Infrared Single Shot Diagnostics for the Longitudinal Profile of the Electron Bunches at FLASH

Dissertation

zur Erlangung des Doktorgrades
des Departments Physik
der Universität Hamburg

vorgelegt von

Hossein Delsim-Hashemi
aus Teheran

Hamburg
2008

Gutachter der Dissertation	Prof. Dr. Jörg Roßbach Prof. Dr. Markus Drescher Dr. A.F.G. van der Meer
Gutachter der Disputation	Prof. Dr. Jörg Roßbach PD. Dr. Bernhard Schmidt
Datum der Disputation	22. Juli 2008
Vorsitzender des Prüfungsausschusses	Prof. Dr. Caren Hagner
Vorsitzender des Promotionsausschusses	Prof. Dr. Joachim Bartels
Dekan der Fakultät für Mathematik, Informatik und Naturwissenschaften	Prof. Dr Arno Frühwald

Abstract

The longitudinal profile of electron bunches plays an important role in the design of single-pass free electron lasers and future linear e^+e^- colliders. For the free electron laser FLASH in Hamburg, a longitudinal compression scheme is used which results in an asymmetric longitudinal bunch profile with a "spike". This "spike", which has a very high peak current, is used in a high-gain SASE-FEL process to produce high intensity (about 70 μJ) femtosecond photon pulses in the XUV wavelength range.
The required high peak current of the electron bunch is realized by confining a large number of electrons in a width, measured in time units, of few tens of femtosecond, making the diagnostics of such bunches a challenge. Furthermore, the operation of facilities such as FLASH shows that single-shot diagnostics is indispensable. It is intuitive to use a time domain method to measure the electron bunch length. However, when the structures present in the bunch profile fall in the femtoseconds range, this is beyond the resolution of time-resolved methods developed so far. In this thesis, a wavelength-domain technique is described that can fulfill both requirements of single shot and high resolution reaching to the femtoseconds range. The amount of charge that is confined in a typical length of several femtoseconds (FWHM of the spike) can be determined by a novel single-shot spectrometer that resolves the coherent radiation (e.g. coherent transition radiation) in the far-infrared and mid-infrared range. Furthermore the extension of this single-shot spectroscopy to shorter wavelengths reaching the near-infrared, makes it possible to investigate the presence of structures in the bunch profile that might correlate or anti-correlate to the SASE intensity.

Zusammenfassung

Das longitudinale Profil von Elektronenpaketen spielt eine wichtige Rolle beim Design von Freie-Elektronen Lasern und zukünftigen e^+e^- Linearbeschleunigern. Das beim Freie-Elektronen Laser FLASH in Hamburg angewandte Kompressionsschema führt zu asymmetrischen longitudinalen Strahlprofilen mit einem "Spike". Dieser "Spike", der einen sehr großen Spitzenstrom besitzt, führt in einem SASE-FEL-Prozess zur Erzeugung von Femtosekunden-Photonenpulsen mit hoher Intensität (ungefähr 70 μJ) im XUV-Wellenlängenbereich.
Den notwendigen hohen Spitzenstrom der Elektronenpakete erhält man, indem eine große Anzahl von Elektronen auf eine sehr kurze Länge kompressiert werden, deren longitudinale Ausdehnung, in Einheiten der Zeit gemessen, nur wenige zehn

Femtosekonden beträgt. Die Diagnose solcher Elektronenpakete ist eine außerordentliche Herausforderung. Desweiteren zeigt der Betrieb von Lichtquellen wie FLASH, dass Diagnostik mit Einzelschussauflösung unverzichtbar ist. Zur Messung der Länge der Elektronenpakete würde man intuitiv eine Methode in der Zeitdomäne wählen. Fallen die im longitudinalen Profil der Elektronenpakete vorliegenden Strukturen jedoch in den fs-Bereich, so stehen bis heute keine zeitaufgelösten Methoden zur Verfügung. In dieser Doktorarbeit wird eine Methode beschrieben, die auf einer Wellenlängenmessung basiert, und die sowohl das Kriterium der Einzelschussauflösung als auch das der hohen zeitlichen Auflösung im fs-Bereich erfüllt. Die Ladungsmenge, die sich in Strukturen mit einer typischen Länge von einigen Femtosekunden (volle Breite bei halber Höhe des "Spike") befindet, kann mit einem neuartiegen Einzelschussspektrometer gemessen werden, welches die kohärente Strahlung (z.B. kohärente Übergangsstrahlung) im fernen und mittleren Infrarotbereich auflöst. Die Erweiterung dieser Einzelschussspektroskopie zu kürzeren Wellenlängen, bis in den nahen Infrarotbereich hinein, ermöglicht Untersuchungen bezüglich des Vorhandenseins von Strukturen, in der Ladungsverteilung welche möglicherweise mit der SASE-Intensität korrelieren oder anti-korrelieren.

Contents

List of Figures

List of Tables

Chapter 1

Introduction

Intense photon-pulses reaching up to several giga-watts of peak power with a pulse-width in the femtosecond range have been sought for by many experiments which are designed to explore the unknown territories in ultrafast physical, chemical and biochemical processes at sub-molecular and atomic resolution. For these experiments the required photon wavelengths range from the VUV down to the Ångstrom regime. Third generation light sources have achieved very high peak brilliances of $\approx 10^{25}\ \frac{\text{photons}}{\text{s mrad}^2\text{mm}^2 0.1\%\text{BW}}$ over a wide range of the electromagnetic spectrum down to the hard X-ray region, but still several orders of magnitude below the desired brilliances. In a typical third generation light source the photon pulse-width is several orders of magnitude longer than the values desired in many experiments. A great leap forward was achieved when free electron lasers based on the Self Amplified Spontaneous Emission (SASE) principle became available. At FLASH, for instance, a single photon-pulse energy of 70 μJ with pulse-width of ≈ 10 fs at a photon wavelength of 13.7 nm has been obtained. A high-gain SASE-FEL such as FLASH, amplifies part of the existing intensity in the white shot noise to several GW of peak power and is not limited to a seed-laser wavelength. The FEL wavelength is tuneable over a wide wavelength range with the undulator field and/or electron beam energy adjustments.

1.1 Free Electron Laser

A Free Electron Laser (FEL) produces coherent electromagnetic radiation like a classical laser, but uses entirely different principles to form the lasing medium. The lasing medium is a relativistic electron beam, which corresponds to the bound atomic or molecular states for conventional lasers. In an FEL, a relativistic elec-

tron beam passes through a periodic transverse magnetic field of an undulator, where it is forced to perform a wiggling path. The acceleration of the electrons along this path results in the release of photons. Mirrors capture the released photons to generate resonant gain through the combined interaction of the electron beam with both, the undulator field and the radiation field stored in the optical resonator formed by the mirrors. At wavelengths where no good mirrors exist, a high gain FEL (see below) can reach a resonant gain and saturate in a single passage along the undulator. The wavelength of the photons can be tuned using the electron beam energy and the magnetic field strength of the undulator, see Eq. 1.3. Compared to conventional lasers, this gives more flexibility to the FELs in the wavelength range coverage and tunability. Operational FEL facilities currently are ranging from microwaves to VUV and they are usually easy to tune.

From single electron radiation to the FEL

The classical radiation power emitted by a particle is quadratically proportional to its charge q and acceleration[1]. Performing Lorenz transformation to the classical radiation power, the emitted power (in the lab system) can be written as [1]

$$P \propto q^2 \gamma^4 \dot{\nu}_\perp^2 \tag{1.1}$$

with $\gamma = \frac{1}{\sqrt{1-\beta^2}}$ where $\beta = \frac{\nu}{c}$. This indicates that one gains a large increase in radiation power when accelerating to ultra-relativistic energies. The key feature in terms of FELs is the quadratic dependence on charge. Re-writing Eq. 1.1 in terms of N, the number of electrons in an electron bunch, the quadratic dependence on N shows up

$$P \propto N^2 e^2 \gamma^4 \dot{\nu}_\perp^2 \tag{1.2}$$

The radiation per electron is proportional to $Ne^2\gamma^4\dot{\nu}_\perp^2$ which is N times larger than single electron power intensity in Eq. 1.1. In practice a large number of electrons are involved. The main condition for Eq. 1.2 to hold is that all electrons have to make a point-like charge distribution compared to the wavelength of the light given by Eq. 1.3. This imposes some very tight requirements on the electron beam quality with respect to transverse and longitudinal distributions, which are impossible to meet in practice if sub-micrometer wavelengths are desired.

[1] The contribution from the longitudinal acceleration is negligible.

Microbunching

The typical length of the highly compressed electron bunches is in the range of few micrometers which is still much longer than the light wavelength in the VUV and X-ray range. Thus, coherent emission in the spirit of Eq. 1.2 cannot take place. The FEL mechanism, however, provides an efficient way to generate a longitudinal density modulation in the electron bunch on the scale of the optical wavelength resulting in a periodic sequence of bunchlets being shorter than the optical wavelength. This phenomena which is called "microbunching" gives the essential advantage to the FEL radiation because a large number of electrons radiate coherently [3].

FEL wavelength

The equation of motion for electrons in the presence of the undulator magnetic field is considered in literatures e.g. [2, 3]. The energy transfer from the electron beam to the co-propagating light wave exhibits resonance behavior as a function of the light wavelength. In terms of the undulator parameter $\mathtt{K} = \frac{\mathtt{e}\lambda_\mathtt{u}\mathtt{B}}{2\pi\mathtt{m}_0\mathtt{c}}$ (where $\mathtt{B}$ is the peak magnetic field), undulator magnetic period $\lambda_\mathtt{u}$, and normalized electron energy γ, the strongest resonance happens at a wavelength given by [3]

$$\lambda_\ell = \frac{\lambda_u}{2\gamma^2}(1 + \frac{K^2}{2}) \tag{1.3}$$

SASE principle and gain length

The amplification of radiation in an FEL can be considered in two general cases. If the changes in the electromagnetic field due to FEL gain in each passage are small it can be described by a low-gain FEL model (see e.g. chapter 1 in [2]). In order to make this low gain useful, an optical resonator must be used where the radiation is amplified over many cycles of interaction with a large number of subsequent bunches. In the extreme ultraviolet and X-ray regimes, however, there are no suitable mirrors to build an optical resonator.
The high gain FEL model describes the situation that the changes of the electromagnetic field are strong in a single passage through the undulator (see e.g. chapter 2 in [2]). The radiation intensity grows exponentially with a characteristic e-folding length $\mathtt{L_G}$. To start the process, there are two general options. One may "seed" the FEL using photons generated by an external laser of the same wavelength as the FEL wavelength (Eq. 1.3), or could start from the spontaneous undulator radiation generated in the first section of the undulator which

is amplified by the FEL mechanism in the subsequent undulator sections. The latter is referred to as Self Amplified Spontaneous Emission (SASE) of high-gain FELs [4].
The gain length, $\mathtt{L_G}$, is given by

$$L_G = \frac{1}{\sqrt{3}}\left(\frac{2mc\gamma^3\sigma_r^2\lambda_u}{\mu_0 e\hat{I}K^2}\right)^{1/3} \tag{1.4}$$

where $\pi\sigma_{\mathtt{r}}^2$ is the beam cross section and $\hat{I}$ is the peak current. The more complete picture is given in the 3D-FEL model where, for instance, the effect of transverse emittance of electrons and diffraction effects of the radiation can be explained [2]. With given undulator parameters, in order to have short gain length, the emittance of the electron beam should be small and its peak current larger than ≈ 1 kA. The latter requires to compress the electron beam longitudinally without defecting the emittance.

1.2 FLASH Linac

The Free Electron LASer in Hamburg (FLASH), the successor of TTF1[2], at DESY is a FEL based on SASE principle and can deliver very intense light in the wavelength range 32 nm [7] to 13 nm [8] in the first harmonic[3]. Installation of further accelerating modules has been done to achieve higher electron energies and thereby achieve even shorter wavelengths as 6.5 nm in the first harmonic. The peak brilliance of FLASH and some other future FELs are shown in Fig. 1.1. The peak brilliance of third generation synchrotron radiation sources are orders of magnitude lower than FELs over a wide range of photon energies.

The layout of the FLASH linac is shown in Fig. 1.2. The FLASH injector consists of a photo-cathode RF-gun which emits electrons when the gun laser hits the cathode. Acceleration happens in 5 cryo-modules (after the recent upgrade 6 cryo-modules), each with eight 1m-long superconducting 9-cell cavities. This acceleration provides energies between 450 to 700 MeV (currently up to 1 GeV). Two magnetic chicanes accomplish the main longitudinal compression of the electron bunches. Six undulators compose the FEL for FLASH, each 4.5 m long and

[2]The vacuum ultra-violet (VUV) free-electron laser at the TESLA Test Facility (TTF) Phase 1 demonstrated saturation in the wavelength range 80-120 nm based on the self-amplified spontaneous emission (SASE) principle [5, 6]

[3]Experiments that are described in this thesis were carried out when the maximum electron energy was 700 MeV (that corresponds to 13 nm SASE-FEL wavelength). The installation of new modules to achieve energies up to 1 GeV has been done later.

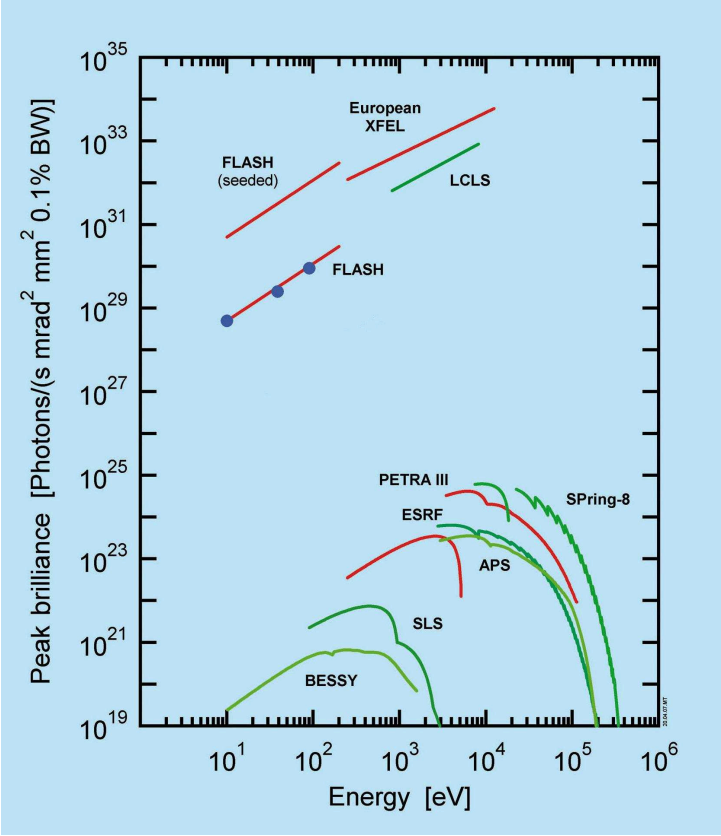

Figure 1.1: The peak brilliance of today's light sources (adapted from [9])

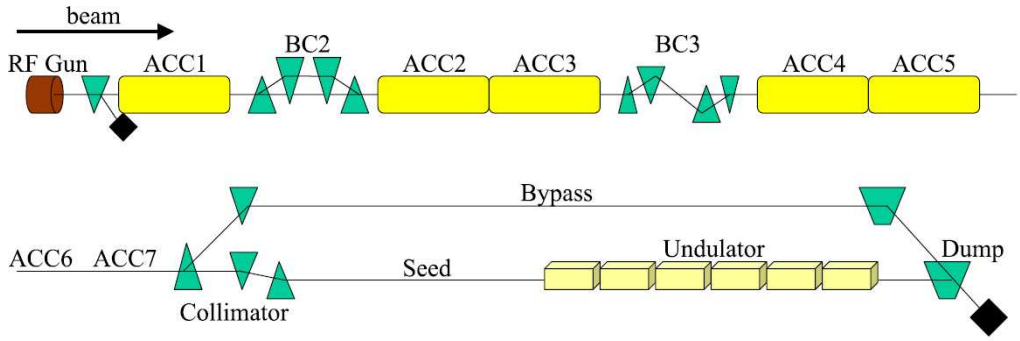

Figure 1.2: FLASH layout (before installation of accelerating module ACC6)

with a magnetic period of 2.73 cm. The bypass has been foreseen to protect undulators from high beam losses during accelerator studies.
The time structure of the electron bunches at FLASH is as follows. There are two modes, short pulses mode: maximum 30 bunches in each train (macro-pulse) and long pulse mode: up to 800 bunches in each train. In the short pulse mode the spacing between successive bunches in a train can be any of 1, 2, 4, 5, 10, 20 and 25 μs. The repetition rates of the macro-pulses that FLASH is already operated are 2 and 5 Hz.

Bunch Compression Scheme

One of the challenging requirements on the electron bunches at FLASH is to achieve peak currents as high as 2500 A. Increasing the charge density in RF gun region is limited due to space charge effects. In contrast, when electrons are ultra-relativistic, it is possible to compress them longitudinally. Here the velocity bunching is not possible because electrons have very small velocity differences. One way to compress the electron bunches is to introduce an energy chirp and then pass a dispersive section (Fig. 1.3). Upstream of a magnetic chicane[4], dependent on the off-crest phase of an accelerating module, an energy chirp ($\frac{\Delta E}{E}$) can be introduced that leads to longitudinal compression when the electron bunch passes through the chicane. The path length of electrons in a magnetic chicane is dependent on their energy, higher energy electrons make a shorter path. In this scheme the tail of the bunch should have higher energy than its head. When the bunch passes through the compressor, tail electrons can catch up with head electrons and the electron bunch gets longitudinally compressed. In references [10, 11] the magnetic chicane bunch compressors are discussed in detail. In terms of η_s, the

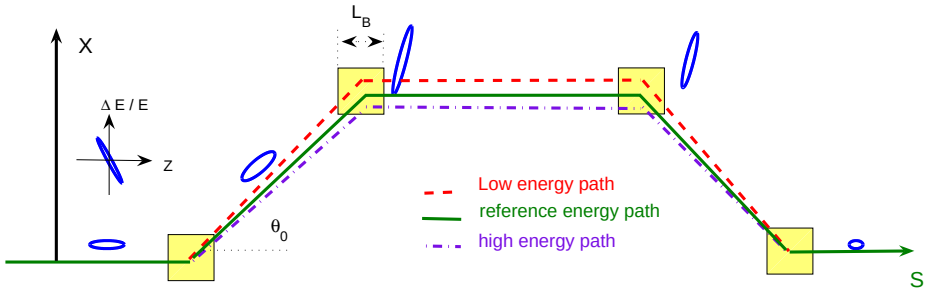

Figure 1.3: A four dipole based bunch compressor chicane.

[4]A dispersive section composed of dipoles only (without any quadrupole).

longitudinal dispersion, the path length difference for a relative energy deviation δ can be written as [11]

$$\Delta z = \eta_s(\delta).\delta = R_{56}.\delta + T_{566}\delta^2 + U_{5666}.\delta^3 + ...$$

$\mathtt{R_{56}}$ is called the linear longitudinal dispersion. For a 4-dipole chicane like Fig. 1.3, in terms of the geometry of the chicane, $\mathtt{R_{56}}$ is given by [11]

$$R_{56} = -2\theta_0^2(\frac{L_{act}}{2} - \frac{4}{3}L_B)$$

where θ_0 is the chicane's bend angle, $\mathtt{L_{act}}$ is the active chicane length and $\mathtt{L_B}$ is the dipoles length.
The change in the energy of a particle at $\mathtt{z_0}$ (longitudinal coordinate with respect to a reference particle) after acceleration in an RF section is given by

$$E(z_0) = eV\cos(\phi + kz_0)$$

where ϕ is the off-crest phase of the bunch to the RF wave and k is the RF wavenumber ($\mathtt{k} = \frac{2\pi}{\lambda_{RF}}$). The linear term in the accelerating field is defined as energy 'chirp' factor h [11]

$$h = -\frac{eV}{E}\sin\phi$$

In terms of h, the correlated energy spread along the bunch is $\frac{\Delta E(z_0)}{E} = \delta = \mathtt{hz_0}$. It can be seen that with linear approximation for correlated energy change and a bunch with length $\sigma_\mathtt{i}$ before the bunch compressor, the bunch length after passing a 4-dipole chicane can be written as [11]

$$\sigma_f = \sqrt{(1 + hR_{56})^2\sigma_i^2 + R_{56}^2\sigma_{\delta_i}^2} \tag{1.5}$$

where $\sigma_{\delta_\mathtt{i}}$ is the uncorrelated energy spread. The maximum compression happens where $\mathtt{1 + hR_{56} = 0}$, in this case the bunch length is given by $\sigma_\mathtt{f} = |\mathtt{R_{56}}|\,\sigma_{\delta_\mathtt{i}}$. In Eq. 1.5 with high quality beam of RF-photocathode gun, the uncorrelated energy spread can be neglected and

$$\sigma_f = |1 + hR_{56}|\,\sigma_i = \frac{\sigma_i}{\mathcal{C}}$$

In addition to the bunch length compression, the uncorrelated energy spread is magnified by the compression factor $\mathcal{C}$ thus preserving the longitudinal emittance [11].

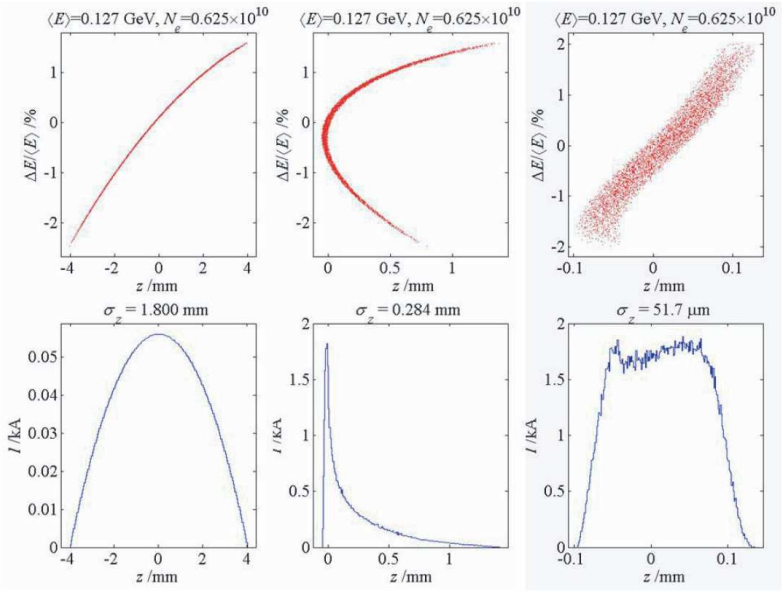

Figure 1.4: Longitudinal phase space and bunch current distribution before (left two plots) and after (center two plots) a bunch compressor chicane. The right two plots show the phase space after the chicane if a $3^{rd}-$`harmonic` RF section is used to compensate the non-linearities of the fundamental frequency and magnetic chicane. The R_{56} is increased here to achieve the same 1.8 kA peak current (adapted from [11]).

The nonlinear RF accelerating field results in strong non-linearities in the chirp and this together with T_{566} of the chicane dominates the shape of the bunch and develops a spiky shape (Fig. 1.4). In a 4-dipole chicane bunch compressor scheme, a way to compensate for this nonlinearities is to linearize the accelerating RF field by means of a 3^{rd} harmonic RF. In this case the shape of the chirp and resulting bunch shape after magnetic chicane is shown in the right side of Fig. 1.4. The effect of the second bunch compressor of FLASH, the S-shape bunch compressor, can be considered in a similar way and can be found in the references e.g. [10, 11].

Chapter 2

Longitudinal Beam Diagnostics

The role of the longitudinal compression of the electron bunches to achieve the required high peak currents is outlined in section 1.1. As the electron bunches get longitudinally compressed the measurement of their profile becomes more important and difficult. There are theories that try to describe the longitudinal compression of the bunches and experimental data are required to investigate these models. The present investigations might help to improve the current understanding and ultimately get closer to the design of the desired compressors.
The expected longitudinal profile of the electron bunches at FLASH has structures as short as a few femtoseconds, this requires a high resolution bunch profile diagnostics. The tail of the bunch may extend to a few picoseconds. When a full bunch profile measurement is required this long tail determines the range that has to be covered by the diagnostics tool[1]. The changes of the bunch profile from shot to shot have to be monitored. Therefore, single shot capability for the diagnostics tool is required. In other words, the ideal longitudinal diagnostics tool should be single shot, broad-band, and with high resolution. Additional requirements would be: easy to operate and maintain, non-invasive, compact and easy to incorporate in different parts of the machine, operating independent of machine parameter changes. Several longitudinal diagnostics experiments are implemented in the diagnostic section between the second bunch compressor (BC3) and the FEL undulator (Fig. 1.2). The transverse deflecting RF structure (TDS) measures the longitudinal bunch profile with a resolution down to 15 fs (rms) by applying a time dependent vertical streak to the electron bunch and measuring the vertical bunch profile afterwards. The longitudinal charge profile of the bunches can be probed by detecting their Coulomb field by means of electro-optic crystals close

[1]For instance with a Fourier transform spectrometer, the low frequency limit that has to be measured corresponds to this tail.

to the beam trajectory. The optical properties (namely the birefringence) of the crystals are changed proportional to the electric field strength and the cumulative effect on a co-propagating short laser pulse can be detected. In this way, the temporal (longitudinal) structure of the bunch charge is impressed in a polarization modulation of the optical pulse [13]. Detection of coherent undulator radiation produced by an electron beam already modulated by an optical laser is the basis of a method which is called optical replica. Single shot spectra of coherent radiation can be measured to reconstruct the longitudinal electron bunch profile.

2.1 The transversely deflecting RF structure

One way to measure the bunch length is to streak the bunch using a transverse RF deflecting structure (TDS). Such a device, which was constructed and tested at SLAC in the 1960's [12], has been installed at FLASH [14] in collaboration with SLAC. The S-band (2.856 GHz) TDS cavities are similar to the disk loaded S-band

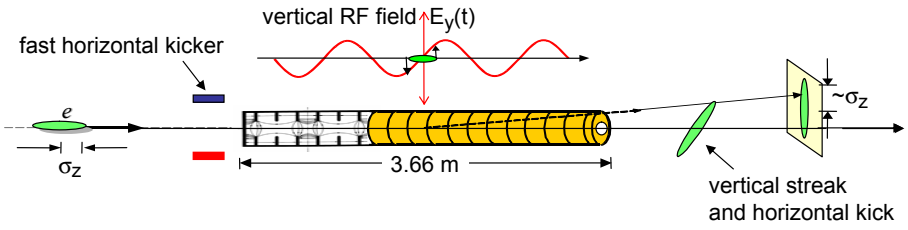

Figure 2.1: Scheme of the operating principle of the transversely deflecting structure. Adapted from [15].

accelerating structures of SLAC except for the irises that have mode-locking holes that result in excitation of the $\mathtt{TM}_{11}$ hybrid mode [16]. When electron bunches enter the TDS which is already filled with this mode, they exhibit a transverse streak in the vertical direction. The streaked bunch is kicked out of the train (by means of a fast kicker) and hits an off-axis screen, Fig. 2.1. Then the produced optical transition radiation can be measured with an optical system to be used to reconstruct the initial bunch profile. The time resolution that can be achieved with the TDS is related to the value of the beta-function of the electron beam on the screen. Optimizing the electron beam optics, the time resolution of a TDS can reach 15 fs (rms) [17]. For the beam optics used during standard accelerator operation the beam size is bigger and therefore the resolution is limited to about 55 ± 5 fs (rms) [14].

2.2 Electro-optical sampling

The electro-optical (EO) detection of THz radiation is based on the Pockels effect in which an applied voltage causes the detector crystal to become birefringent. When the optical sampling pulse travels through the crystal at the same time as one temporal point of the THz pulse, its polarization is slightly rotated. The magnitude of rotation is proportional to the magnitude of the THz field, and the direction of rotation is dependent on the sign of the field. In this way, the

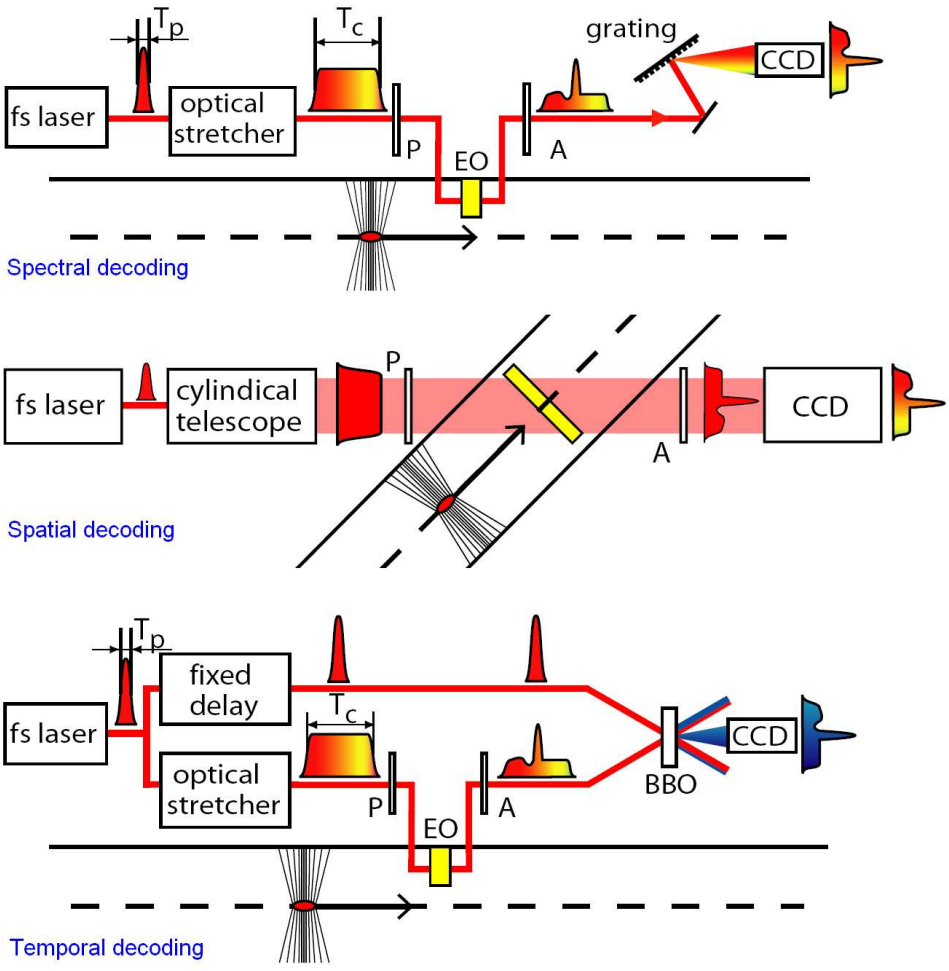

Figure 2.2: Overview on different methods to decode the temporal information from the laser pulse probing the EO crystal. Adapted from [18].

temporal (longitudinal) structure of the bunch charge is impressed in a polarization modulation of the optical pulse. An appropriate optical layout can be used to convert this polarization modulation to the field modulation. For single shot measurement there are different techniques to use the aforementioned effect.

Introducing a known chirp to the optical laser pulse and measuring the optical spectrum of the laser after passing the EO crystal is the basis of spectral decoding. If a stretched optical laser pulse incide with an oblique angle on the crystal, different spatial positions on the crystal will be reached by the laser in different times that could correspond to the instantaneous polarization change made by THz pulse field. This is called spatial decoding. The non-stretched probe laser

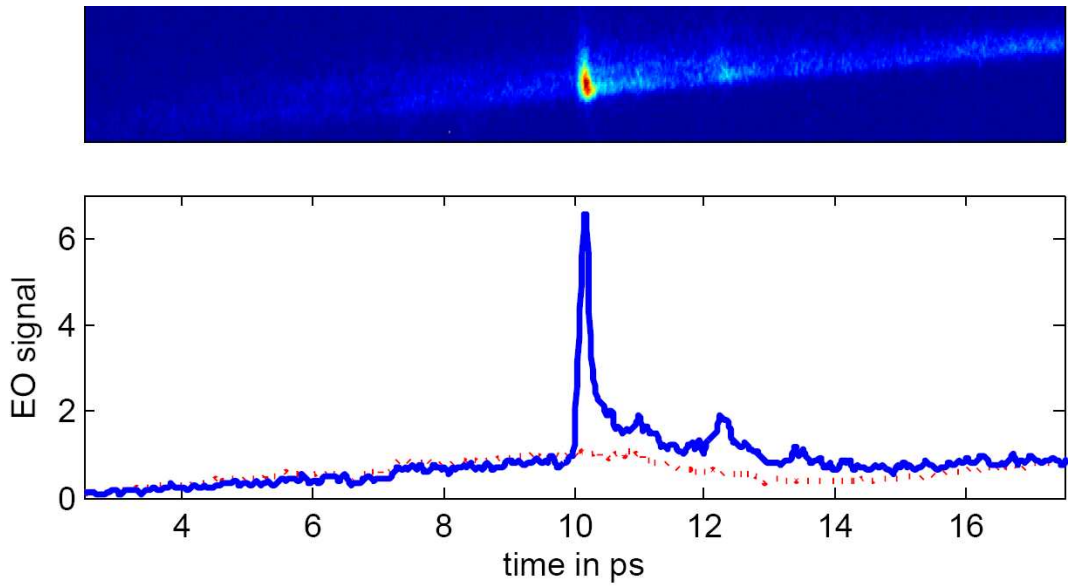

Figure 2.3: Longitudinal bunch profile measured at FLASH with the electro-optic temporal decoding technique using a 100 μm thick GaP crystal. Adapted from [18].

can be split in two parts, one to go through the same process as spectral decoding and the other to be used to make a time-space mapping [18]. An overview on the different single shot electro-optical methods is shown in Fig. 2.2. Single-shot EO bunch length measurements were pioneered at FELIX [20] with the spectral decoding, the more recently developed spatial decoding [21] and temporal decoding [22] techniques offer higher resolution at the price of enhanced complexity. An overview on the electro-optical techniques for bunch length diagnostics is given in [13, 19]. In Fig. 2.3 a measurement performed at FLASH is shown. It shows a FWHM of about 100 fs for the spike in the time domain profile [18, 23].

2.3 Optical replica

The method proposed recently by Saldin et al. [24] is based on detection of coherent undulator radiation produced by modulated electron beam. A seed optical laser is used to produce an optical replica of the field of the electron bunches. The electron bunch and the laser pulse overlap by adjusting the timing of the laser pulse[2] in a modulator that consists of an undulator (tuned for the resonance at the laser wavelength) and a dispersion section (a chicane with $R_{56} = 50\ \mu m$). In this step, the density modulated (same as the laser wavelength) electron bunch enters to another undulator (radiator) which is also tuned to the laser wavelength. This results in the coherent radiation in the laser wavelength. Then an ultrashort optical-pulse measurement device can be used to provide real-time single-shot measurements of the electron bunch structure [24].

2.4 Coherent radiation diagnostics

The most common coherent radiation sources for diagnostics purposes are transition radiation (TR), diffraction radiation (DR), synchrotron radiation (SR), Smith-Purcell radiation (SPR) and edge radiation (ER) (see chapter 3). For wavelengths of the radiation longer than or comparable to the distance of electrons, these electrons radiate "in phase" or coherently, the intensity of this coherent radiation scales with the square of the number of contributing electrons. The intensity integrated over the coherent radiation spectrum can be used as a relatively simple tool to control the compression of the electron bunches. From spectrally resolved measurements of the intensity of the emitted coherent radiation, information about the longitudinal form factor and thus the charge distribution can be obtained. This can be done either using a Fourier transform interferometer or using grating spectrometers. Although only the magnitude of the form factor can be measured, the bunch profile can be reconstructed within certain limitations using parametrized bunch profiles that can be fit to the measured spectra. Alternatively, the Kramers-Kroning relation can be used to estimate the phase (e.g. see [25]). These are described in more details in section 9.2.

[2]The seed laser pulse has to be longer than the time jitter of the electron bunch

Bunch compression monitors

The polychromatic coherent radiation of the electron bunches can be focused on a single pyroelectric detector (see chapter 5) to get a signal proportional to the total radiated intensity. This provides a simple tool to control the compression of the bunches, called Bunch Compression Monitor (BCM). The integrated signal described above is dominated by relatively long wavelength contributions and accordingly is not very sensitive to the short wavelengths content in the spectrum of the coherent radiation. The compressed bunches at FLASH have a spike which contains roughly 10% of the electrons. The rest of the electrons which are in the tail contribute to intensities in the long wavelengths of the coherent radiation spectrum when bunch is subjected to radiate. The spectrally resolved coherent radiation contains more information on the compression process than the integrated radiation. A device which is called Advanced Bunch Compression Monitor (ABCM) [26] can be used to detect any part of the coherent radiation spectrum. The basic principles of this device are described in section 6.2.2. The detected regions might cover the wavelengths corresponding to the width of the spike in the time domain bunch profile (see Fig. 8.16).

Bunch length diagnostics using Fourier transform spectrometers

In many areas of science and dependent on the application, different spectrometers have been developed to measure the spectra that can be any part of the electromagnetic spectrum. Steady phenomena can be resolved with Fourier transform spectrometers, e.g. the Martin-Puplett interferometer. These are devices that typically probe the spectrum with a shifted in time version of itself. An autocorrelation function can be measured and, knowing enough on the spectral behavior of the entire instrument (e.g. grids, mirrors, lenses, polarizer and detectors), one could extract the spectrum with high resolution. A recent work conducted at FLASH using a Martin-Puplett interferometer is reported in reference [27]. The bunch profile is reconstructed from the measured coherent synchrotron radiation from the last magnets of the first bunch compressor (BC2 in Fig. 1.2). When the subject under study deals with phenomena that vary from shot to shot, non single-shot spectroscopy is not very useful. Most of the operational interferometers as bunch length diagnostics tool, e.g. the Martin-Puplett interferometer, have a movable element (a linearly moving arm or a rotating grating) and the signals in each step of the moving element are recorded to form the interferogram. Therefore, they are intrinsically not single-shot devices.

Bunch length diagnostics using grating spectrometer

For the single-shot detection of a broad-band spectrum, like coherent transition radiation of the electron bunches in a linac-driven FEL, it is straightforward to think of dispersive elements that are capable of sorting the radiation in terms of wavelengths. Well known single element optical devices that can do this are prisms and diffraction gratings. The spatial distribution of the dispersed light is wavelength dependent. That makes it possible to record the spectra for individual shots provided a suitable detection system is in place. Prisms can be used for visible to mid-infrared light. The dispersive power of a typical prism is not strong and single-shot high resolution spectra cannot be recorded even over their limited range of coverage. Diffraction gratings are available for almost the entire electromagnetic spectrum. Depending on the application, an appropriate choice can be made. The description of gratings problem as dispersive elements of spectrometers is given in chapter 4. The basic principles of different types of grating spectrometers are described in chapter 6.

Chapter 3

Coherent Radiation Sources for the Electron Bunch Diagnostics

One method for the longitudinal diagnostics of electron bunches is the measurement of the emitted spectrum when electrons are subjected to a radiation process. The most common radiation sources are Transition Radiation[1] (TR), Synchrotron Radiation (SR), Smith-Purcell Radiation (SPR) and Edge Radiation (ER). In order to compute the coherent radiation spectrum, one should get the single electron spectrum from the theory. Then for any given electron distribution along the bunch, it is straight forward to derive the spectral energy density of the entire bunch, the quantity that can be measured. The generalized case of a three dimensional charge distribution of the electron bunches can often be simplified (see Fig. F.4) by considering it as a line charge distribution along the longitudinal coordinate denoted by $\rho(t)$. Here the transverse size effect is neglected. This assumption may result in over estimation of short wavelengths content.
The normalized line charge distribution[2], $\widetilde{\rho}(t)$, can be converted to the frequency domain to derive the "longitudinal form factor" of the bunch as

$$F_{long}(\omega) = \int_{-\infty}^{\infty} \widetilde{\rho}(t) \exp(-i\omega t) dt \tag{3.1}$$

In terms of this form factor, the spectral radiation density for the entire bunch can be written as

$$\frac{d^2U_N}{d\omega d\Omega} = \left(N + N(N-1)\left|F_{long}(\omega)\right|^2\right) \frac{d^2U_1}{d\omega d\Omega} \tag{3.2}$$

[1] Including its special case of Diffraction Radiation (DR)
[2] Normalized to the total bunch charge

where $\frac{d^2U_1}{d\omega d\Omega}$ is the radiation intensity emitted by a single electron into the solid angle $d\Omega$ in the frequency band $d\omega$ of the specific radiation process . In general the single electron spectrum depends on the electron energy, ω (the angular frequency), the point of observation and details on the physics of the generation of the radiation. For a large enough number[3] of electrons Eq. 3.2 can be simplified to

$$\frac{d^2U_N}{d\omega d\Omega} = N^2 \left|F_{long}(\omega)\right|^2 \frac{d^2U_1}{d\omega d\Omega} \tag{3.3}$$

The interpretation is simple, the term $N^2 \left|F_{long}(\omega)\right|^2$ is a measure of how well, for a given frequency ω, the entire charge acts as a single macro-charge.

3.1 Transition radiation

The following section outlines, mainly based on reference [28], how to calculate the single electron spectrum for transition radiation. The problem of synchrotron radiation is also addressed in the next section. When a charged particle traverses the boundary of two media of different dielectric properties its self field gets modified and this results in a radiation which is called transition radiation. One example of such a radiation process is when a thin screen of a conductor is in the passage of relativistic electrons. In the ideal case of infinite transverse size of the screen the radiation intensity is frequency independent. In contrast, for real screens of finite size the radiation intensity is frequency dependent.

3.1.1 Ginzburg-Frank formula

For the special case that an electron crosses the boundary from vacuum to an infinite metallic plane the spectral and spatial radiation energy of backward transition radiation is given by the Ginzburg- Frank formula [29, 30]:

$$\frac{d^2U_{GF}}{d\omega d\Omega} = \frac{e^2}{4\pi^3\epsilon_0 c} \frac{\beta^2 \sin^2\theta}{(1-\beta^2\cos^2\theta)^2} \tag{3.4}$$

with $\beta = v/c$ and θ the angle against the backward direction (see Fig. 3.1). This is valid in the far field and is independent of frequency, provided one stays well below the plasma frequency[4] of the metal.

[3] This approximation is valid when $N\left|F_{long}(\omega)\right|^2 >> 1$.

[4] The plasma frequency is given by $\omega = \sqrt{\frac{ne^2}{m\epsilon_0}}$, where n is the density of electrons in the material of the screen, e is the electronic charge, m is the mass of the electron, and ϵ_0 is the permitivity of free space. As a typical value, the plasma frequency of copper is ≈ 16 PHz.

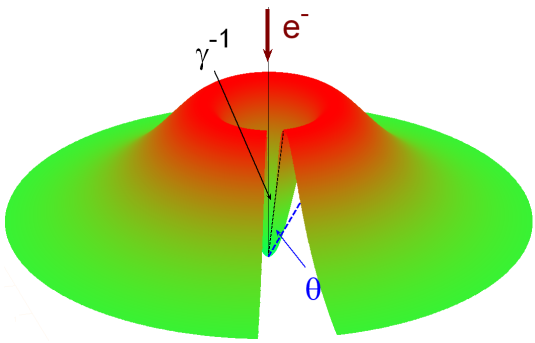

Figure 3.1: Ginzburg-Frank spatial distribution for the transition radiation by a single electron. The angle against backward direction is shown by θ. At $\theta = 1/\gamma$ the maximum intensity appears.

3.1.2 Generalized Ginzburg-Frank formula

For a finite circular screen of radius a one can see that the spectral and spatial radiation energy in far field is given by [28]:

$$\frac{d^2U_{generalized-GF}}{d\omega d\Omega} = \frac{d^2U_{GF}}{d\omega d\Omega}[1 - T_a(\theta,\omega)]^2 \tag{3.5}$$

where

$$T_a(\theta,\omega) = \frac{\omega a}{c\beta\gamma}J_0(\frac{\omega a \sin\theta}{c})K_1(\frac{\omega a}{c\beta\gamma}) + \frac{\omega a}{c\beta^2\gamma^2\sin\theta}J_1(\frac{\omega a \sin\theta}{c})K_0(\frac{\omega a}{c\beta\gamma}) \tag{3.6}$$

This form reduces to the Ginzburg-Frank formula when $a \geq \gamma\lambda$ and $\mathtt{D} \geq \gamma^2\lambda$ ($\mathtt{D}$ is the distance from the source to the observation point).
In near field ($\mathtt{D} \leq \gamma^2\lambda$), for the angular dependence of the intensity only an integral form can be derived [28]:

$$\frac{d^2U_{generalized-GF}}{d\omega d\Omega} \propto \left|\int_0^a J_1(k\rho\sin\theta)K_1(\frac{k\rho}{\beta\gamma})\exp(ik\frac{\rho^2}{2R})\rho d\rho\right|^2 \tag{3.7}$$

In order to orient this back reflected radiation to an experimental setup the target screen normally has an angle of $45°$ to the electron beam which introduces an asymmetry to the spatial distribution that can be derived by the inclination factor $\chi = \cos\theta$ (see chapter 3.7 in [28]). It is clear from Eq. 3.5 that for a finite screen, the radiation energy acquires an ω dependence. The spectral energy density given by Eq. 3.5 can be evaluated with numerical integration. In Fig. 3.2 the TR energy per frequency interval $\Delta\mathtt{f} = 1\ \mathtt{GHz}$ that is emitted by an electron with $\gamma = 1000$ is plotted as a function of the TR screen radius a. The wavelength is varied between 50 $\mu\mathtt{m}$ to 2 mm. All curves show a rise with increasing TR screen radius. For large enough screen size they all approach asymptotically to $\frac{\mathtt{e}^2}{2\pi^2\epsilon_0\mathtt{c}}(\ln\gamma + \ln 2 - 0.5)$ (see chapter 3.5 in [28]).

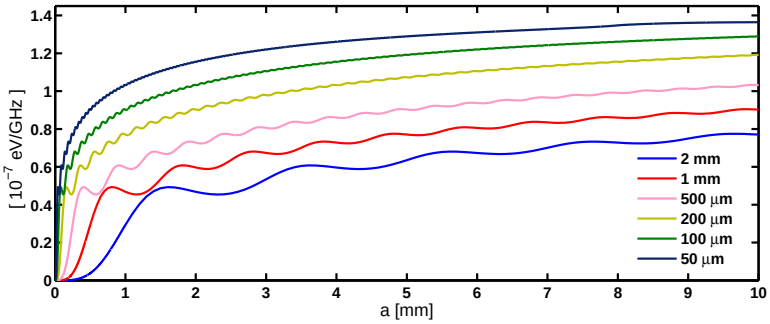

Figure 3.2: Transition radiation by single electrons. The TR energy in eV per GHz bandwidth is shown as a function of screen radius a for wavelengths from 50 μm to 2 mm. Lorentz factor $\gamma = 1000$ (see Fig. 9 in [28]).

3.1.3 Coherent transition radiation by an electron bunch

So far assuming the line charge along the electron bunch, the transverse distribution was neglected. For a cylindrically homogeneous transverse distribution with radius r_b, the spectral energy density of the entire bunch is given by Eq. 3.3 with [28]

$$\frac{d^2U_1}{d\omega d\Omega} = [\frac{2c}{\omega r_b \sin\theta} J_1(\frac{\omega r_b \sin\theta}{c}) - \frac{2c\beta\gamma}{\omega r_b} I_1(\frac{\omega r_b}{c\beta\gamma}) T_a(\theta,\omega)]^2 \frac{d^2U_{GF}}{d\omega d\Omega}$$

where $T_a(\theta,\omega)$ is given by Eq. 3.6. More general bunch profiles can be studied numerically.

3.1.4 Diffraction Radiation

For a diffraction radiation screen of radius a which has a hole of radius b, the single electron spectral energy is given by [28]

$$\frac{d^2U}{d\omega d\Omega} = [T_a(\theta,\omega) - T_b(\theta,\omega)]^2 \frac{d^2U_{GF}}{d\omega d\Omega}$$

In Fig. 3.3 a comparison for the far-field angular distribution of TR, produced at a disk with radius $a = 20$ mm, with that of Diffraction Radiation (DR) at the same size disk but with a central hole of radius $b = 2$ mm is shown. The distributions are all normalized to the maximum value of the transition radiation at the longest wavelength of 50 μm. Diffraction radiation intensity reduces dramatically with decreasing wavelength. This loss is much more pronounced at smaller energies ($\gamma = 500$ is shown in Fig. 3.3 in the left). In Fig. 3.4 a comparison for the spectra

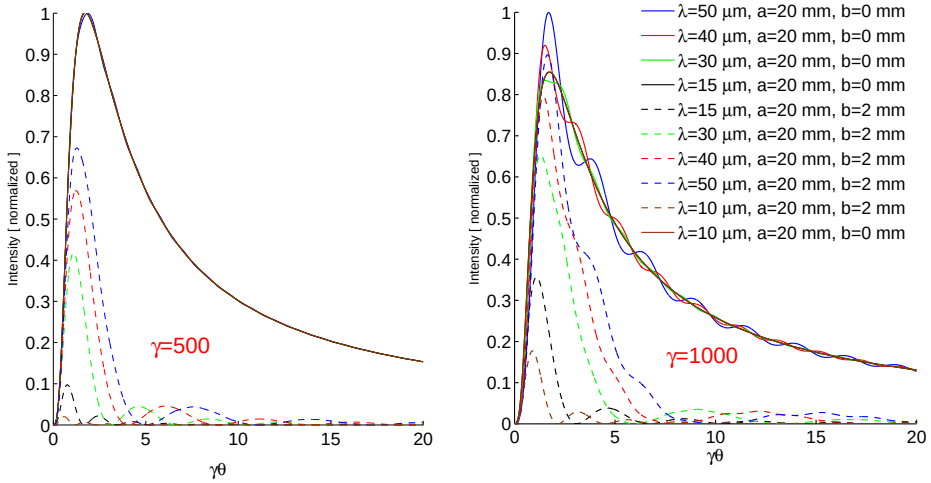

Figure 3.3: Angular distribution of transition and diffraction radiation from a circular disk (radius $\mathtt{a} = 20\ \mathtt{mm}$) target. Solid curves are TR on a disk without hole, the other curves refer to DR on a disk of radius $\mathtt{a} = 20\ \mathtt{mm}$ which has a central hole of radius $\mathtt{b} = 2\ \mathtt{mm}$ (see Fig. 11 in reference [28]).

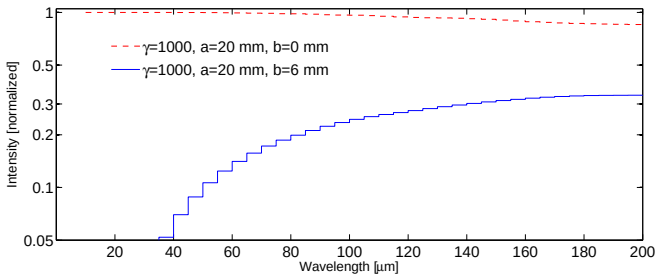

Figure 3.4: Single electron spectra as a function of the wavelength for two targets, a full circular disk of radius $\mathtt{a} = 20\ \mathtt{mm}$ in red (dashed), and a same disk with a hole of radius $\mathtt{b} = 6\ \mathtt{mm}$ in blue (solid). There is a cut-off at about $40\ \mu\mathtt{m}$ for diffraction radiation.

of a single electron subjected to TR and DR are shown. A short wavelength cut-off close to 40 μm is exhibited for DR. This cut-off depends on the size of the slit in the target screen. An experimental evidence for this short wavelength cut-off is shown in Fig. 8.12.

3.2 Synchrotron radiation

Dipole magnetic field deflects a relativistic electron and centripetal acceleration produces radiation which is known as synchrotron radiation. The fully non-invasive nature of this source makes it very attractive for the purpose of diagnostics. Synchrotron radiation is broad-band and the shorter wavelengths are more confined to narrower emission angles.
The electric field of an electron moving along an arbitrary trajectory is given by the Lienard-Wiechert formula [1]

$$E(t) = \frac{e}{\gamma^2 \left|\vec{r}\right|^2} \left[\frac{\hat{n} - \vec{\beta}}{(1 - \hat{n} \cdot \vec{\beta})^3}\right]_{ret} + \frac{e}{c \left|\vec{r}\right|} \left[\frac{\hat{n} \times [(\hat{n} - \vec{\beta}) \times \dot{\vec{\beta}}]}{(1 - \hat{n} \cdot \vec{\beta})^3}\right]_{ret} \tag{3.8}$$

where $\hat{\mathrm{n}}$ is a unit vector along the direction from the emission point to the observation point. The quantity in the brackets has to be evaluated in the retarded time $t' = t - \frac{1}{c}\left|\vec{r}(t')\right|$. Using this formula one can get the spatial spectral density of a single electron moving along a circle known as Schwinger formula. When the electron trajectory is not a complete circle, e.g. when electron travels along a short dipole magnetic field, one has to perform numerical calculation starting from field given by Eq. 3.8 [31].
In reference [31], synchrotron radiation from a short magnet is discussed in details. For a very small bending angle comparable with $\frac{1}{\gamma}$ the spatial and spectral radiation density from an electron could be given by an analytic form (see section 3.2.2 in [31]).
In general, for a full reconstruction of the bunch profile, when the absolute intensities are important, SR sources seem to be more complicated than TR. In applications like bunch compression monitoring where the relative intensity changes are important, if enough care is taken, SR can be used instead of TR. Measured spectra of SR should be unfolded for contribution that may come from different dipoles of a chicane or wiggler as well as the complication that may arise because of waveguide effect of vacuum chamber that may bring the radiation from upstream magnets to the measurement port.

Chapter 4

Electromagnetic Theory of Diffraction Gratings

The coherent radiation of electron bunches is broad-band ranging from a few micrometers to millimeter wavelengths. For single shot spectroscopy of the emitted coherent radiation, gratings can be used to disperse the polychromatic radiation into its components. The widest free spectral range of a grating is when it is used in its lowest non-zero diffractive orders (± 1 `order`). The free spectral range is then close to a factor of two for an optimized setup. Therefore a single grating unit cannot cover the entire range of interest. A proper design of the grooves geometry and the grating setup can make it possible to stage the process of dispersing the radiation. In each stage, for a wide range of the shortest present wavelengths, the grating acts as a very efficient dispersive element and at the same time it filters the longer wavelengths from any short wavelengths content [32]. These longer wavelengths can then be resolved in a later stage with an appropriate grating pitch size. In each stage the dispersed radiation is well separated from the longer non-dispersed wavelengths. With this short introductory remarks it becomes clear that a deeper understanding of the grating physical problem has to be established.

For several decades physicists were trying to solve the problem of diffraction grating energy distribution within a given order. Earlier approaches ended with approximate solutions applicable only to low $\lambda/\mathtt{g}$, where λ is the wavelength and g the groove spacing. Later, Pavageau and Bousquet [33] found an integral formalism with only restriction of a perfectly conducting surface. The next breakthrough was made by Maystre who derived an efficient single integral equation formalism that could handle real metals with no geometric restrictions for both S (TM mode, electric field perpendicular to the grooves) and P (TE mode, electric

field parallel to the grooves) polarizations [34].
Maystre has discussed the rigorous computational treatment of the diffractive efficiency of a plane grating. In general, there are two limiting regimes defined by the ratio of the wavelength to the grating groove spacing $\lambda/\mathtt{g}$. The vector regime is encountered when $\lambda/\mathtt{g} > 0.2$ and the solution of Maxwell's equation for diffractive efficiency depends upon the polarization of the plane wave incident upon the grating surface. When $\lambda/\mathtt{g} < 0.2$ and the groove depth to groove spacing ratio is small (small blaze angles for blazed grating) scalar theories can be used [35, 36]. Both types of gratings used in the grating spectrometer discussed in this thesis fall completely in the vector diffraction theory regime.

4.1 Boundary value problem of gratings

Figure 4.1 shows a sketch of a grating with the incident and diffracted wavevectors in the coordinate system oxyz. The grating has a profile ρ, of equation y=f(x), with period g = OG in x and invariant on z. The extensions in x and z are assumed to be infinite. The region $\mathtt{R}_+$ ($\mathtt{y} > \mathtt{Y_M}$) normally contains air and its index of refraction will be assumed as being equal to 1. The region $\mathtt{R}_-$ ($\mathtt{y} < \mathtt{Y_m}$) filled with a metal or a dielectric with complex refraction index ν. Suppose an incident plane wave given by (the time dependence $\exp(-\mathtt{i}\omega\mathtt{t})$ is omitted)

$$\vec{E^i} = \vec{\mathcal{A}} \cdot \exp(i\vec{k} \cdot \vec{X}) = \vec{\mathcal{A}} \cdot \exp\left[i(k_x \sin\theta - k_y \cos\theta)\right]$$
$$\vec{H^i} = \vec{\mathcal{B}} \cdot \exp(i\vec{k} \cdot \vec{X}) = \vec{\mathcal{B}} \cdot \exp\left[i(k_x \sin\theta - k_y \cos\theta)\right]$$

which illuminates the grating of Fig. 4.1 where $\vec{\mathcal{B}} = \frac{1}{\epsilon\mu_0}\vec{k} \times \vec{\mathcal{A}}$ and $\left|\vec{k}\right| = \frac{2\pi}{\lambda}$. The physical problem is to find the total fields $\vec{E}$ and $\vec{H}$ at any point. It can be shown that polarization of the incident radiation is preserved by the diffracted radiation. Starting from Maxwell equations one can formulate a boundary value problem for the magnitude of the diffracted field (in both polarizations), F, that models[1] the above physical problem

$$\begin{cases} \nabla^2 F^+ + k^2 F^+ = 0 & in\ R^+ \\ \nabla^2 F^- + k^2 \nu^2 F^- = 0 & in\ R^- \end{cases} \tag{4.1}$$

with the boundary conditions ($\mathtt{on}\ \rho$)

$$\begin{cases} F^+(x, f(x)) + F^i(x, f(x)) = F^-(x, f(x)) & TE\ mode \\ \frac{d}{d\mathcal{N}} F^+(x, f(x)) + \frac{d}{d\mathcal{N}} F^i(x, f(x)) = \mathcal{C}_p \frac{d}{d\mathcal{N}} F^-(x, f(x)) & TM\ mode \end{cases} \tag{4.2}$$

[1]The derivation of the differential equation for the magnitude of the field for both polarization is given in [34] (see appendix A).

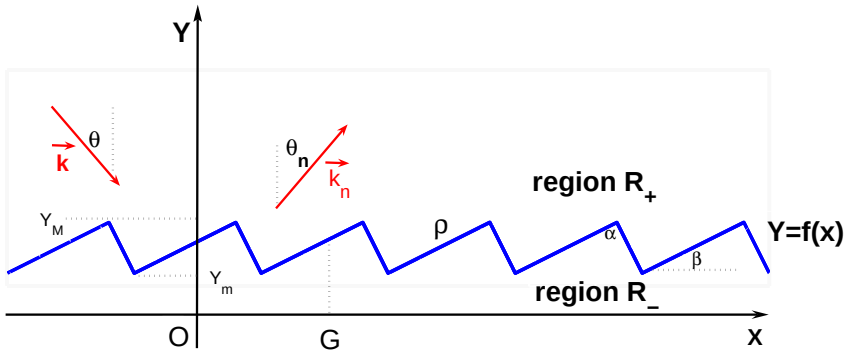

Figure 4.1: Grating physical problem. ρ shows the boundary surface of two regions R_- ($y < Y_m$) and R_+ ($y > Y_M$). An incident plane wave upon grating surface propagates along $\vec{k}$ while $\vec{k}_n$ describes the diffracted n^{th} order. The period of the function f(x) is equal to g = OG. The grating shown here is called "blazed grating". The blaze angle is denoted by β and the apex angle by α.

and $F^{\pm}$ satisfy a radiation condition[2] when $y \to \infty$ where

$$\mathcal{C}_p = \begin{cases} 1 & P\ polarized \\ \frac{1}{\nu^2} & S\ polarized \end{cases}$$

F^i is the magnitude of E_z^i (for TE mode or P polarization) or H_z^i (for TM mode or S polarization) and $\widehat{\mathcal{N}}$ is the unit vector in the direction normal to the grating surface and is pointing to the region R_+. $\frac{d}{d\mathcal{N}}$ is the directional derivative in the direction of $\widehat{\mathcal{N}}$ or $\frac{d}{d\mathcal{N}} = \widehat{\mathcal{N}} \cdot \nabla$. The boundary conditions of Eq. 4.2 are the continuity equation for the transverse field components (E_z for the TE mode and H_z for the TM mode). In [34] the solution of this boundary value problem is discussed and an overview is given in appendix A.

4.2 Distribution of dispersed radiation in a grating setup

Solution of the boundary value problem of the previous section describes the distribution of the dispersed light. A general solution is a superposition of eigenfunctions of Eq. 4.1 with boundary conditions of Eq. 4.2. Each eigenfunction is

[2]The integrated power over a large enough surface that surrounds the entire volume under consideration is finite.

called a diffraction order. Each diffraction order carries a fraction of the incident energy that is called efficiency of that order. The propagation direction of an order is given by the "grating equation" (see Eq. 4.3).

4.2.1 Grating equation

The well-known grating equation gives the angular distribution of the $\mathtt{n}^{\mathtt{th}}$ reflected order[3] as (for a derivation see appendix A.1.3)

$$\sin\theta_n + \sin\theta = n\frac{\lambda}{g} \tag{4.3}$$

One consequence of Eq. 4.3 is that wavelengths dispersed in different orders, n, propagate in the same direction if the product $\mathtt{n}\lambda$ stays the same. Then different wavelengths are mixed up which makes any recorded spectra fakery. This degeneracy problem will be discussed in more detail later in this chapter taking into consideration the role of efficiencies.

Dispersive power

Another aspect of Eq. 4.3 is the dispersive power. The quantity

$$\frac{d\lambda}{d\theta_n} = \frac{g}{n}\cos\theta_n \tag{4.4}$$

is called dispersive power. This indicates that the dispersed radiation is not uniformly distributed over the deflection angle θ_n: the larger θ_n the weaker the dispersive power. In other words, shorter wavelengths are resolved with higher resolution than longer ones. The presence of n in the denominator reveals the well known rule that for wider range coverage the lower orders are better and when higher resolution is required higher orders are more useful. Especially in the application of the subject of this thesis, the first order is very beneficial because it maximizes the range of coverage. The presence of g in the numerator tells that gratings with shorter groove period are less dispersive. This becomes important when the spectra measured in different stages of a multi-stage spectrometer should be combined. When similar detectors are used to measure the intensities in the entire dispersed radiation range[4] a normalization is necessary that converts

[3] For transmission orders this equation has the form $\nu\sin\theta_n^{(\nu)} + \sin\theta = n\frac{\lambda}{g}$.

[4] Either scanning spectrometer that uses one detector or multi-channel spectrometer that has identical detectors with identical geometrical acceptance.

the raw signal to intensity per bandwidth. It can be seen that for $\mathtt{n} = \mathtt{1}$, this normalization factor is

$$\frac{d\theta_1}{d\lambda} = \frac{1}{g\cos\theta_1}$$

4.2.2 Efficiency of different orders

The efficiency $\mathcal{E}_n$ in the $\mathtt{n}^{\mathtt{th}}$ diffracted order is defined as the ratio of diffracted energy in this order to the energy incident on the grating. In appendix A.1.3 an integral method for a perfect conductor, adapted from [34], is presented that gives the relation between $\mathcal{E}_n$ and the coefficients of eigenfunctions of Eq. 4.1.

Simulation results for the efficiency of different orders

Efficiency curves of diffraction gratings are widely used in different areas of physics and can be found in literatures e.g. [35, 37]. A powerful commercial code that can handle complicated problems of diffraction gratings is "GSolver" [38].

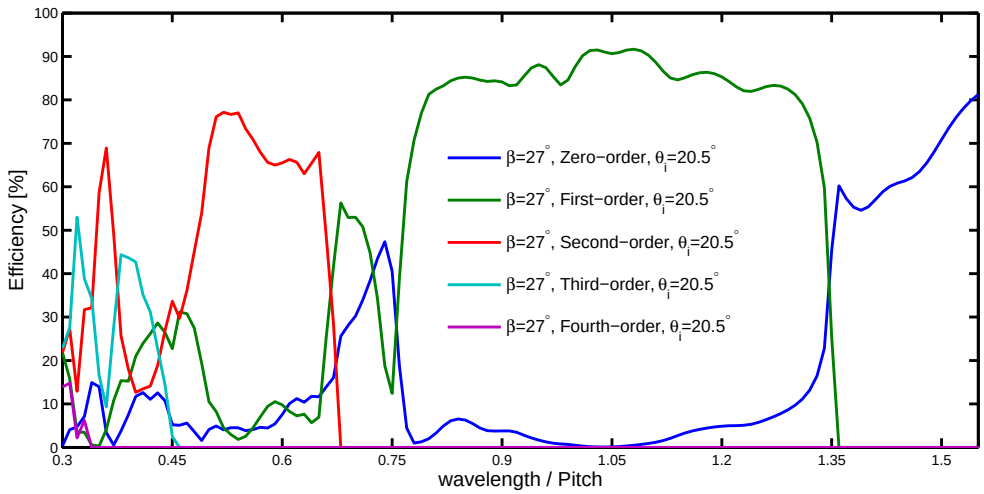

Figure 4.2: Efficiency curve of a reflectance blazed grating S-polarized incident radiation. The efficiency of the first order is larger than 50% when $\frac{\lambda}{g} \in [0.78, 1.31]$.

In Fig. 4.2, an example of efficiency curves is shown. This is for S-polarized (electric field normal to the grooves) light incident on the grating with an angle of $20.5°$ to the grating normal. The horizontal axis is the wavelength normalized to the pitch size (λ/g). There are several important features as this parameter varies over the range $0.3 < \frac{\lambda}{g}$. For $0.3 < \frac{\lambda}{g} < 0.78$, many orders carry energy and if the incident radiation contains these wavelengths they get dispersed to the entire range of deflection angles of Fig. 4.3. When $0.8 < \frac{\lambda}{g} < 1.3$, most of the radiation

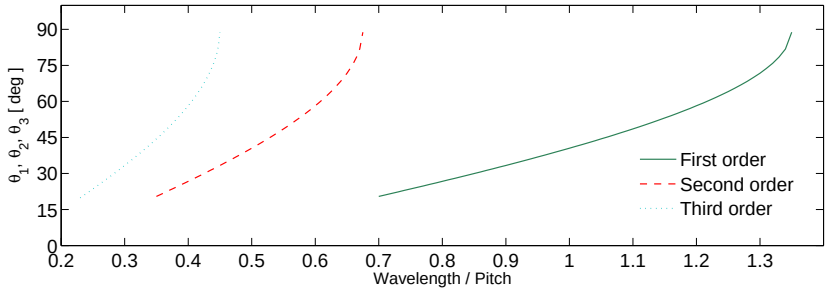

Figure 4.3: Deflection angle for the most intensive orders of Fig. 4.2

goes to first order and only a little intensity leaks to zero-order. This window can be used to record spectra if the spectral range contains wavelengths longer than $\lambda = 0.78g$. If $\frac{\lambda}{g} > 1.32$ then radiation is sent to the zero-order direction, as if the grating would be a mirror. In Fig. 4.4 the efficiency curves are shown for both S and P-polarized radiation. For P polarized light, the first-order window is not flat but more like a peak with a very narrow maximum. This shows clearly that the S-polarized radiation is much better suited to resolve a wide spectral range. If the radiation under study is not linearly polarized (like transition radiation), a polarizer with known spectral behavior should be used (see appendix C).

Angular distribution as a function of wavelength

Equation 4.3 describes the propagation direction as a function of wavelength. At first glance, one may conclude that the radiation distribution does not depend on details of the grating surface shape. As long as Eq. 4.3 is concerned this is true, but efficiencies need to be considered as well. Depending on the details of the groove geometry, efficiencies change and accordingly, unlike the prediction of Eq. 4.3, there might be no intensity appearing in an order for some wavelengths. The incident radiation shows up only in orders that have non-zero efficiencies. Therefore for a complete description of the energy distribution both the grating equation and efficiencies have to be considered.

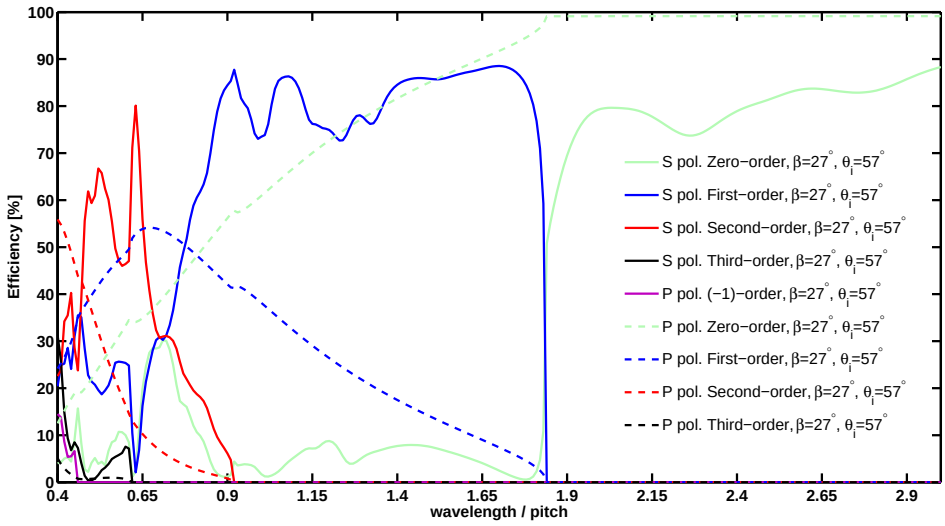

Figure 4.4: Efficiency curves of a reflectance blazed grating. The results corresponding to S and P-polarized incident radiations shown as solid and dashed lines, respectively. Green, blue and black correspond to zero, first and second orders, respectively. For S-polarized radiation the first order efficiency is larger than 50% when $\frac{\lambda}{g} \in [0.75, 1.8]$.

4.3 Design considerations for broad-band grating spectrometer

In the ordinary applications of the reflectance gratings (e.g. monochromators), a blaze-wavelength condition (Littrow mount[5]) is satisfied to maximize the efficiency by a proper selection of the angle of incidence on the grating (e.g. rotating the grating to obtain the blaze wavelength condition for different wavelengths). When it is desired to resolve broad-band polychromatic radiation (like coherent radiation of the electron bunches) in a single shot mode, the angle of incident on the grating is fixed. This requires optimizations in terms of a proper design of the grooves and angle of incidence on the grating. In other words, the widest first-order dispersive window with high efficiency that exhibits minimum intensities leaking into other orders is desired. The dispersed radiation into first order extends over a large angular spread and may, without a careful design, overlap with the incident radiation. In addition, the optimized configuration should provide a sharp change from the dispersive window to the range of longer wavelengths that propagate (with high efficiency) to the specular reflection. In order to use the long wavelengths that are sent to the zero-order (the specular reflection) in a next stage this region has to be kept free from any other diffraction order.

Restriction on the angle of incident

In a non Littrow mount the dispersed radiation in first order may overlap with the incident radiation. In Fig. 4.4 the angle of incident is optimized to achieve the broadest high-efficiency first-order dispersive range. The dispersed radiation propagates in the direction $\theta_1(\lambda)$ where $3^\circ < \theta_1(\lambda) < 75^\circ$. This imposes on complications in the design of collecting optics of the dispersed light when the incident radiation is broad-band polychromatic (like the spectra of coherent radiation of the electron bunches in a linac-driven FEL). An intuitive simple solution is to orient the dispersed light out of the plane of incident radiation. This arises a lot of complication with conical diffraction from the gratings. The solution is to make a compromise between efficiency and the angular spread of the dispersed light. With the angle of incident $\theta_i = 19^\circ$ the dispersed radiation spans the range $27^\circ < \theta_1(\lambda) < 78^\circ$. The efficiency curves are very close to those of Fig. 4.2. A setup with $\theta_i = 57^\circ$ has been used in the experimental verification of efficiency curves at FELIX (see chapter 8).

[5] A first-order Littrow mount is when the first order dispersed radiation coincides with the incident radiation ($\theta_1 = -\theta$ in Fig. 4.1).

4.3.1 Staging of gratings to achieve broad-band coverage

The arguments of section 4.2.2 suggest a way to use the reflectance grating in a non Littrow mount to do single shot spectroscopy of broad-band radiation. Suppose the incident radiation is composed of wavelengths longer than λ_0. If the first order dispersive window starts at λ_0 for a reflectance grating with the pitch size of g it resolves the spectra to a wavelength λ_1 such that $\lambda_1 > \lambda_0$ (in reference to Fig. 4.2, which is for an incident angle of $\theta_i = 20.5^\circ$ on the grating, $\lambda_0 = 0.78g$ and $\lambda_1 = 1.31g$ which results in $\lambda_1 = 1.65\lambda_0$). Then for wavelengths longer than λ_1 the entire, not yet resolved, radiation goes to zero-order where the grating acts like a mirror. This reflected radiation can be send to the next grating with appropriate grating geometry to repeat the same process until the region of interest is covered. A very important objective in the design of the grooves and the layout arises in this context. The direction of the specular reflection has to be free of any diffracted order. This staging concept is shown in Fig. 4.5.

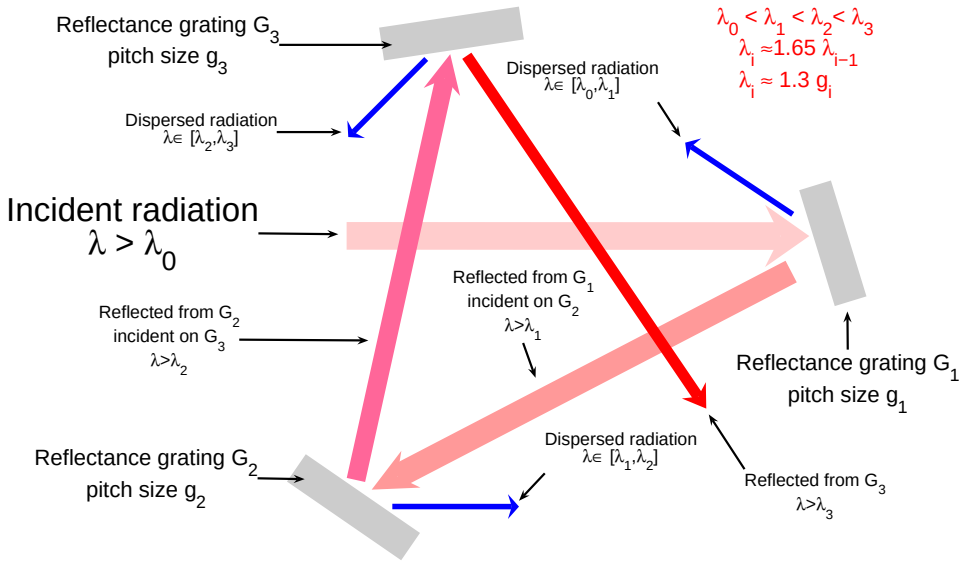

Figure 4.5: A multi-stage mount of reflectance gratings. An incident radiation (S-polarized) composed of wavelengths longer than λ_0 illuminates the grating G1 with a pitch size g_1. The wavelength range $[0.78g_1, 1.31g_1] = [\lambda_0, \lambda_1]$ is then dispersed to the first-order and radiation composed of wavelengths longer than λ_1 can be send to the next grating G2 to repeat the same process. In the setup that is shown in the sketch three stages are mounted.

Definition of a stage

The bandwidth that can be resolved by a single grating (either transmission or reflectance) is given by the specifications of the grating. Therefore it is reasonable to define for any grating setup the number of stages as the number of gratings in the optical path.

4.3.2 Design of the optimum grooves

As for the choices of the geometry of the grooves there are different options: rectangular (lamellar grating) , sinusoidal (holographic gratings) and triangular (blazed grating). Lamellar gratings have low efficiencies (the maximum first order efficiency is about 40%). Holographic gratings are not as efficient as blazed gratings and they are not easily available in the FIR range. Blazed gratings have the highest efficiencies and it is possible to rule them with groove sizes in the range of a fraction of a micrometer to several millimeters. The geometry of the grooves with a known groove length, g, can be distinguished by the blaze angle β and apex angle α (see Fig. 4.1).

Selection of the blaze angle

In Fig. 4.6 the efficiencies of the most intense orders for blazed gratings with different blaze angles are shown in a Littrow mount. The result for a non Littrow mount (fixed angle of incident) is shown in Fig. 4.7. In both cases it can be seen that the average first order efficiency is maximum for $\beta = 27^\circ$ with a minimum variation over first-order dispersive range.

How to orient the gratings

A simple failure that may happen during the mounting of a blaze grating is to mix up the orientation of the grooves. A typical blazed grating may have several hundred grooves per millimeter which makes it difficult to see the grooves without appropriate tools. With an apex angle of $\alpha = 90^\circ$, the grating with blaze angle β can be used as a grating with blaze angle $\frac{\pi}{2} - \beta$. In Fig. 4.8 this circumstance is simulated and it can clearly be seen that the orientation of the gratings plays an important role.

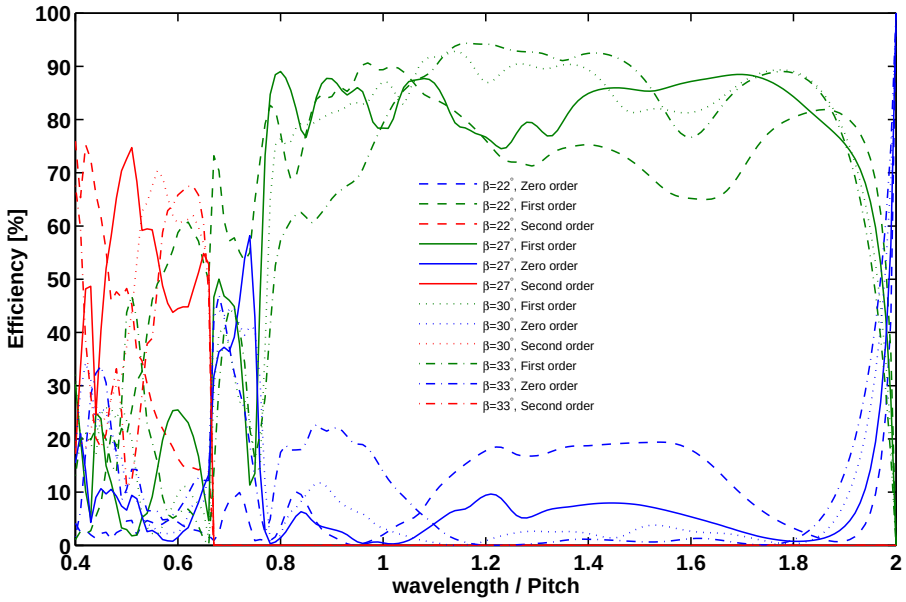

Figure 4.6: Optimization of dispersion versus blaze angle in a Littrow mount.

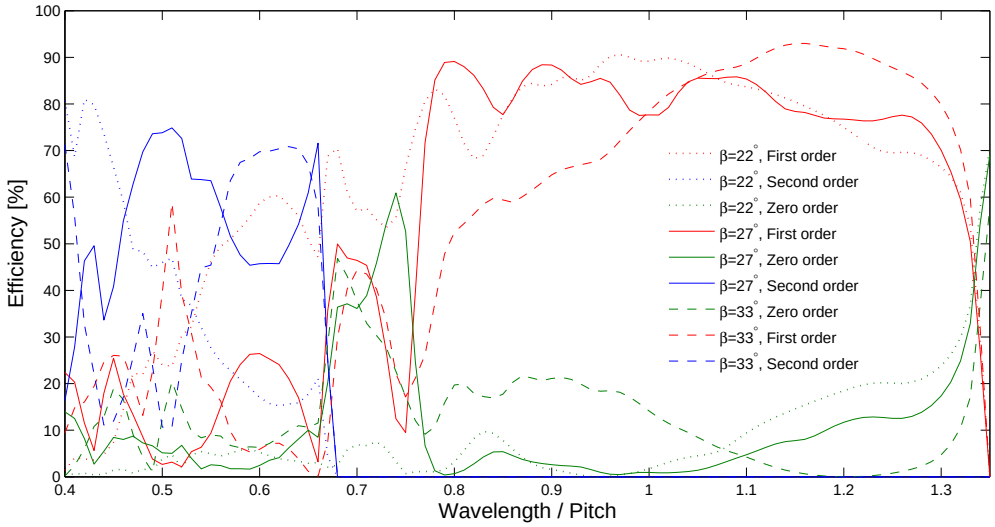

Figure 4.7: Optimization of dispersion versus blaze angle in a non-Littrow mount.

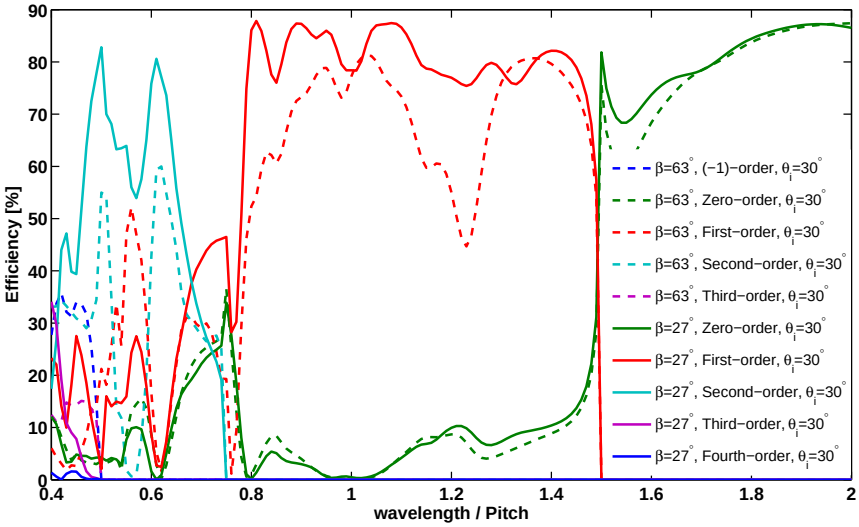

Figure 4.8: How to orient the grating with respect to the incident radiation.

The role of apex angle

Another degree of freedom in the design of the triangular grooves is the apex angle α. In Fig. 4.9 the efficiency for three apex angles of 80°, 90° and 100° has been calculated. The first-order curve that shows a flat, high efficiency corresponds to $\alpha = 90°$.

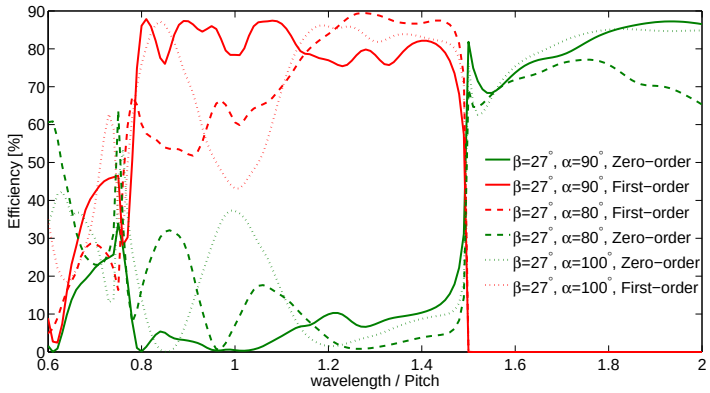

Figure 4.9: Influence of apex angle on the efficiency

4.4 Transmission gratings

The simplest type of Transmission Grating (TG) is a piece of rectangular metallic plane that has parallel slits of width a with a spacing of period g. In the approximation of scalar diffraction theory, the intensity distribution for a set of N parallel slits is given by

$$I \propto \left[\frac{\sin(ua)}{ua}\ \frac{\sin(Nug)}{\sin(ug)}\right]^2 \tag{4.5}$$

with $\mathtt{u} = \frac{\mathtt{kx}}{\mathtt{2R}}$ where k is the wavenumber, x is distance in the observation plane from the origin in the direction perpendicular to the slits and R is distance from the grating to the observation plane (Fig. 4.10, top). It can be seen from Eq. 4.5 by substitution $\mathtt{g} = \mathtt{2a}$, i.e. the slit width equal to the metallic strip width, that the diffraction pattern has only one strong component (first-order) in addition to the intense central region of zero-order. For such a transmission grating the total intensity that appears in the first-order (one of the two identical transmission orders which are sketched in Fig. 4.10 bottom) is about 13% of the incident radiation. The free spectral range[6] seems to be very broad: it is limited towards long wavelengths by the pitch size g and towards short wavelengths by the incident beam spot size[7]. The grating equation Eq. 4.3 with $\theta = 0$ takes the simple shape $\sin\theta_{\mathtt{n}} = \frac{\mathtt{n}\lambda}{\mathtt{g}}$ for TGs.

For real TGs the ratios wavelength over pitch ($\lambda/\mathtt{g}$) and thickness over pitch ($\mathtt{h}/\mathtt{g}$), determine the range of validity of the scalar theory results. For $\frac{\mathtt{h}}{\mathtt{g}} > \mathtt{0.2}$, scalar theory results cannot be used.

In order to get some insight into the vector diffraction theory description of transmission gratings the approach of previous section is applied to this problem and two sample results are shown in Fig. 4.11, for a TG with pitch size $\mathtt{g} = \mathtt{200}\ \mu\mathtt{m}$ and $\frac{\mathtt{h}}{\mathtt{g}} = \mathtt{0.05}$ and pitch size $\mathtt{g} = \mathtt{100}\ \mu\mathtt{m}$ and $\frac{\mathtt{h}}{\mathtt{g}} = \mathtt{0.1}$. It is evident that for thin TG the suppression of higher orders is stronger and for gratings that can be realized in practice[8], the free spectral range is not very large.

Transmission gratings of the described type are very useful to resolve the part of the radiation with relatively long wavelengths. When they are made thin enough to suppress the higher orders, they are daintily refined and hard to incorporate

[6] Free spectral range is a continuous range of wavelengths over which there is only a specified diffracted order.

[7] The zero-order spot has the same size as incident beam and shades the short wavelengths.

[8] One technique to fabricate such gratings is to cut, by a laser, slits out of a metallic sheet. This has limitations in the achievable pitch size and thickness. The current values that have been reached by the producer of these gratings are $\mathtt{g}_{\mathtt{min}} = \mathtt{100}\ \mu\mathtt{m}$ and $\mathtt{h}_{\mathtt{min}} = \mathtt{10}\ \mu\mathtt{m}$.

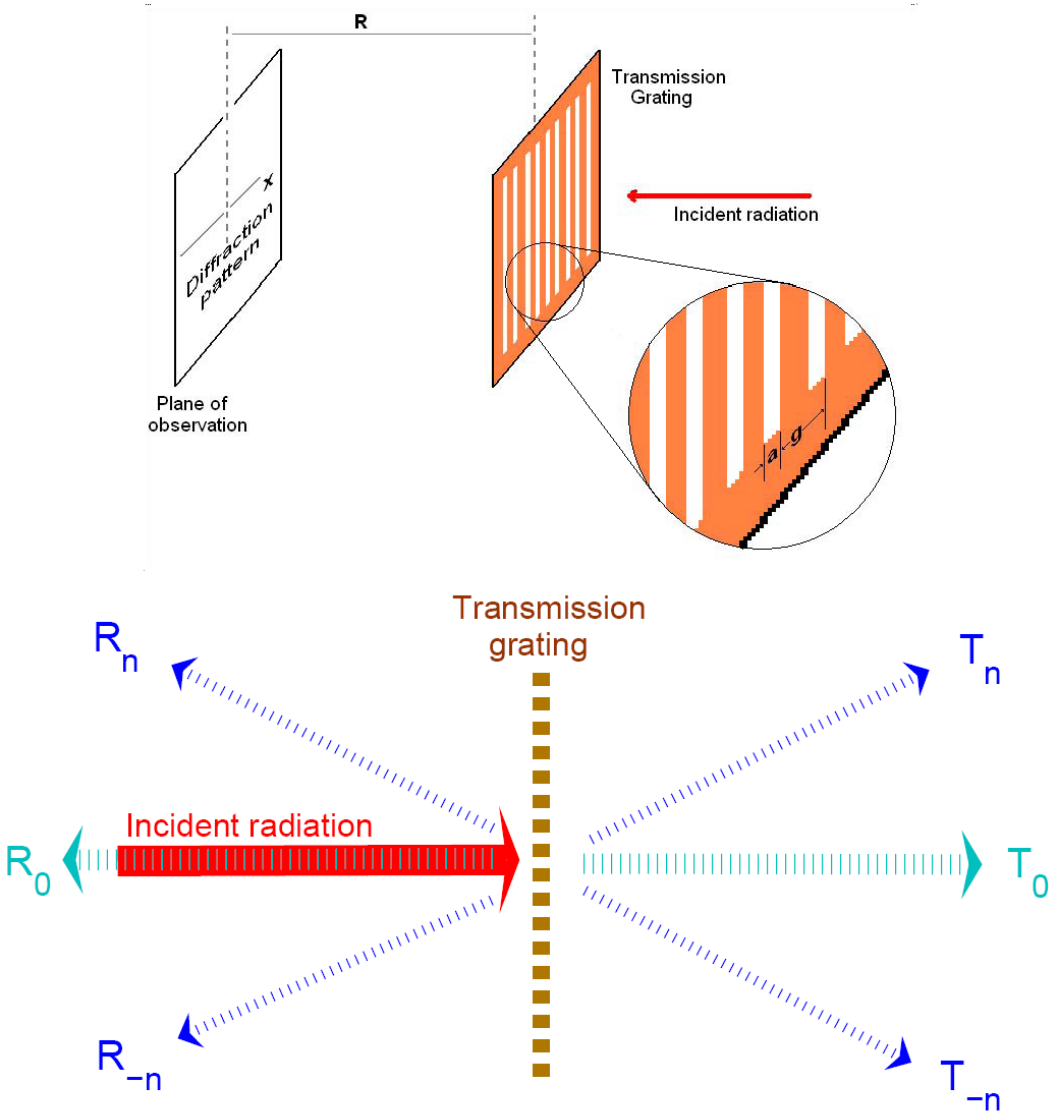

Figure 4.10: Transmission grating with strongly suppressed higher orders is obtained with $\mathtt{g} = \mathtt{2a}$. Bottom: Different transmission ($T_i, with\ i \in \mathbb{Z}$) and reflection ($R_i, with\ i \in \mathbb{Z}$) orders diffracted by a transmission grating.

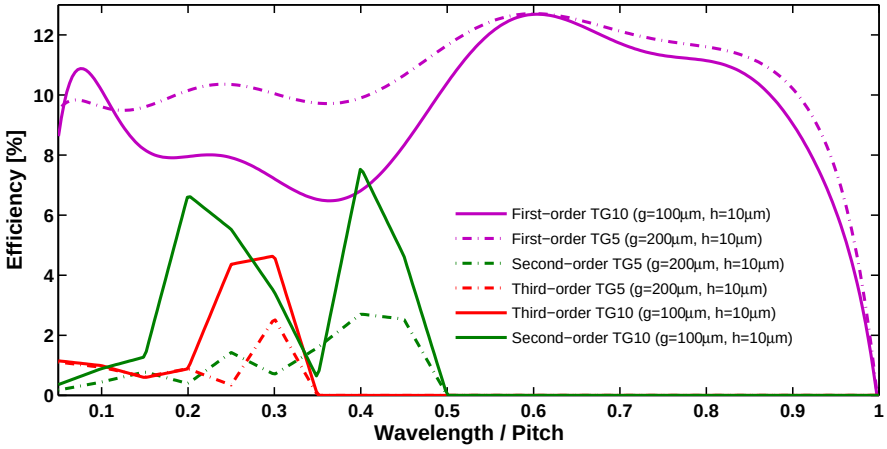

Figure 4.11: Efficiency curves of transmission gratings with pitch size of $g = 200\ \mu m$, $\frac{h}{g} = 0.05$ (TG5) and $g = 100\ \mu m$, $\frac{h}{g} = 0.1$ (TG10). h is the thickness of the grating.

in a mount. For wavelengths shorter than 15 μm technical realization of TGs becomes hardly feasible.

Chapter 5

Room Temperature IR Detectors

A detector is a device that provides an electrical output that is a measure of the radiation intensity incident on the device. Depending on the target wavelength range, the intensity level and type of spectroscopy, a suitable detector needs to be chosen.

General requirements

As is described in section 1.2, the distance between successive bunches during routine operation at FLASH is as short as 1 μs. The spacing between the bunches will reduce to 200 ns for the European XFEL [39]. Therefore the entire method of single shot detection should be as fast as 1 μs for FLASH and have the potential to be reduced to 200 ns for the XFEL.
The other important issue is the intensity level that should be detected by the individual detectors of the grating spectrometer. Simulation results show that the spectral range of the coherent radiation that corresponds to the spike in the bunch profile is at wavelengths shorter than $\approx$ 200 μm. For this spectral range the minimum intensity level to be detected can be estimated. For a fixed geometrical aperture of the detector, the signals at longer wavelengths are integrated over a narrower frequency bandwidth (see Eq. 4.4). Consider an electron bunch with a total charge of 1nC (with a normalized electron energy of $\gamma = 1000$). With the assumption that 10% of the charge are confined in the spike of the asymmetric bunch profile, the number of electrons that radiate coherently can be calculated. For the single electron spectral density the value $\approx 10^{-7}$ $\frac{\text{eV}}{\text{GHz}}$ can be used (see Fig. 3.2). Then Eq. 3.3 can be used to calculate the radiation intensity by the electron bunch at the source. For a wavelength of 200 μm, Fig. 8.2 shows a transmission of 80% for the THz beamline and Fig. D.1 a transmission of 70% of the

diamond window. The polarizer blocks half of the intensity and the efficiency of the grating is about 80%. The other factor is the bandwidth over which the geometrical aperture of the detector integrates. The angular spread of the detector aperture is 2° or 35 mrad. From Eq. 4.4 with $\lambda = 200\ \mu\mathrm{m}$, $g = 127\ \mu\mathrm{m}$, $\theta = 80^\circ$ and $\Delta\theta = 35\ \mathrm{mrad}$, the frequency bandwidth of $\Delta f = 6\ \mathrm{GHz}$ can be obtained. The final result for the minimum radiation intensity at the individual detectors is $\approx 8\ \mathrm{nJ}$.
Other important requirements are: The detector unit needs to be an array of detectors that are located close to each other along the path that is given by the collecting optics. In order to avoid water absorption lines (see Fig. D.2) the entire detector unit should be usable under vacuum condition of the level of $\leq 10^{-1}\mathrm{mbar}$.
In the following sections the detection mechanism of some THz-radiation detectors is discussed.

5.1 Pyroelectric detector

The pyroelectric effect

Among the crystals of noncentrosymmetrical structure there are ten classes that can exhibit spontaneous electric polarization[1]. In particular, if the temperature of the crystal is changed, the dipole moment may also change and result in an external electric field. For conductors, the mobile charge carriers rearrange quickly such that there will be no external electric field. However if the crystal is an insulator, stray charges will be attracted to and trapped on the surface until the surface charge associated with the polarization is neutralized. This process is not very quick and the relaxation time of the crystal is long enough to detect the resulted external electric field. The coefficient that relates the polarization charge to the temperature change is called pyro-coefficient. In other words, the pyro-coefficient is the rate of change of polarization with temperature at constant stress. In general the pyro-coefficient depends on the temperature but the changes are about 0.5% per one degree of the changes at the equilibrium temperature [41] and will be neglected in this thesis.
There are different ways to use the pyroelectric effect for signal detection. One way is to use the pyroelectric element to store the total charge liberated by a transient signal. In Fig. 5.1 a drawing of a pyroelectric sensor is shown. The top black layer, which is used to make the detector more suitable to measure the

[1] These crystals are all piezoelectrics.

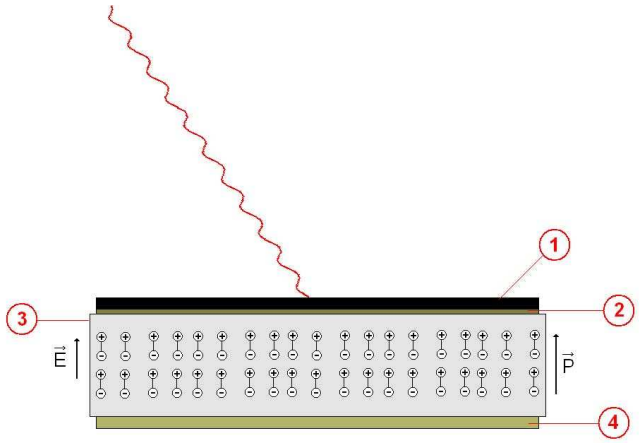

Figure 5.1: The pyroelectric sensor is composed of several layers. 1- Black coating material, for storing the incident energy. 2- Chromium layer acts as one of the two electrodes. 3- The pyroelectric crystal 4- The metallic electrode layer. Incident radiation heats the black layer and/or pyroelectric crystal. The absorbed energy makes a temperature change which produces the polarization charge due to pyroelectric effect. Then the resultant electric field can be detected by means of a suitable preamplifier.

total energy[2], is followed by a thin metallic layer that acts as an electrode of the capacitor. The next layer is the pyro-crystal which produces a polarization charge dependent on the temperature change. The bottom layer is the second electrode of the capacitor. The detector of Fig. 5.1 can be integrated in a circuit as demonstrated in Fig. 5.2. The left part shows the pyro-sensor and the preamplifier, and the equivalent circuit for the sensor and preamplifier in the right.

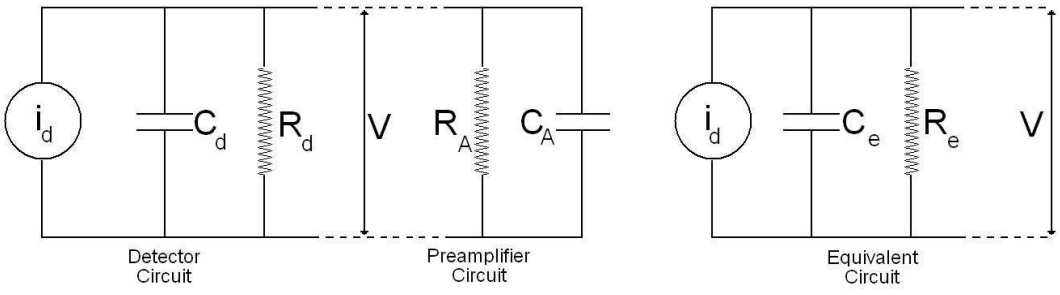

Figure 5.2: Equivalent circuit for pyroelectric detector and amplifier input.

[2]A pyroelectric detector can be used as a movement detector. This is an example application that it is not necessary to measure the total energy. The black layer (which is black only in relatively short wavelengths close to visible) does not absorb all the radiation in far infrared.

5.1.1 Pyroelectric detector characterization

In order to characterize the pyroelectric detector, both the thermal and electrical circuits must be considered. When the responsive element absorbs an amount of infrared radiation, its temperature rises, changing its surface charge. With the appropriate external circuit, this change in surface charge leads to a signal voltage.
For a given thickness of a pyroelectric crystal, electroded on both sides, the non absorbed part of primary incident radiation might be reflected back into the crystal when it reaches the metallic bottom electrode (etalon effect). This enhances the absorbed intensity in the crystal and generates an additional wavelength dependent resonance.

Thermal and electrical circuits

The change in temperature, $\mathtt{\Delta T}$, of the responsive element is related to its thermal capacitance, C_T, and its thermal conductance, $\mathcal{C}$, by the following equation:

$$C_T \frac{d}{dt}\Delta T + \mathcal{C}\Delta T = \Phi \tag{5.1}$$

where Φ is the absorbed incident, infrared radiation power. The solution (absolute value of the solution) of this equation for a harmonic Φ, is

$$|\Delta T| = \frac{[1+\omega^2(\frac{C_T}{\mathcal{C}})^2]^{-1/2}}{\mathcal{C}}\Phi \tag{5.2}$$

where ω is the angular frequency of Φ[3]. This analysis assumes that the radiation is absorbed uniformly throughout the sample[4]. For a periodic incident infrared radiation, Putley [43] has derived the voltage responsivity, $\mathcal{R}_\mathcal{V}$, for a pyroelectric detector in terms of $\mathcal{V}$, the preamplifier output voltage:

$$\mathcal{V} = \frac{\rho\omega A_d \Phi R_e}{\mathcal{C}}[1+\omega^2\tau_T^2]^{-1/2}[1+\omega^2\tau_e^2]^{-1/2} \tag{5.3}$$

as

$$\mathcal{R}_\mathcal{V} = \frac{\mathcal{V}}{\Phi} \tag{5.4}$$

where ρ = pyro-coefficient, $\mathtt{A_d}$ = sensitive area of the responsive crystal, $\mathtt{R_e}$ = equivalent input resistance of the detector-preamplifier circuit, $\mathtt{C_e}$ = equivalent

[3]The relation between the incident radiation power Ψ and the absorbed power Φ is $\Phi = \epsilon\Psi$, where ϵ is the effective emissivity of the sensor.

[4]If the heating is nonuniform, the responsive element can be split into layers of different temperature, then the average temperature change can be used in Eq. 5.2 [42].

capacitance and $\tau_{\mathtt{T}} = C_T/\mathcal{C}$, $\tau_{\mathtt{e}} = \mathtt{R_e C_e}$ are thermal and electrical time constants, respectively. When the incident infrared radiation is a short pulse compared to the repetition rate[5], the periodic pulse formalism is not applicable and the solution of the Eq. 5.1 for a short pulse of incident radiation has to be considered. In references [44, 45] the pyroelectric response to single infrared laser pulse as a function of time constants and the parameters of the signal is described. In Fig. 5.2 the charge flow can be described by

$$C_e \frac{dV}{dt} + \frac{V}{R_e} = \frac{dQ}{dt} \tag{5.5}$$

and for voltage response V

$$\frac{dV}{dt} + \frac{V}{\tau_e} = \frac{A_d}{C_e}\rho\frac{dT}{dt} \tag{5.6}$$

For sufficiently small loads[6], $\tau_{\mathtt{e}} \ll \tau_{\mathtt{T}}$, the solution of $\mathtt{V(t)}$ with the boundary conditions $\Phi(0) = V(0) = 0$ is given by

$$V(t) = \xi \exp(-t/\tau_e) \int_0^t \exp(t^{'}/\tau_e)\Phi(t^{'})dt^{'} \tag{5.7}$$

where $\xi = \frac{\rho A_d}{C_T C_e}$ is a constant for any sensor-amplifier set. A typical radiation pulse of coherent radiation produced by electron bunches is of the length of a few picoseconds, therefore τ_e is much longer than the entire pulse duration. The exponential term in Eq. 5.7 can then be replaced by 1,

$$V(t) = \xi \textstyle\int_0^t \Phi(t^{'})dt^{'}$$

i.e. the response is rising as long as the signal persists. At the end of the signal, $V(t)$ reaches a peak value $V_p = \xi \int_0^{t_s} \Phi(t^{'})dt^{'} = \xi I_{abs}$, which is proportional to the energy absorbed from the radiation pulse, $\mathtt{I_{abs}}$, and independent of $\mathtt{R_e}$.

Pyroelectric resonances

In early usages of pyroelectric detectors, at most, a few discrete laser frequencies were under study. Later, the increasing interest to study more frequencies

[5] When one electron bunch is kicked out of the train, with the repetition rate of 5 Hz for the trains, the 200 ms time between successive shots is of the same order as $\tau_{\mathtt{T}} = \mathtt{C_T}/\mathcal{C}$. This is different to an `1MHz` operation of the pyro-preamplifier where the thermal circuit cannot relax as fast as $\mathtt{1}\ \mu\mathtt{s}$.

[6] Any thermal effects occur on time scales many orders of magnitude slower than the electrical signals.

initiated the need to have these detectors calibrated over a wider range. Since at least 2 decades the need to characterize pyroelectric detector, including their resonances, has been realized [46]. The layers of a pyroelectric sensor are composed of different materials. The optical properties of these materials determine the transmission and absorption of the radiation. In each interface between two adjacent layers reflection and transmission occur. For a multi-layer slabs of different materials one has to carry out careful simulations of total absorption and transmission coefficients [47, 48, 49]. The results of such calculations are strongly dependent on the knowledge of the optical properties of the materials of the different layers and their thicknesses. For some of these layers which are evaporated on the substrate one needs to know the optical properties of the evaporated type of the material which normally happens to be different than the normal material. Unfortunately, these properties are not available over the whole range of interest, making it more complicated to use the simulation results. In Fig. 5.3 the

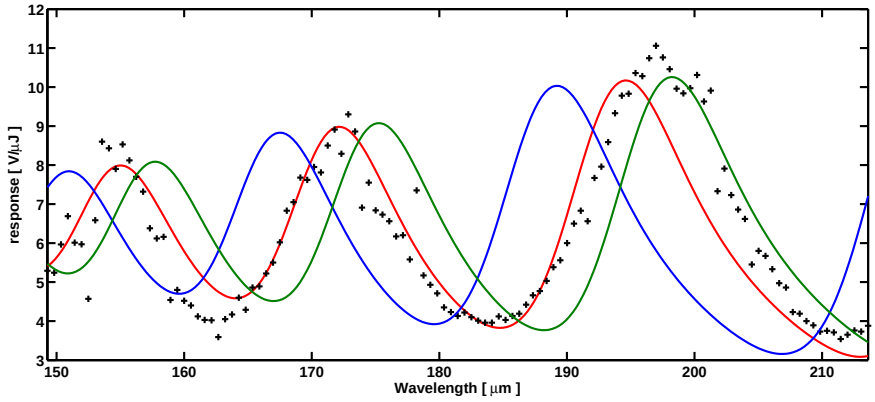

Figure 5.3: Dependency of the response voltage on the crystal thickness for a $LiTaO_3$ pyroelectric detector over the range 150 to 215 μm[7]. According to the crystal specifications, its thickness in the direction of the pyroelectric axis should be between 95 to 100 μm. The experimental result is shown as points; the blue, red and green curves are calculated for crystal thickness of 95, 98 and 100 μm, respectively. Calculations for the etalon resonances are carried out in the same way as it is described in references [46, 47] by O. Grimm.

result of a measurement for the responsivity of a $LiTaO_3$ pyroelectric detector is shown in comparison with the result of simulation. The three curves correspond to simulation results for crystal thickness of 95, 98, 100 μm in the direction of

[7]The experimental result is from a DTGS pyroelectric detector calibration performed at FELIX [50].

pyroelectric axes. The best fit to the experimental result corresponds to 98 μm which is shown in red. The change of response voltage as a function of crystal thickness is large and this means that experimental calibration is mandatory for each individual detector.

5.2 Thermopneumatic detectors (The Golay-cell)

In this detection process, a material (e.g. aluminized cellulose with 200 nm thickness) that absorbs the infrared radiation is placed in a chamber filled with a gas (typically Xenon), see Fig. 5.4. A window (diamond) in one of the walls of the chamber couples the incident radiation on the absorbing material. The irradiated absorber heats up and by conduction heats the gas. The gas inside the chamber expands and distorts a flexible mirror that is mounted as one of the walls of the chamber. Finally a detection system composed of another detector and a source of light, measures the degree of the distortion on the mirror. Golay [51, 52, 53] has described the theory of operation for this type of detector. The physics of

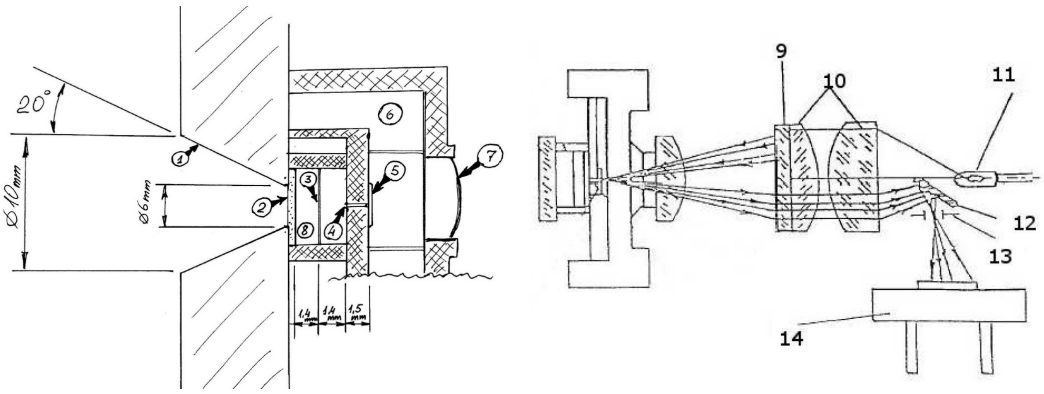

Figure 5.4: Sketch of a Golay cell detector taken from [54]. Right: the entire detector including the mechanism that measures the distortion on the flexible mirror; left: a zoom to the thermopneumatics detector is seen.
1. Polished metal input cone to increase the radiation angular acceptance 2. Input window 3. Absorbing film 4. Signal and compensation channel 5. Sensitive mirror membrane 6.Vacuum chamber 7. Objective 8. Gas chamber 9. Grid 10. Double-lens system 11. LED 12. Mirror 13. Grid 14. Photocell.

the Golay-cell detector suggests a flat response as a function of wavelength. This has been investigated and to a high extent, confirmed experimentally. The flat

response function is a big advantage for such a room temperature detector and makes it a reference detector. For the studies on the resonances of the responsivity of the other detectors one could use the Goaly-cell detector [46].
There are some disadvantages of the Golay-cell as a detector for the grating spectrometer. First of all, when the operation in vacuum is desired, this detector is not robust. Secondly, the available detectors of the Golay-cell type are relatively slow such that, for instance at FLASH, they can be used only to study the macro-pulses[8]. Finally, the realization of an array of Golay-cell detectors, if not impossible, is hard to achieve. For these reasons, Golay-cell is not considered as the detector for the single shot grating spectrometer. A recent work on the characterization of the Golay-cell detector can be found in reference [54].

[8]As it is mentioned in chapter 6 a Golay-cell detector can be used with the RMS device. Using such configuration of RMS, several studies including the comparison of CTR and CDR have been made (see Fig. 8.12).

Chapter 6

Grating Spectrometer

In this chapter the technical layout of the grating spectrometers are described. The principles that are applied here for the spectroscopy in the infrared spectral range can easily be extended to other parts of the electromagnetic spectrum. High-resolution one-stage spectrometers can be designed either narrow-band and single-shot or wide-band but non single-shot.

6.1 Rotating mirror spectrometer

The distribution of dispersed radiation in a diffraction grating setup described in chapter 4 suggests the design of the collecting optics that focuses this radiation to the detection unit. A THz longitudinal diagnostics of electron bunches can be realized by two types of spectrometers: scanning or single-shot spectrometers.
Figure 6.1 shows a schematic of the Rotating Mirror Spectrometer (RMS)[1]. An off-axis focusing mirror can be used to collect the dispersed components of the light incident on the grating. To capture different wavelengths, such a mirror, oriented with its axis along the radial dispersed rays, has to be moved along the arc that is centered at the center of the illuminated region of the grating in the optical plane. The angular extension of this arc should be large enough to cover the entire range of the dispersed light. A detection unit can be mounted at the focus of the rotating mirror to give a signal corresponding to the incident intensity at different angles (and corresponding wavelengths). An RMS is such a device that has in addition the possibility to move, remotely controlled, the detection unit on a three dimensional linear mover. A hexagonal rotation stage with six

[1]RMS with Reflectance Blazed Gratings is shortly called RMS-RBG and similarly RMS with Transmission Gratings is called RMS-TG.

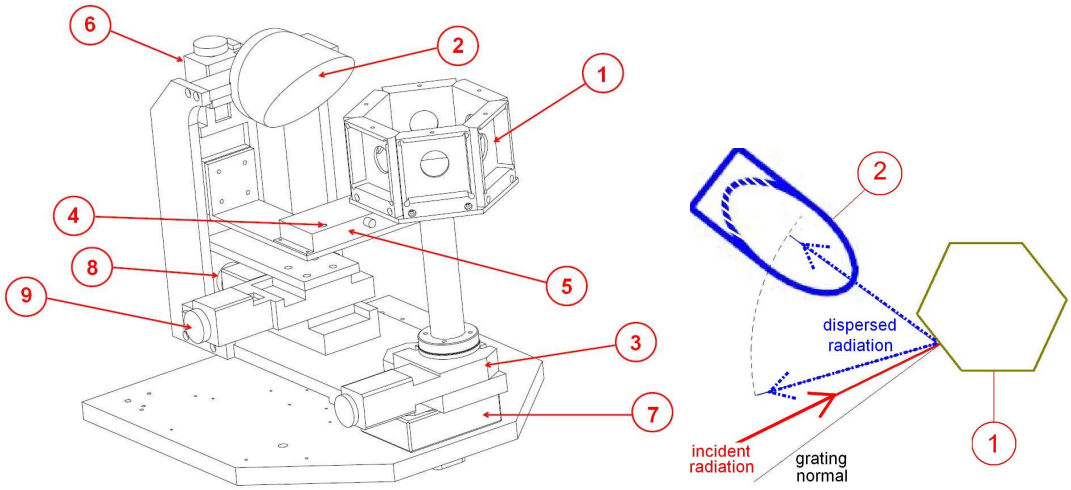

Figure 6.1: Rotating mirror spectrometer; reflectance blazed grating mount.
1- Holder for reflectance gratings of six different pitch sizes
2- 90° off-axis parabolic mirror
3- Mover for Gratings holder
4- Detector sensor and cone
5- Detector box
6- Mover to adjust the focus on the sensor
7- Mover to rotate the detection unit along the arc
8- Mover to adjust the distance from mirror to the grating
9- Mover to move along the tangential to the arc

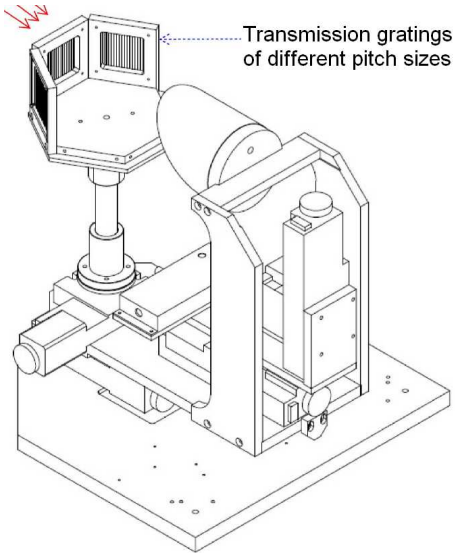

Figure 6.2: Rotating mirror spectrometer; transmission grating mount.

grating holders is placed such that when the incident radiation illuminates the grating the center of the spot on the grating is at the center of the circular path of the arc. When six gratings of different pitch sizes are placed on the holders it is possible to cover about six octaves of the wavelength range (with each of the gratings having a free spectral range of ≈ 2).
The optimal focus of the incident radiation to the diffraction limited spot size is wavelength dependent. In chapter 4 it was shown that for the designed reflectance grating setup and in first order, the interval $[0.78\lambda_0, 1.31\lambda_0]$ where λ_0 is the central dispersed wavelength (see chapter 4), is the largest possible range that can be resolved with a specific reflectance grating. Simulations show that the wavelength dependence of the focus over such a range is small enough to be compensated with a cone that slightly enlarges the geometrical acceptance of the detection unit[2]. In order to cover an entirely different wavelength range it is necessary to change the grating. One of the movers of the RMS (the mover 6 in Fig. 6.1) is foreseen to have the possibility to change the distance from the mirror to the detection unit. The other two directions in the set of detector movers are for the tangential to the arc and the distance to the center of the spot on the grating from the center of the mirror.
The detection unit can house either pyroelectric or Golay-cell detectors. This gives the possibility to cross check detectors that work based on entirely different physics and, for instance, get some insight into the detector response. The signal from the detector amplifier goes directly to an ADC which is integrated in the distributed read-out and control-system at FLASH [56]. A MATLAB control script is used as an interface to act on the movers, and register the sampled signal to a file or produce online plots from the data.
The grating holders can be changed to use either transmission or reflectance gratings. In reflectance grating mount, there are two hexagonal heads each with six grating holders. One set of six gratings is to filter the short wavelengths out of the incident radiation and the second head, right at the center of the arc, is used to disperse the radiation. In other words, when it is desired to resolve wavelength range $[0.78\lambda_0, 1.31\lambda_0]$ where λ_0 is the central dispersed wavelength, in the dispersive head one has to have a grating with a pitch size of about λ_0 while the filter head has to filter shorter wavelengths using a grating of a pitch size close to λ_1 where $1.31\lambda_1 \cong 0.78\lambda_0$ (see Fig. 4.2).
A head used in transmission mode can be equipped with a maximum of three gratings, otherwise the dispersed radiation gets blocked (Fig. 6.2). In practice assembling a setup composed of heads and RMS, as well as its alignment and

[2] A calculation based on pure geometrical considerations results in a design criterion of an optimal collecting cone (see appendix E)

wavelength calibration needs a lot of effort. Figures 6.1 and 6.2 show RMS-RBG and RMS-TG, respectively. When the heads rotate, in addition to a changed angle of incident, the position of the illuminated region on the gratings changes. This additionally complicates the alignment of the entire spectrometer. A newer version of RMS[3] has linear movers that is a copy of the two stage single shot spectrometer (see Fig. 6.13).

6.2 Prototypes of single shot spectrometer

The second type of spectrometer, the single shot spectrometer, can be realized by putting several detectors at the focus of the mirrors which are oriented radially to collect the dispersed radiation by the grating. In the following two devices that use this concept are explained.

6.2.1 Eight-channel single shot spectrometer

The one-stage eight-channel single-shot spectrometer was the first device with which the short wavelengths in the coherent transition radiation of the electron bunches were measured. Figure 6.3 shows the layout of the device in left and

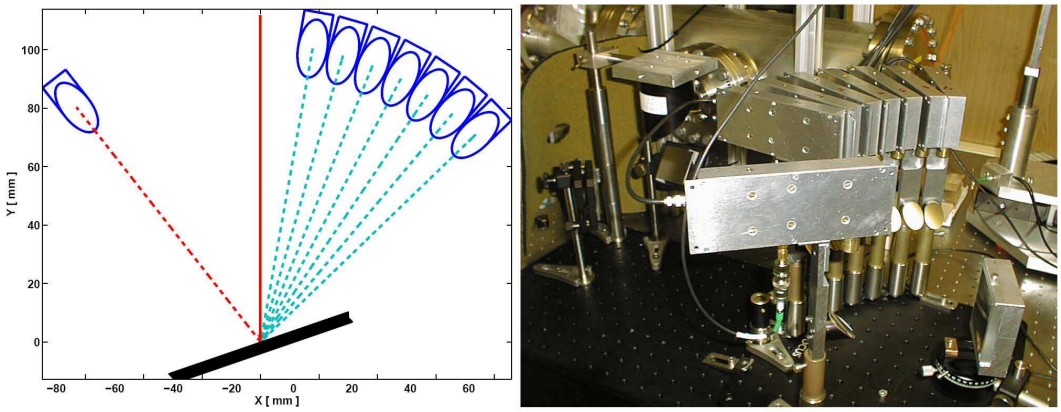

Figure 6.3: Eight-channel single-shot spectrometer; incident radiation in solid red, dispersed to the first order in cyan, reflected to the zero order dashed red.

a photography of the device in the right. Coherent radiation (solid red ray)

[3]This version of RMS is going to be installed as a diagnostic tool at the infrared undulator setup at FLASH [55].

illuminates the reflectance grating and the components of the dispersed radiation (dashed cyan rays) are directed to the corresponding detection units. One detection unit is also mounted to collect the reflected radiation into the zero-order (dashed red ray). The collecting optics is composed of eight 90° off-axis parabolic mirrors with one inch diameter. The axis of the parabolic curvature of the paraboloids are parallel to the radially dispersed rays centered at the illuminated part of the grating. The center of the circular curvature of the paraboloids are at their corresponding detector sensor. In other words, moving along the optical path, all the paraboloids are oriented "to focus". As the detector sensors, pyroelectric X003 (see section 7.2) are used.

6.2.2 Four-channel multi-stage single-shot spectrometer

The concept of staging of reflectance blazed gratings (see section 4.3.1) has been realized in the four-channel multi-stage mount as shown in the photograph of Fig. 6.4. This device detects intensities at wavelengths that are quite far from each other. The first three signals correspond approximately to wavelengths g_1, $\frac{5}{3}\mathsf{g}_1$ and $\frac{25}{9}\mathsf{g}_1$ where g_1 is the pitch size of the first grating and the next gratings obey the staging criterion. The last channel gives a signal proportional to the integrated intensity over wavelengths longer than $\approx \frac{25}{9}\mathsf{g}_1$. This device can be used to study the compression of the electron bunches, on a single shot basis and spectrally resolved, over a wide range. The resolved wavelengths in the eight-channel single-stage device are much closer to each other compared to those of this multi-stage device. This makes it possible to be sensitive to the structural changes that correspond to different parts of the broad-band spectrum. This is the conceptual idea behind an Advanced Bunch Compression Monitor (ABCM) [26]. The classical bunch compression monitor based on coherent radiation is composed of a detector, usually a pyroelectric, that detects the integrated diffraction radiation produced by a screen target on the path of the electron bunches[4]. The signal of such a detector is used to control the compression of the electron bunches and used in a feedback loop to stabilize the phase of accelerating modules to some desired degree of compression. Compared to the ordinary bunch compression monitors that work based on the integrated signals, with a multi-channel spectrometer such as ABCM, it is possible to extract informations that are directly related to the density of electrons in the spike. Sample measurement results using an ABCM is shown in Fig. 8.16.

[4]The detector of this device is normally placed in air and the interface to the ultra high vacuum is a thick crystalline-quartz window that cuts-off the spectra for wavelengths shorter

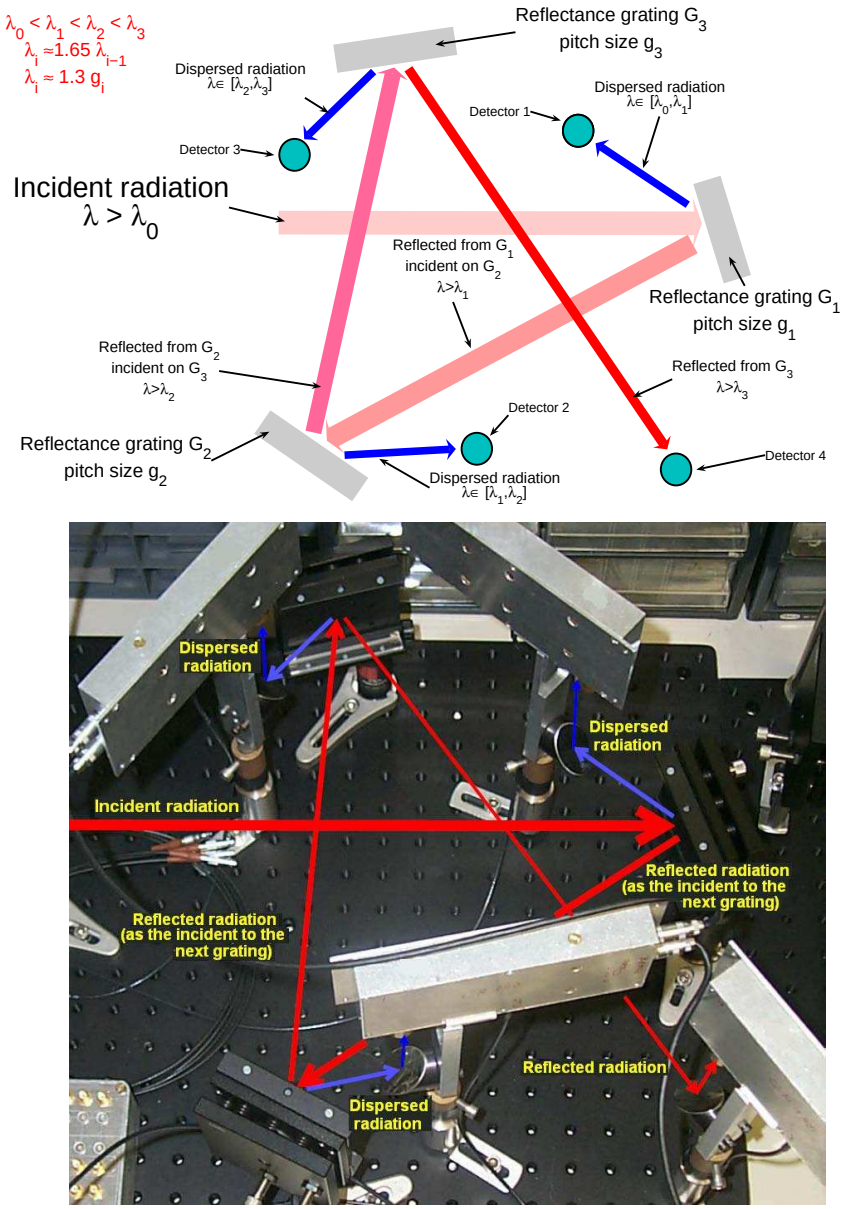

Figure 6.4: Four-channel multi-stage single-shot spectrometer. A polychromatic radiation of wavelengths longer than λ_0 incides upon the first grating with pitch size g_1. A 90° off-axis parabolic mirror oriented radially to the dispersed radiation with its axis, can be used to focus a selected part of the dispersed radiation onto a detector. The reflected zero-order radiation by grating G1, can be send to the next grating with appropriate pitch size to repeat a similar process. After several stages (three stages in this case) the reflected radiation can be focused on a detector (detector 4 in the picture) to get a signal that corresponds to the integrated intensity over relatively long wavelengths.

6.3 Accessories

In chapter 4, it was assumed that the radiation that illuminates the grating is composed of plane waves of the same polarization that propagate in the same direction. Transition radiation is radially polarized, therefore polarizers are needed to fulfill the requirements on the polarization. Polarizers are available that could be used over a wide range of the spectrum under study (see appendix C). The requirement on propagation direction is satisfied by transition radiation (see Fig. 3.3). The calculation results for efficiency and distribution of dispersed radiation in a grating setup can be used if all the components of the incoming radiation stay convergent and do not assume the beam waist before the detector sensors. The THz beamline CTR140 fulfills this requirement by providing an optical path length of $\approx 2\,\mathrm{m}$ inside the vacuum vessel at the end of the beamline before reaching the waist (3 m after M4 in Fig. 8.1).

6.3.1 Preparatory optics

As part of the in-coupling optics to the spectrometer setup it might be required to change the beam spot size that illuminates the grating, or it may become necessary to correct the propagation direction. This can be achieved by a combination of two focusing mirrors of appropriate focal length. In order to decrease the beam spot size, such a combination has been used for both the four-channel multi-stage and eight-channel one-stage single-shot spectrometers because the geometrical acceptance of the collecting mirrors were small.
The wavelength calibration relies on the precision under which the incident angle on the gratings and the adjusted orientation of the collecting optics are known. THz filters and materials that have known transmission for THz radiation are a good probe for wavelength calibration. Therefore a filter wheel that could house several such filters has been considered as part of the preparatory optics (see Fig. 6.13). In appendix B all the THz filters that are used for this purpose are listed and their transmission over THz range are shown.

Polarizers

The properties of reflectance blazed gratings strongly depend on the polarization of the radiation as discussed in detail in chapter 4. The extraction of the wavelength spectra is only possible if the properties of the grating are properly

than $\approx 80\,\mu\mathrm{m}$.

matched to the polarization. Wire grid polarizers are available over a very wide range in infrared spectral region. In appendix C the transmission of two polarizations for two different polarizers are shown.

6.3.2 Collecting optics

In order to minimizes effects like longitudinal and transverse spherical aberrations and defocus, it is necessary to minimize the blur spot[5]. There are analytical expressions, applicable only to ordinary lenses, which estimate the blur spot size for the given conditions. For these ordinary lenses, when the angular spread of the incident radiation is large, numerical calculations are indispensable. For the design of an optimal lens with appropriate principle curvatures (that fits to specific requirements), even in geometrical optics approximation, only numerical ray tracing can be used.
When polychromatic radiation illuminates a diffraction grating, depending on the dispersive power of the grating and chromaticity of the radiation, there will be a large angular extension of the dispersed light. From the argument above, and the fact that coherent radiation of electron bunches is broad-band, it is evident that the required lens for the collecting optics has to be designed using numerical ray tracing.

Remarks on 3D ray tracing

If $f(x, y, z) = 0$ represents the surface of the mirror under study and $\vec{\nu}$ is the vector in the direction of an incident ray on this surface at point $X_0 = (x_0, y_0, z_0)$ (see Fig. 6.5), the vector in the direction of reflected ray, $\vec{\nu'}$, is given by

$$\vec{\nu'} = \vec{\nu} - 2(\vec{\nu} \cdot \hat{n})\hat{n} \tag{6.1}$$

where $\hat{n} = \frac{\vec{\nabla} f}{|\vec{\nabla} f|}$. Given the propagation direction towards the mirror surface, these relations can be used to find the intersection of the reflected ray with the image plane. Applying this to the parallel rays (which start at points distributed over a reasonable spot size) incident upon the mirror, one can get the projection of the beam spot reflected by the mirror to an image plane or surface. This procedure can be used for all propagation directions over a distribution which is given, for instance, by the dispersed components in a grating setup. In the following this method is applied to the special case of a paraboloid[6] of Effective

[5]Blur spot is the diameter of the best focused spot containing all of the geometrically traced rays in the image.

[6]A parabola which is rotated about its axis makes the paraboloid.

Focal Length (EFL) of αP where P is the parent focal length and α is a measure of the part of the parabolic surface which forms the mirror[7]. For the αP parabolic mirror of Fig. 6.5 the surface is given by

$$x^2 + (y - \alpha P)^2 - 4P(z + P) = 0 \qquad with \quad -r < x < r \quad -r < y < r$$

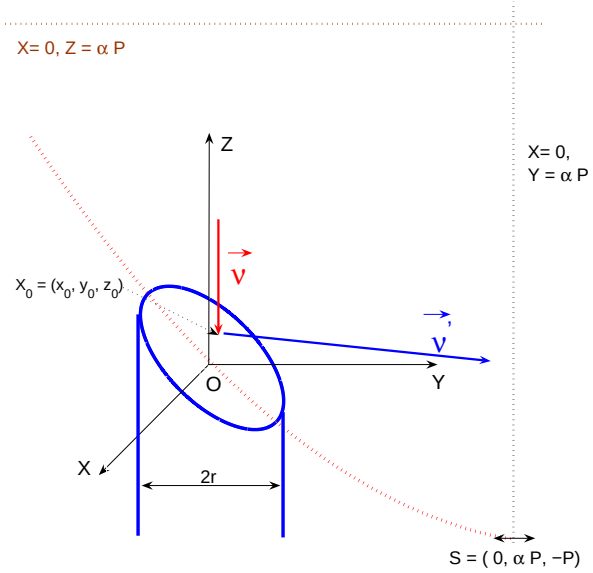

Figure 6.5: A parabolic mirror and the coordinate system that is used for the calculation of the reflected rays. An αP parabolic mirror is a cylindrical cut from a paraboloid with center of the circle at coordinates $(0, \alpha P, P)$ measured from the vertex of the parabola, S. The dashed-line parallel to the z-axis at S is the axis of the parabola. The vector in the direction of incident ray on the surface of the parabolic mirror is $\vec{\nu}$ and that of reflected ray is $\vec{\nu'}$. $X_0 = (x_0, y_0, z_0)$ is the intersection point on the surface with the incident ray.

where r is the radius of the part of the paraboloid that makes the mirror. Substitution into 6.1 results in

$$\vec{\nu'} = \vec{\nu} + (x_0, y_0 - \alpha P, -2P) \cdot Q \qquad with \;\; Q = -\frac{x_0\nu_x + (y_0 - \alpha P)\nu_y - 2P\nu_z}{2P(z_0 + 2P)}$$

[7]A 90° off-axis parabolic mirror is given by $\alpha = 2$. In general, for a θ° off-axis parabolic mirror in terms of α parameter, $\theta = 90 + \arctan\frac{\alpha^2 - 4}{4\alpha}$.

Consider the trivial case of the rays incident on a 90° off-axis parabolic mirror ($\alpha = 2$) parallel to its axis. In terms of the notation of this section this means $\vec{\nu} = (0, 0, -1)$ and it is easy to see $\vec{\nu'} = (x_0 Q, (y_0 - 2P)Q, -1 - 2PQ)$ with $Q = \frac{-1}{z_0 + 2P}$. The parametric equation for the reflected ray is $\vec{X}(s) = \vec{X_0} + \vec{\nu'} s$ where s is the line parameter. It can be seen that $\vec{X}(y = 2P) = (0, 2P, 0)$ independent of X_0. This shows that, for this trivial case, all rays get focused to the focal point as it is expected.

In Fig. 6.6 the result of a simulation for rays that over a large angular spread incide upon a paraboloid is shown. In the left plot, the angle to the z-axis is changed between $-11°$ to $11°$ and $\vec{\nu}$ has an x-component equal to zero. The black points show the intersection of the incident rays with the paraboloid seen from a view perpendicular to the xz-plane. Each of the red points are the intersection of the individual rays, reflected by the mirror, with the observation plane $\mathtt{y} = \mathtt{2P}$. The projected spot size increases for increasing angle of incident. A sharp focus can be found in the center but only when rays are parallel to the axis of the parabola. On the right, an error of 5% of the maximum y-component is introduced as the x-component, which makes the situation worse such that even the central angle with no y-component does not form a point-like focus. In both cases the spot size in the observation plane ($\mathtt{y} = \mathtt{2P}$) increases as a function of the incident angle. In Fig. 6.7 a view from a direction perpendicular to the yz-plane is shown. The dispersive element resembles a source that generates wavelength-dependent propagation direction. For each angle to the z-axis one color is used; red is used for the largest angle (longest wavelength) and violet is used for the smallest angle (shortest wavelength). For a transmission grating as the dispersive element, there are identical diffraction orders in both sides of the central zero-order (see section 4.4). In Fig. 6.7 a transmission grating is considered as the dispersive element. Therefore rays with the same absolute angle to the z-axis are shown with the same color[8]. For those rays that have negative angles to the z-axis, blur spot happens in distances larger than the nominal focal length. The red rays correspond to the largest blur spot; the violet rays have made the minimum blur spot. For those rays that have positive angles to the z-axis, blur spot can be seen at distances smaller than the nominal focal length. For this set of rays the blur spot is very large and in order to avoid a fuzzy plot, only two angles to the z-axis are shown. The blur spot locus is on a curved surface, which can be approximated by an inclined plane. The simulation result for an optimal inclined plane seen from a view perpendicular to xz-plane is shown in Fig. 6.8. The transverse coma has not improved and the minimum spot size is still huge for large angles. The

[8]Nevertheless the optical properties that can be concluded are quite general and for a more general case only the color code has to be changed.

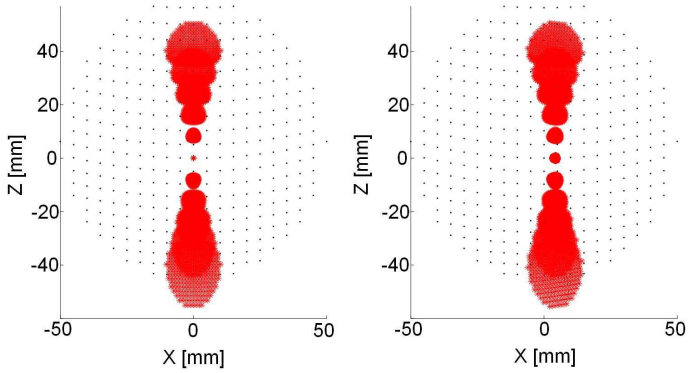

Figure 6.6: Ray tracing simulation result for rays in the direction off-parallel to the paraboloid axis incident on the paraboloid (for details see text).

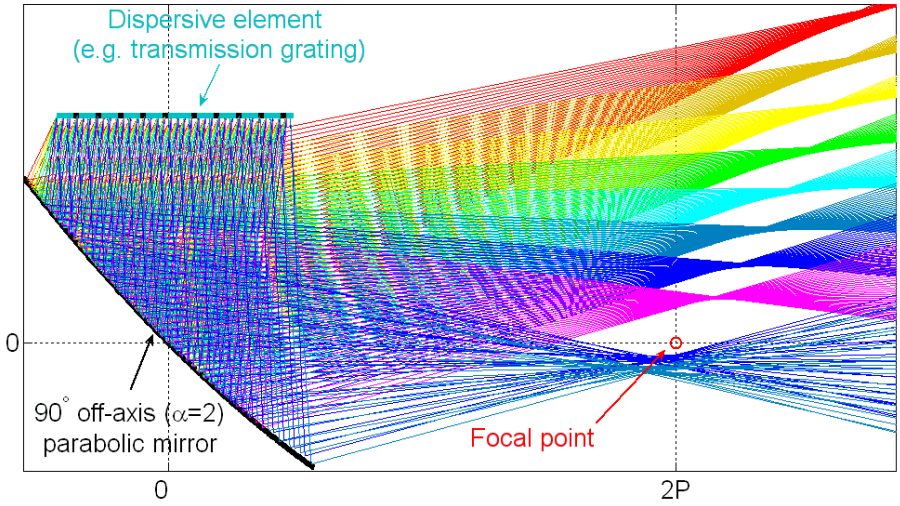

Figure 6.7: View of rays moving in the yz-plane. Rays start at the source (which is considered a dispersive element) with different angles to the z-axis. For each angle to the z-axis, a set of rays with the same color are considered that start at different points of the source. Red rays correspond to the largest angle (longest wavelength) and violet rays correspond to the smallest angle (shortest wavelength). For more details see text.

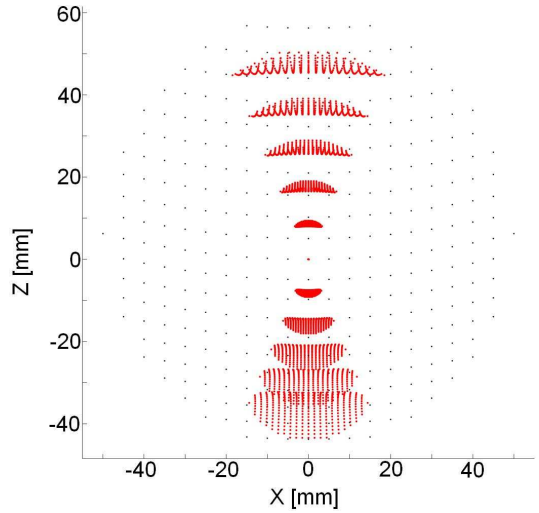

Figure 6.8: Same as the left picture of Fig. 6.6 but for an optimized inclined plane of detection (see text for further explanation).

key consequence is that only for incident rays with angles very close to parallel to the paraboloid axis, the point-like focus can be achieved. This leads to the design of an appropriate mirror for the collecting optics of the grating spectrometer.

Ring-mirror

Consider a surface that has a parabolic principle curvature rotated about an axis normal to the axis of the parabola which is in the distance equal to αP from the central height of the αP parabola (The axis normal to the paraboloid axis in Fig. 6.5). This produces an optimum surface, a "ring-mirror", to focus rays that emerge from the source in radial directions. All components of the dispersed light that propagate in the radial directions, when incide upon the ring-mirror see an optimal "to focus" mirror. An ordinary paraboloid does not have this property. The most important difference between a paraboloid and a ring-mirror is that all rays that propagate parallel to the axis of a paraboloid get focused to a point-like focus, and with non-zero angles to the axis of the paraboloid, angle dependent strong aberrations are take place. A ring-mirror is the improved extension of the multi-mirror collecting optics of the eight-channel single-shot spectrometer[9]. The multi-mirror collecting optics has parabolic mirrors which

[9]Ring-mirror is not an exact extension of the collecting optics scheme of the eight-channel spectrometer. For ring-mirror the circular curvature is centered at the center of the source (see Fig. 6.10), in multi-paraboloid scheme the circular curvature of individual mirrors are centered at the corresponding detector sensor.

are oriented along their axes parallel to the different components of dispersed rays. The acceptance of each unit is limited to the size of the single mirror of the unit. With ring-mirror the entire dispersed radiation is collected and focused on the detectors. Figures 6.9 and 6.10 show schematics of the ring-mirror. The

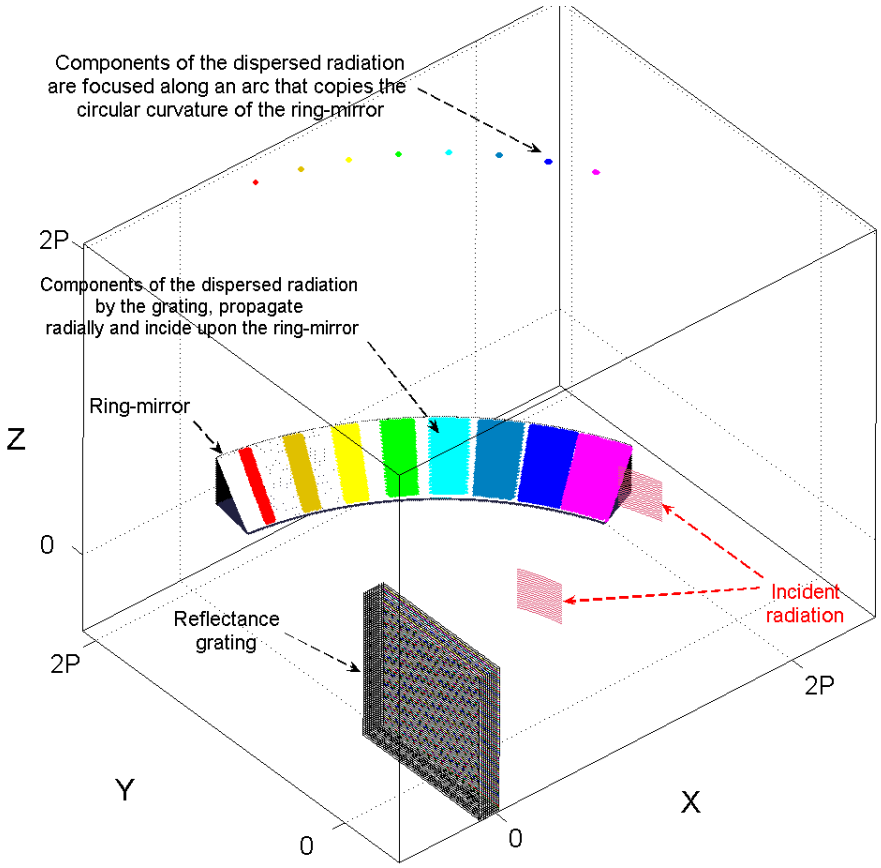

Figure 6.9: Perspective view to a stage of the spectrometer. The wave-front of the incident plane wave is shown in two spatial points along the direction of propagation. The incident radiation is dispersed into its components after it hits the reflectance grating. These dispersed radiation components propagate radially until they hit the ring-mirror. Ring-mirror focuses these components to distinct point-like spots along an arc which has a radius equal to the circular curvature of the ring-mirror and is located in Z=2P plane.

blur spot of all the components, incident upon the ring-mirror over very large extensions of the angular spread (larger than 50°), is close to the detector sensor size. The simulated properties of this mirror have been checked experimentally using a large-spot laser pointer. Illuminating a grating of appropriate pitch size with such a laser light, many spots of high enough intensity can be produced (see Fig. 4.2). When the illuminated part of the grating is located at the center of the ring-mirror (see Fig. 6.10) such that the dispersed radiation lies in the plane of the circular curvature of the ring-mirror, all the different spots that represent the dispersed wavelength components, get focused to a spot size smaller than the detector sensor size (see Fig. 6.11). These spots are located on the plane parallel to the optical plane and αP apart from the mirror on a circular path. For $\alpha = 2$ the radius of the foci is equal to the radius of the ring-mirror.

In the ring-mirror mount of Fig. 6.12 it is possible to adjust the distance which

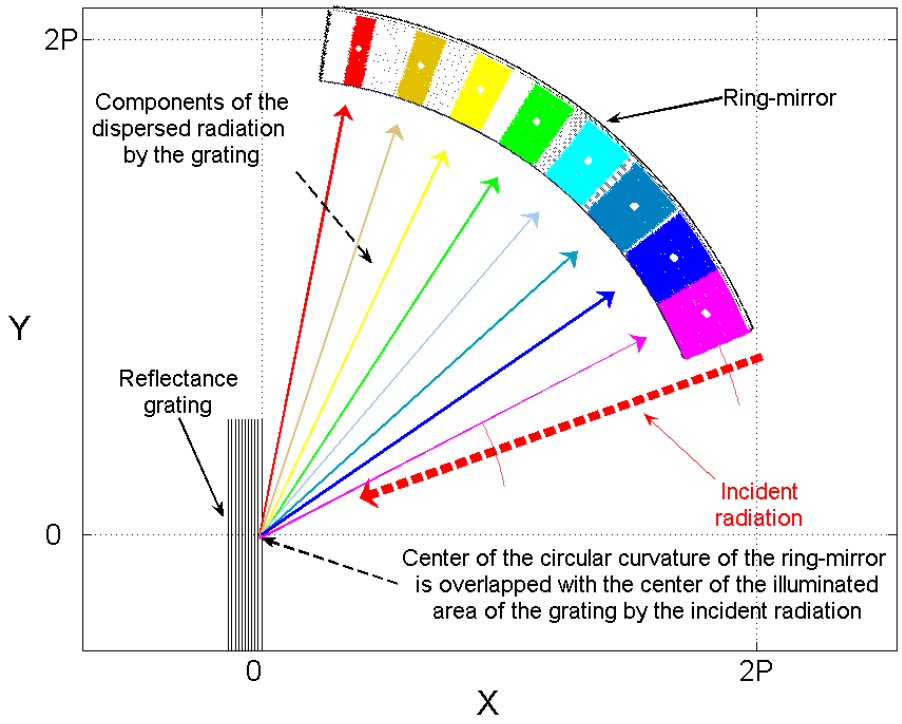

Figure 6.10: Top view to a collecting optics based on the ring-mirror. Red dashed arrow shows the polychromatic radiation incident on the grating, other arrows show the components that are dispersed by the grating and illuminate the ring-mirror thereby focused to spots (in white color) at the center which in fact are located in Z=2P plane.

resembles the focal length. The drawing shown in Fig. 6.12 is the unit used in the single shot spectrometers of the next section.

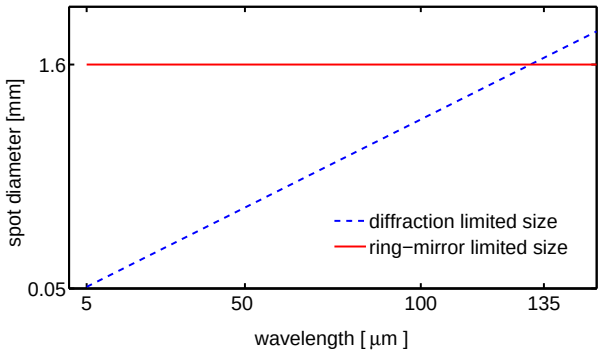

Figure 6.11: Diffraction limited focus and ring-mirror limited focus. The diameter of the central Airy disk is calculated as the diffraction limited focus with the incident beam spot size of 25 mm and focal length of 250 mm. The ring-mirror limited focus is plotted in terms of the focused spot size that can be achieved when rays are traced originated from the entire incident beam size of 25 mm. In other words, the ring-mirror is not a perfect lens for wavelengths shorter than $\approx 130\ \mu\mathrm{m}$ but focuses the entire dispersed radiation to a size smaller than the detector sensor size. For longer wavelengths the focus is diffraction limited and the ring-mirror acts as a perfect lens.

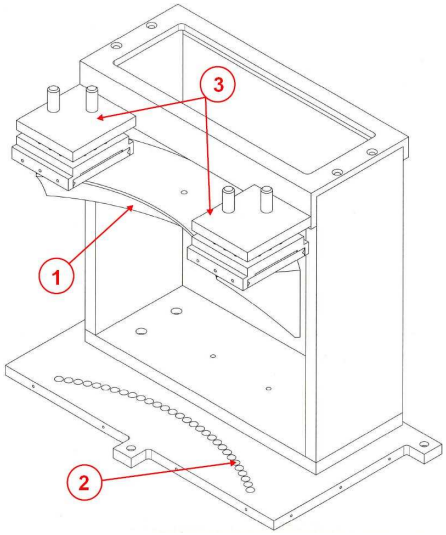

Figure 6.12: Collecting optics unit as it is used in one stage of the single-shot spectrometer.
1- Ring-mirror
2- Collecting cones
3- Standard flat mirror holders

6.4 Spectrometers based on integrated collecting optics and detectors

In this section the final versions of the single shot spectrometer are described. The development of an integrated 30-channel pyroelectric detector unit made it possible to realize the single shot spectrometer [57].
In the first series of experiments only one stage, based on the unit which is shown in Fig. 6.12, was used. The 30-channel electronic circuit with pyroelectric detectors was located under the exit part of the cones that can be seen in Fig. 6.12 along the arc at the focus of the ring-mirror.
The pyroelectric sensors $X009$ (see section 7.2) were used for the one-stage setup. In the two-stage setup, the stage for the shorter wavelengths was equipped with a reflectance grating and the sensor type $X003$ (see section 7.2). For the stage with transmission gratings, the sensor type $X009$ was used. In one-stage mount, both options, the transmission and reflectance blazed gratings, were used with and without filter heads. A polarizer of the type `G30`, which is described in appendix C, was used when the two stage device was mounted.

Figure 6.13 shows the two-stage single-shot spectrometer. The incident radiation (red line) enters the spectrometer setup from the THz beamline (CTR140) on the left. The remote controlled filter wheel has six filter holders which can be used to introduce different band-pass or low-pass filters as described in appendix B. These THz filters provide a tool for wavelength calibration of the spectrometer. The next element in the optical path is the polarizer G30 (see appendix C). After the polarizer there is an out-coupling mirror that can be moved into the light path to focus it onto an infrared pyro-camera. This device can be used to record, in single shot, the transverse profile of the radiation (see Fig. 8.5). When the parabolic mirror is out, the beam illuminates one of the reflectance blazed gratings which are housed on a vertical mover. The dispersed radiation (blue lines) propagate towards the detection unit, which is shown in Fig. 6.12, equipped with detector sensors X003 (see section 7.2). The zero-order radiation of the reflectance blazed grating incides upon the next grating which is one of the transmission gratings that are housed on a vertically movable linear stage. Both the zero-order and first-order dispersed radiations of the transmission grating propagate towards the second detector unit (again of the same type as Fig. 6.12) which was equipped with detector sensors X009 (see section 7.2).

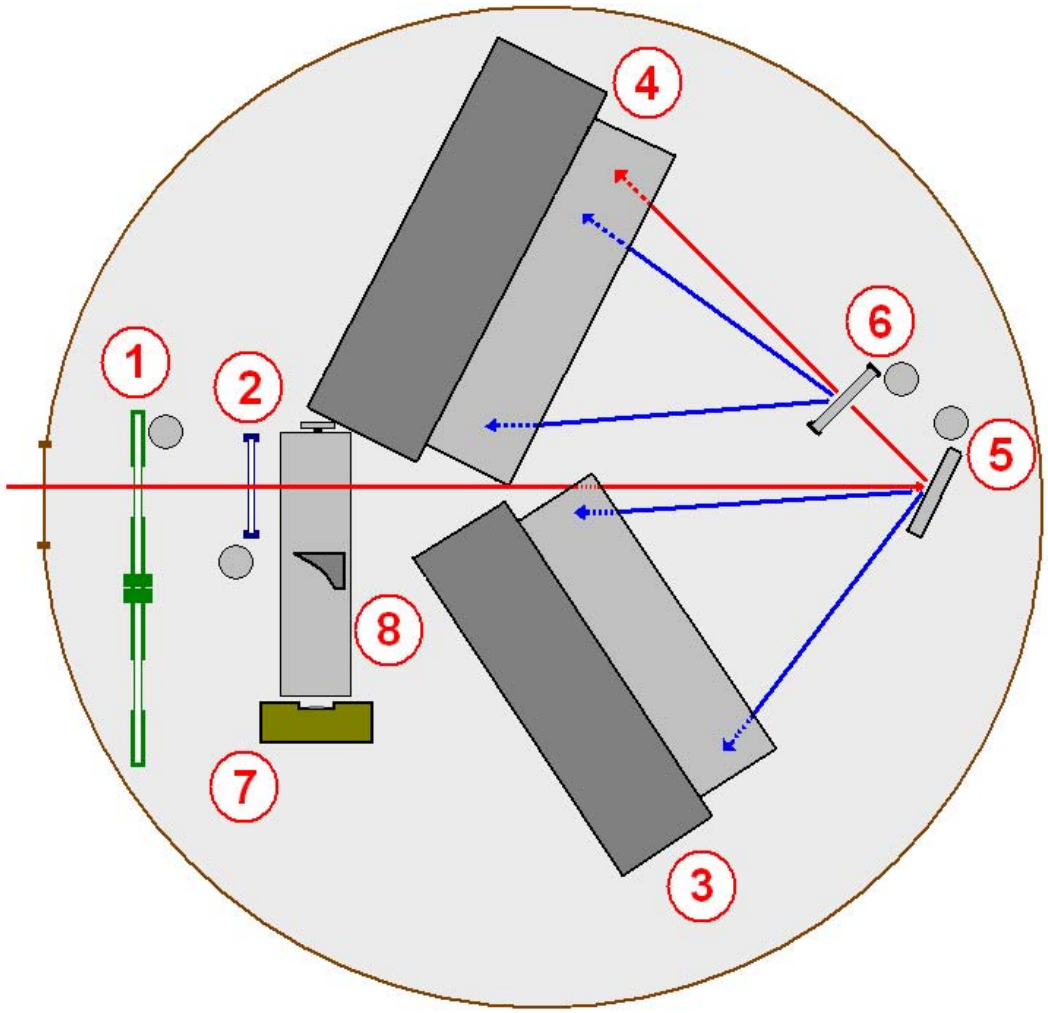

Figure 6.13: Two stage single shot spectrometer.
1- THz-filters (remote controlled)
2- Polarizer (remote controlled)
3- Reflectance grating stage (for the short wavelength range)
4- Transmission grating stage (for the longer wavelength range)
5- Reflectance gratings holder and remote controlled mover
6- Transmission gratings holder and remote controlled mover
7- Pyro-camera
8- Parabolic mirror and its linear mover

Chapter 7

Experimental Setups and Measurements at FELIX

In order to perform experiments on calibration of the pyroelectric detectors and the characterization of the reflectance gratings, several setups have been mounted at FELIX [58], where infrared FEL radiation in the wavelength range 5 to 220 μm was provided for these experiments.

7.1 FEL radiation at FELIX

In the right hand side of Fig. 7.1 the time structure of the FEL radiation pulses at FELIX is shown. The width of a micropulse is in the range of a few picoseconds

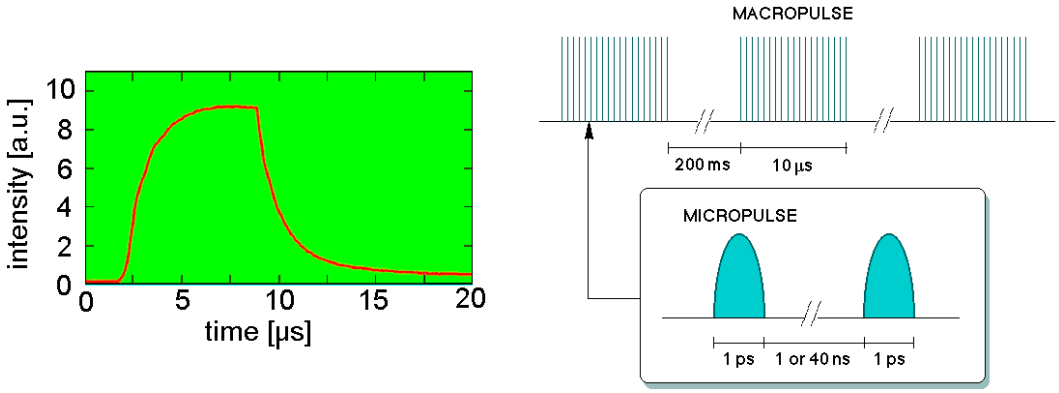

Figure 7.1: Right: Radiation pulse time structure at FELIX. Left: The macropulse intensity development for 80 μm wavelength (Courtesy FELIX [58]).

and the spacing of the micropulses are either 1 ns (1 GHz mode) or 40 ns (25 MHz mode). The micropulses form a train (the macropulse) with a duration of up to $15\ \mu s$. The macropulses are repeated every few 100 ms, with a maximum repetition rate of 10 Hz. In the left side of Fig. 7.1 the macropulse intensity development for $80\ \mu m$ wavelength is shown (the micropulses cannot be seen in this figure, due to the bandwidth of the detector used). The first few μs of the macropulse are needed for the radiation intensity to build up from noise toward saturation. This typically takes $3 - 4\ \mu s$. A saturated output is available during the subsequent part of the macropulse ($5\ \mu s$). The electron pulse ends at $9\ \mu s$ in this example and the laser power drops to zero. Variation of the macropulse duration and/or its repetition frequency can be done by adjustment of timing devices. The energy per macropulse is in the level of few tens of mJ (see Fig. 7.4) which is several orders of magnitude higher than the level at which thin crystal pyroelectric detectors would saturate. Therefore, sufficient attenuation had to be used when radiation was focused on the pyroelectric detectors.

7.2 Pyroelectric detectors calibration

Figure 7.2 shows the experimental setup. The entire setup was under vacuum in the level of $\leq 10^{-3}$ mbar. In table 7.1 the specifications of the pyroelectric detectors are listed. The joule-meter is a pyroelectric detector with thick crystal that makes the absorption almost independent of the wavelength (type J50LP, low profile joule-meter; MOLECTRON). A focusing mirror is mounted on a remotely movable stage where it can reach the optimum focus for the individual detectors and the joule-meter. A pyroelectric camera (SPIRICON Pyrocam III) was also mounted in the setup to be calibrated in the same way. The pyroelectric detectors are all followed by the same type of amplifiers [1] and their sensors are given in table 7.1. None of the detectors in the setup of Fig. 7.2 is faster than 250 kHz, they sample the macropulse over first $4\ \mu s$ after the trigger signal, while the joule-meter samples the entire macropulse. The measurement procedure was as follows. The FEL radiation was focused on one of the detectors or joule-meter by adjusting the remotely controlled focusing mirror. In each case the attenuation level was set such that the signal was not saturating within the scan range. A LabVIEW program and GPIB readout was sampling the spectrum of the signals on an oscilloscope and recording the data on the local disk. During the scan and for each wavelength, eight shots were sampled and the average over these eight

[1] CR-110 is a charge sensitive amplifier and CR-200 is a Gaussian shaper. Specification of these two amplifiers are given at [59].

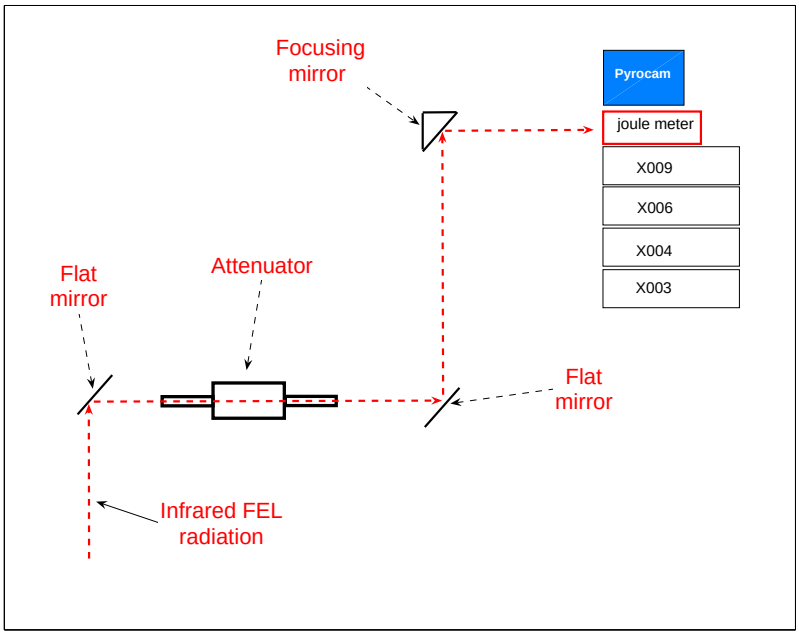

Figure 7.2: Experimental setup for the detector calibration at FELIX.

Table 7.1: Specifications of the pyroelectric detectors

Detector	Pyro-crystal type,thickness (μm)	Black coated	Amplifier integrator, shaper
LIE-301-X003	$LiTaO_3$, 25	$\surd$	CR-110, CR-200
LIE-301-X004	$LiTaO_3$, 25	–	CR-110, CR-200
LIE-301-X006	$LiTaO_3$, 75	$\surd$	CR-110, CR-200
LIE-301-X009	$LiTaO_3$, 25	$\surd$	CR-110, CR-200

signals used to calculate the response. Taking into account the attenuations that were used in the corresponding scan, the measured spectrum for each detector has been normalized to the corresponding joule-meter spectrum, resulting in a response function that differs only by a constant factor with respect to the absolute calibration. This factor can be determined in one (or even better, in a few wavelengths) wavelength by reading the energy on the calibrated joule-meter[2]. In Fig. 7.3 the results for four pyroelectric detectors are shown. Infrared-FEL radiation was provided in three runs in the wavelength range of 35 to 65 μm, 65 to 85 μm and 85 to 135 μm, respectively. The results of these runs in the region where they overlap are in good agreement.

In Fig. 7.5 the results of the calibration measurement in the short wavelengths

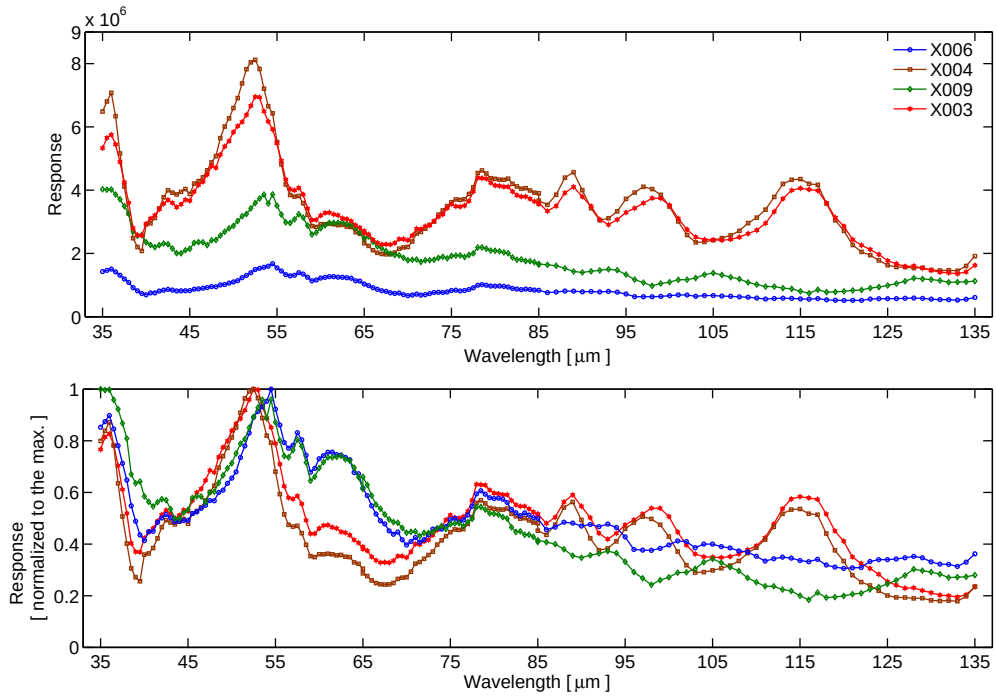

Figure 7.3: Top: Comparison of the response of different detectors to the same FEL radiation intensity. Bottom: The plots in the top picture are normalized to the maximum response for each detector. At wavelengths $\approx 87, 97$ and 115 μm there are resonance responses for detectors X003 and X004. The difference of these standard sensors with the other two specially designed sensors is in the design of their multi-layer slabs (see Fig. 5.1) and is discussed in [48, 49].

[2]The basis of this is on the presumed flat response of the thick black-coated pyroelectric detector of the joule-meter.

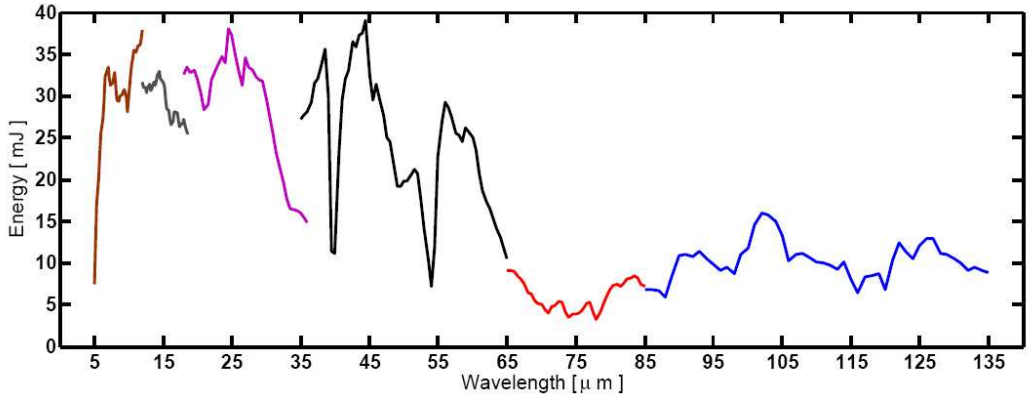

Figure 7.4: The absolute macro-pulse energy of the FEL radiation at FELIX measured with a MOLECTRON joule-meter (type J50LP, low profile joule-meter) which has a thick pyroelectric detector as the sensor and accordingly no etalon resonances were expected.

range, which are covered by three different settings of FELIX, are shown. In these plots the normalization is made to the detector X003. The reason for this is that the joule-meter scan has been found to be not useful for normalization due to an unknown wavelength dependent attenuation[3]. Unfortunately in this range below 35 μm, which is very critical for the bunch profile determination, detectors are not calibrated. The relative behavior can be understood from Fig. 7.5. The clear finding is that the X009 detector is not appropriate for short wavelengths. This result is in agreement with the fact that at FLASH, measuring short wavelengths CTR of kicked bunches with the detector X009 shows signals that are much weaker than those measured with X003. For this reason the detector X003 has been installed on the first stage of the two-stage single-shot spectrometer.
Theoretical computation of the relative response, taking into consideration the resonance absorption of infrared radiation in a pyroelectric crystal has been described in [47]. In Fig. 7.6 a comparison between the theoretical calculation (carried out by B. Schmidt [48, 49]) and measurement is shown. The vertical line at $\approx$ 44 μm is the transition point of the two spectra measured by the two stages of the spectrometer shown in Fig. 6.13. The conclusion is that the theoretical description is in qualitative agreement, in terms of the wavelengths of spikes in the spectrum, with the measurement over the range where experimental data exist. Therefore, for the short wavelengths where there are no reliable measurements

[3]In fact, for the short wavelengths an attenuator appropriate for the wavelengths in the range of 5 to 35 μm has been installed but unfortunately the device was not installed properly (missing long damping tubes in Fig. 7.2) resulting in non-damped diffracted waves that were going toward the setup and making the read-out useless.

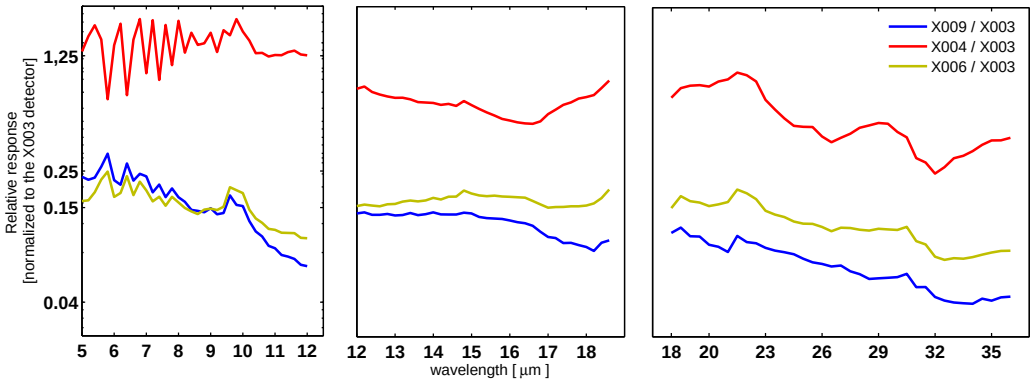

Figure 7.5: The response function of detectors X004, X006 and X009 normalized to the X003 response.

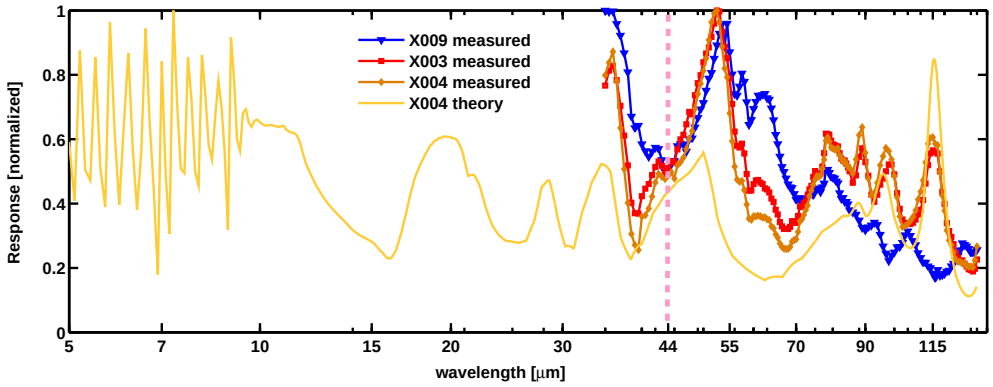

Figure 7.6: Comparison between theoretical calculation for the detector response and measurements. The theoretical computation which is carried out by B. Schmidt [48, 49] cannot take into account the role of the black coating due to the non-available optical properties of the material [47].

the theoretical calculations is used to deduce the detector response. In Fig. 7.7 the absolute response of the detector assembly of the two stage spectrometer is shown.

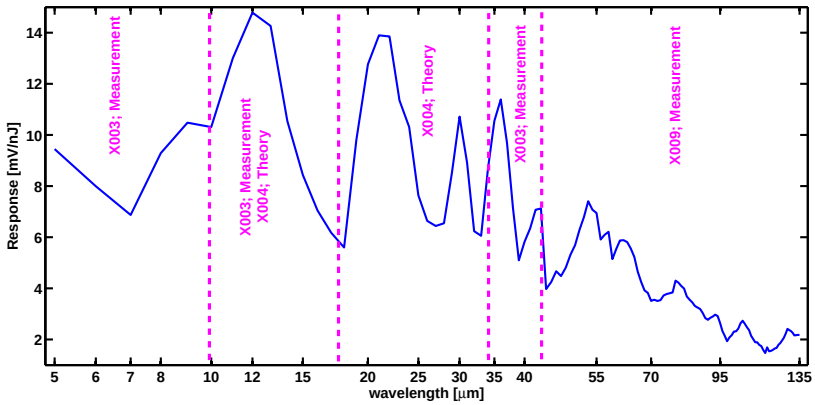

Figure 7.7: Absolute response of the detector assembly of the two-stage spectrometer.

The same method as it was described for the pyroelectric detectors calibration was used for a SPIRICON pyroelectric camera calibration. The lower overall responsivity of this camera required much less attenuation from the unit inside the setup. Therefore the data collected over short wavelengths should suffer less from the uncertainties on the wavelength dependent attenuation in comparison to the pyroelectric detectors data. In Fig. 7.8 the measured response function is shown. Response is given in terms of counts which are read over an ellipse that surrounded the area of the illuminated pixels, therefore this response function assumes a linear behavior of the pixels as a function of deposited energy.

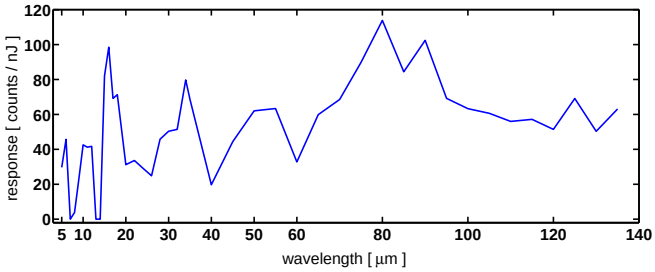

Figure 7.8: Response of the SPIRICON Pyrocam III to the infrared short pulses. The vertical axis is in terms of counts which can be read by using the LBA-PC software that was provided by the company.

7.3 Experimental results on reflectance grating characterization

In order to check the predictions for efficiencies and distribution of dispersed radiation in a grating spectrometer set-up, the experiments described in this section have been performed. The experimental setup is sketched in Fig. 7.9.

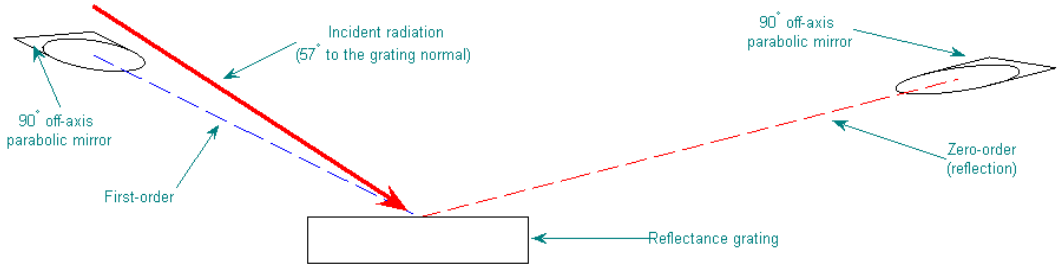

Figure 7.9: Experimental set-up for grating efficiency measurement at FELIX.

The angle of incidence on the gratings has been chosen to be $57°$ (angle to the grating normal, see Fig. 4.4). The simulation showed that this angle gives the widest and most efficient dispersion in a non-Littrow mount. The reflectance grating was selected from one of the gratings with a pitch size of $g_1 = 127\ \mu m$ or $g_2 = 50\ \mu m$ dependent on the experiment. Two identical $90°$ off-axis parabolic mirrors (2 inches diameter) were used as the collecting optics, one in the zero-order (reflection for the mirror) and one in the first order. In Fig. 7.10 the combined result of six independent measurements are shown. Several measurements were conducted in air and several in vacuum. In each experiment first a gold plated mirror has been installed instead of the reflectance grating to send the attenuated FEL radiation to the same path as it would go if the gratings were installed. Then the intensity as a function of FEL wavelength was measured. In the next step, by putting in either a grating with a pitch size of $g_1 = 127\ \mu m$ or $g_2 = 50\ \mu m$, the intensity of the reflected light, which is the diffracted zero-order, was recorded. The ratio of the two recorded spectra, one with a grating and one with the mirror, gives the zero-order efficiency of the grating. In general, the efficiency of the grooves is larger than zero-order efficiency of the grating[4]. Six measurements were performed independently with different gratings and various FEL wavelengths such that for several ranges of the normalized wavelength (see Fig. 7.10), the efficiency values were measured more than once (by different gratings, G1 with $g_1 = 127\ \mu m$ and G2 with $g_2 = 50\ \mu m$, and/or different absolute wavelengths).

[4]For far-infrared this difference is negligible because of high reflection coefficient.

They are in agreement with the solid red curve which is the theoretical prediction. In order to check the prediction for the angular distribution of first-order dispersed light, for several wavelengths of the FEL, the arm that was housing the detection system (pyroelectric detector), was moved over the entire possible angular range. At angles close to the value that is given by Eq. 4.3 there were signals, for which the peak signal corresponded to the actual FEL wavelength. The integral of the intensity over the range of first-order dispersed light turned out to be more than three times stronger than the reflected intensity to the zero-order.

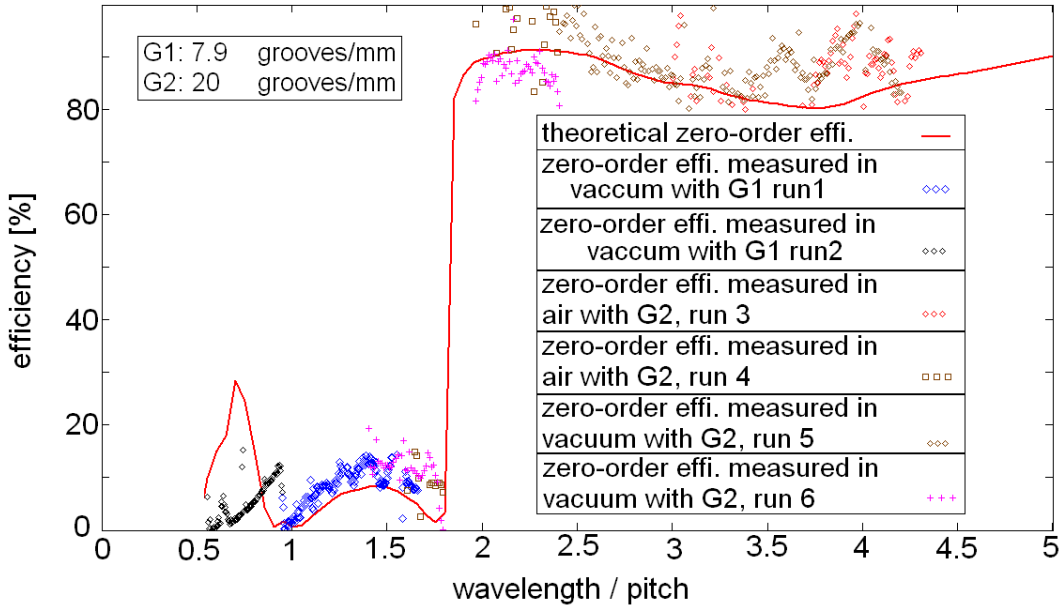

Figure 7.10: Experimental verification of efficiency calculation for a reflectance grating mount. Theoretical calculation is in agreement with the measurements. In particular, the expected sharp change at about $\frac{\lambda}{g} \approx 1.7$ can be seen in two measurements (runs 4 and 6) which cover a range of normalized wavelength that includes $\frac{\lambda}{g} \approx 1.7$.

Chapter 8

Experimental Setups and Measurements at FLASH

8.1 THz coherent transition radiation source at FLASH

In order to facilitate longitudinal bunch diagnostics based on coherent transition radiation (CTR), a THz beam-line, shown in Fig. 8.1 has been designed [40]. It guides the CTR from the accelerator tunnel over a distance of 18 m to an experimental hut. An ultrahigh vacuum chamber, housing several transition and diffraction radiation screens (the left sketch in Fig. 8.1), is located between the last acceleration module and the collimator section upstream the undulator. The radiation is coupled out from the UHV chamber of the linac through a 0.5 mm thick diamond window (see Fig. D.1) and is transported by an optical system consisting of four focusing and four plane mirrors to the experiment (the right hand sketch in Fig. 8.1). The THz beam is transported in a tube of 190 mm inner diameter which is evacuated (air pressure < 0.1 mbar) to avoid absorption in humid air (for water absorption lines see Fig. D.2). The computed THz transmission using "THz-Transport" as the simulation toolbox (see next part), is plotted in Fig. 8.2 as a function of wavelength. The acceptance of the THz beam-line is small for wavelengths longer than $800\ \mu$m due to diffraction effects, and rises steeply with decreasing wavelength to a plateau, which is practically constant for wavelengths shorter than $300\ \mu$m. Around 3-5μm the diamond window has an absorption band (see Fig. D.1).

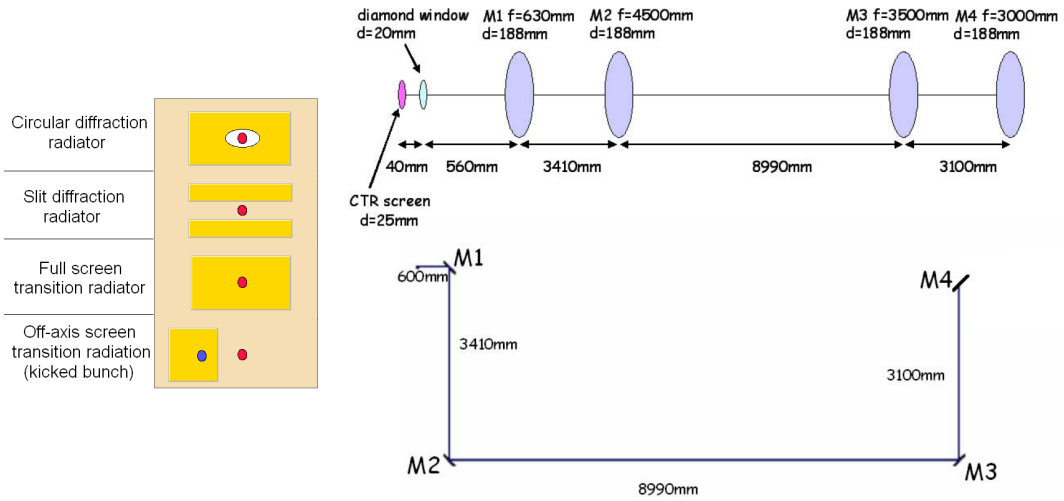

Figure 8.1: Left: Transition and diffraction radiation screens of CTR140 beamline. The red spots show the nominal electron orbit with respect to the inserted screen. The blue spot on the off-axis screen shows where a kicked bunch hits the screen. Right: THz Beamline (CTR140) lattice. It is a reflective optics lattice that transports the THz transition or diffraction radiation of the electron bunches efficiently to the experimental hut.

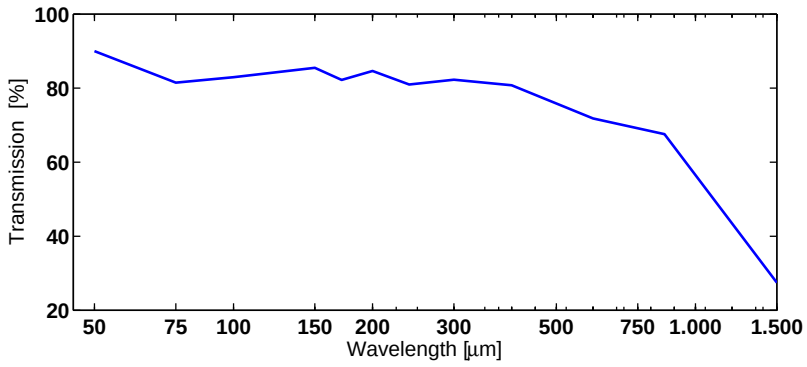

Figure 8.2: Computed geometrical transmission of the THz beamline using "THz-Transport".

"THz-Transport" as simulation tool-box

"THz-Transport"[1] generates the transition radiation from a single electron for a specified radiator-screen geometry and frequency. It can propagate all kinds of radiations, including transition radiation, to optical elements using Fourier transformation optics. Optical elements which can be described include parabolic, elliptical, toroidal, spherical and flat mirrors and windows of different materials. The code provides the complex electric field amplitude at any plane perpendicular to the optical axis and allows simulating complex optical beam-lines with respect to transmission functions or propagation of THz pulses. It is written as a set of Mathematica routines and is able to handle frequencies in the range of a few GHz up to about 10 THz.

8.1.1 Simulation results using "THz-Transport" and comparison with the experiments

An example of the application of "THz-Transport" is the design of the THz beam-line at FLASH. In the following, a simulation is presented to demonstrate the current understanding of the generation and transport of CTR. For a single electron that hits on a screen and generates transition radiation, the simulation result for the transverse profile is shown in Fig. 8.3. The view point is 1.5 m after M4 in Fig. 8.1 and the calculation is done for the horizontal polarization at a wavelength of 50 μm. The coherent transition radiation of electron bunches is broad-band and using THz band-pass filters a band-width can be selected. In order to get only one polarization the polarizer G30 of appendix C may be used. A band-width centered at 50 μm of the horizontally polarized radiation is used to measure the transverse profile, Fig. 8.4. The simulated and measured profiles should show the same pattern. The product of the values of the form factor (see Eq. 3.3), transmission of the beam-line plus the THz filter and polarizer, and the detector response at 50 μm gives the scaling factor for the two profiles. The computed profile shown in Fig. 8.3 and the measured profile of Fig. 8.4 show a qualitative agreement. The measured profile has not been done single shot and possible machine changes are imprinted there. For a filtered CTR at a wavelength of $\approx$ 80 μm a single shot measurement result is shown in the right side of Fig. 8.5 which is made using SPIRICON PyroCamIII (see section 7.2) located at the focus of a paraboloid at the end of CTR140 beam-line (see Fig. 6.13). The computed transverse profile shown on the left of Fig. 8.5 is in qualitative agreement with

[1] "THz-Transport" is a program package in Mathematica written by B. Schmidt [60].

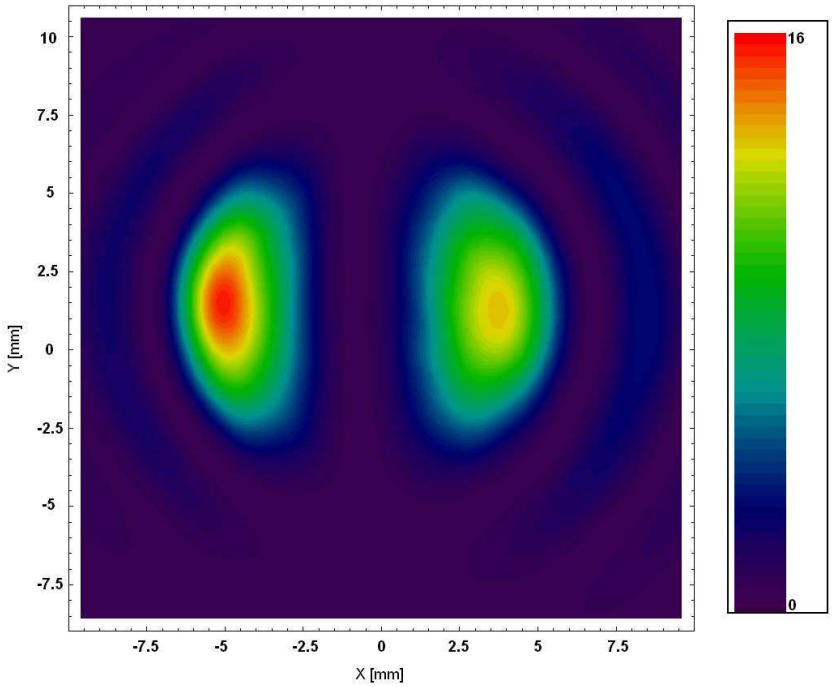

Figure 8.3: Simulated transverse profile of the 50 μm wavelength component of CTR.

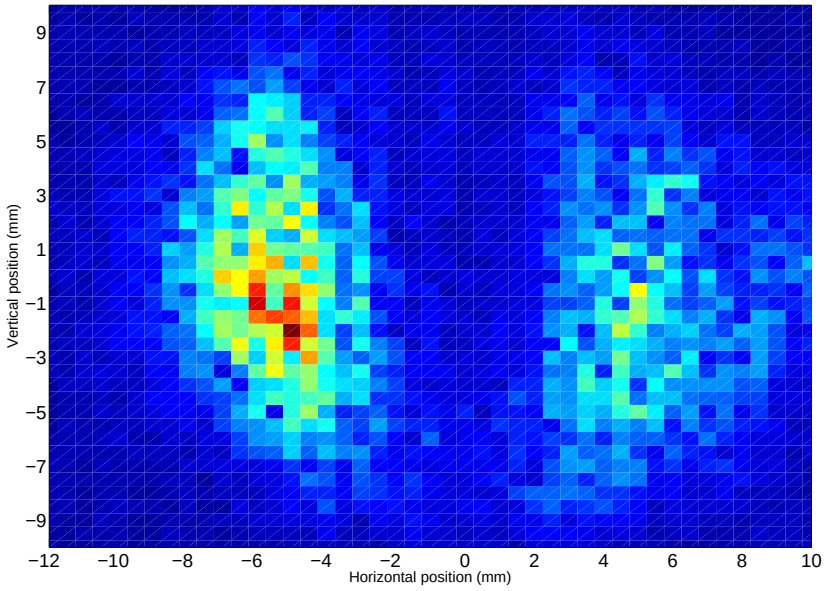

Figure 8.4: Measured transverse beam profile of CTR 50 μm wavelength component.

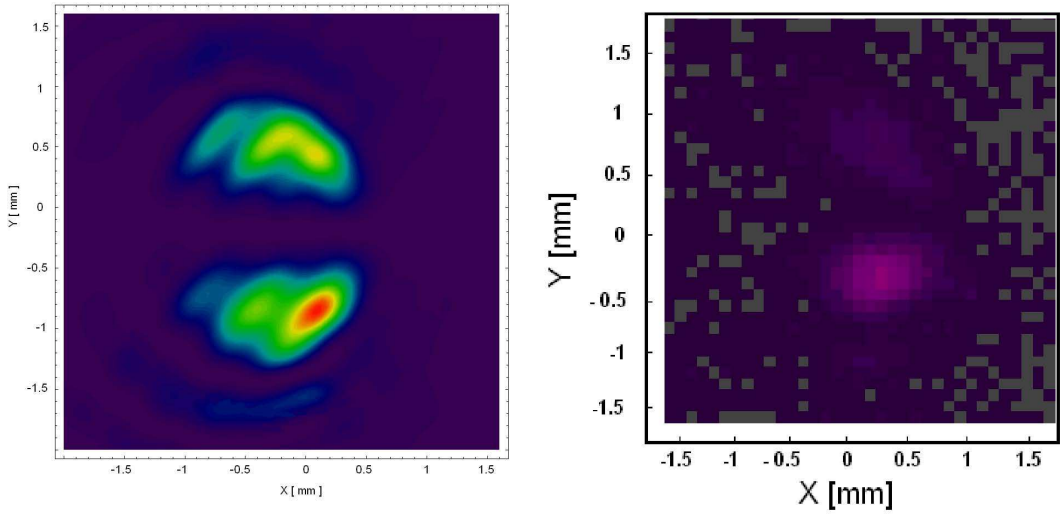

Figure 8.5: Right: The measured transverse profile at a wavelength of $\approx 80\ \mu$m. Left: The computed transverse profile.

the measured profile.

8.2 Sample experiments with rotating mirror spectrometer

8.2.1 First spectra in air and crystalline quartz window

The light path in the THz beamline CTR140 is entirely in vacuum ($\approx 10^{-1}$ mbar). At the exit port of this beamline in the experimental hut a vacuum vessel is placed. During the time between end of beamline commissioning and the arrival of the vessel all experiments had to be done in short distance of air. A crystalline-quartz window was the interface of the beamline to the air and the length in air, dependent on the setup, normally was close to 1.5 m. At a later time a LDPE[2] window also became available[3]. Figure 8.6 is a sample spectrum taken

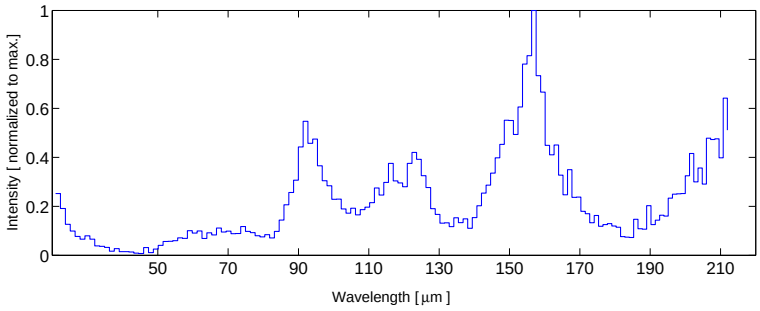

Figure 8.6: A sample spectrum (from a kicked bunch on off-axis screen) taken with transmission grating with pitch size of g=400 μm in 1.5 m path in air after CTR140 exit port. The interface of THz beamline to the air was crystalline-quartz window of 4 mm thickness. The intensities versus the part of the x axis below 50 μm do actually not correspond to wavelength contributions below 50 μm but show up as the tail of the zero-order radiation.

using rotating mirror spectrometer with transmission grating (RMS-TG). The pitch size of the grating is $\mathtt{g} = 400$ μm. The source is transition radiation of a kicked bunch on off-axis screen. This spectrum is neither corrected for geometrical acceptance factor $\mathtt{g}\cos\theta_1$ nor for grating efficiency. Structures are mostly either water absorption lines or pyroelectric detector resonances. The transmission of the crystalline-quartz, adapted from reference [69], is shown in Fig. D.1. At

[2]Low Density PolyEthylene

[3]The transmission of several materials including those that are used in the measurements of this chapter over infrared range are given in appendix D.

about 80 μm, the crystalline-quartz window has a short wavelength cut-off and there is a drop in intensity in Fig. 8.6. According to Fig. D.1 there are small intensities leaking in down to 50 μm which can be seen in Fig. 8.6 too. Intensities in the range below 50 μm (which is not anymore labeled with the same wavelength scale) is just the non-dispersed zero-order polychromatic radiation (with 4 mm thick crystalline-quartz window there is no transmission below 50 μm).
In order to check the wavelength calibration, THz filters were inserted in the path of the incoming radiation. The 155 μm band-pass filter[4] is inserted in the path of the radiation in the conditions similar to Fig. 8.6 and the result is shown in Fig. 8.7. The correction of the small discrepancies can be done by setting the angles in the readout code. In this way the precise angle of incidence of the radiation on the grating is determined.

A sample for longer wavelengths spectra which is recorded in the same conditions

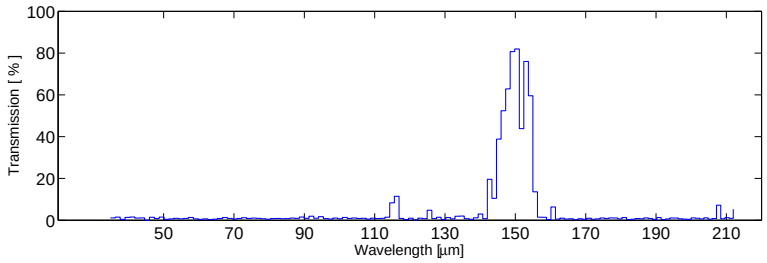

Figure 8.7: Sample wavelength calibration check (with 155 μm band-pass filter). The conditions for the measurement is the same as Fig. 8.6

as the previous spectra is shown in Fig. 8.8. The structures that are in the range of the previous spectrum (Fig. 8.6) look very much the same.

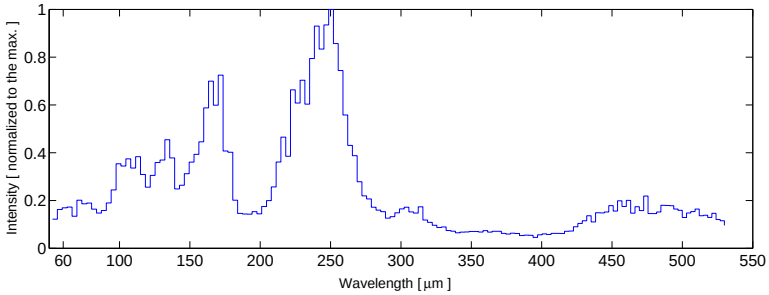

Figure 8.8: Long wavelength sample spectrum. The conditions for the measurement are the same as in Fig.8.6.

[4]Transmission of this filter, which was measured at BESSY, is shown in appendix B.

8.2.2 Spectra in air with LDPE window

The short wavelength cut-off can be pushed to shorter wavelengths if the crystalline-quartz is replaced by LDPE. The spectra of Fig. 8.9 and the blue curve in Fig. 8.10 are taken in such a condition. The structures in Fig. 8.9 are dominantly water-absorption. The cut-off at about 14 μm of the blue curve in Fig. 8.10 is due to LDPE transmission (see Fig. D.1).

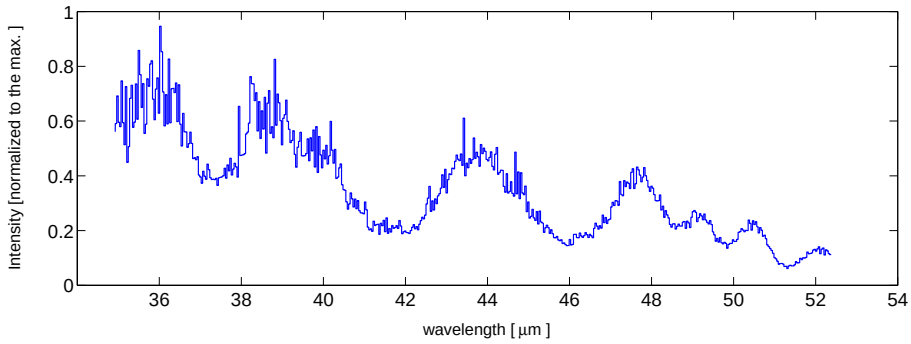

Figure 8.9: A spectrum taken with reflectance blazed grating with a pitch size of $g = 40$ μm in 1.5 m of air after CTR140 exit port from kicked bunch on off-axis screen. The interface to air is a LDPE window of 2 mm thickness.

8.2.3 Spectra in full vacuum and diamond window condition

This part contains the sample spectra recorded by a full in-vacuum setup. The red curve in Fig. 8.10 shows the spectra recorded using a reflectance blazed grating of the pitch size $g \approx 13\mu$m, and the blue curve is in the same conditions but in air with LDPE window. The valley at about 14 μm due to LDPE transmission disappears with a path that is fully in vacuum as it is shown in the red curve. This is also an indirect way to check the wavelength calibration of the spectrometer (see also Fig. D.1).
The next example (Fig. 8.11) is the extreme short wavelength range and it is a combined spectra recorded with RMS in vacuum using gratings of the pitch sizes $g_1 \approx 6.5$ μm, $g_2 \approx 4$ μm and $g_3 \approx 3$ μm. The steep drop in the intensity near 5 μm is due to the transmission of the diamond window (Fig. D.1).
Using the RMS spectrometer with two heads, one for filtering and one as disperser, the spectra of the electron bunches subjected to transition radiation are

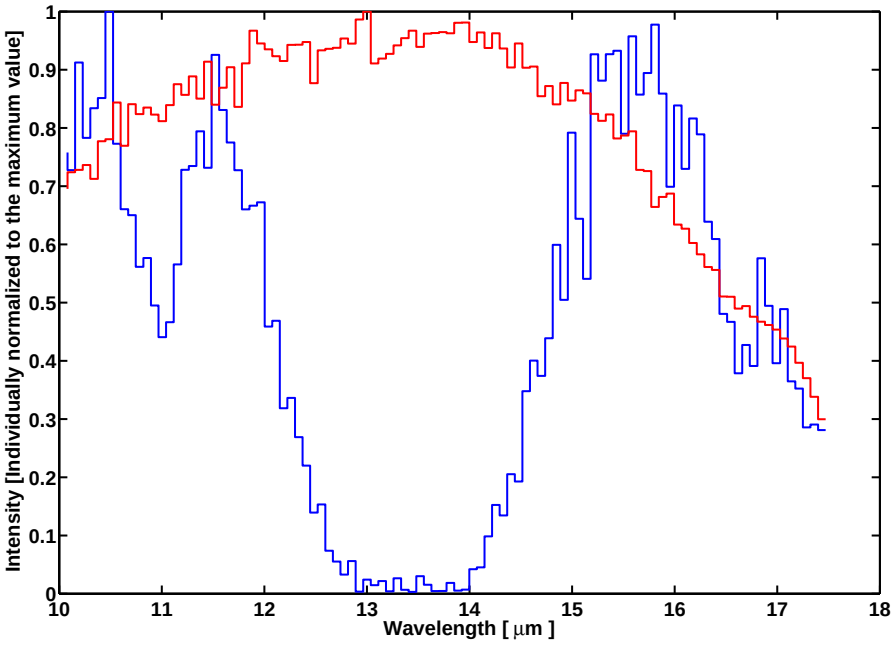

Figure 8.10: Comparison of spectra taken with LDPE as the interface to air, in blue, and a spectrum in full vacuum condition with diamond window (which is always there, see the first element in the CTR140 beam-line in Fig. 8.1), in red.

possibly recorded in different conditions of the machine. In principle, it is possible to deconvolute the detector response function, gratings efficiencies and bunch charge dependence of the spectra and then, combining the spectra that are measured successively, the broad-band spectrum can be determined in an average sense. In order to do such a broad-band measurement with RMS, the changes

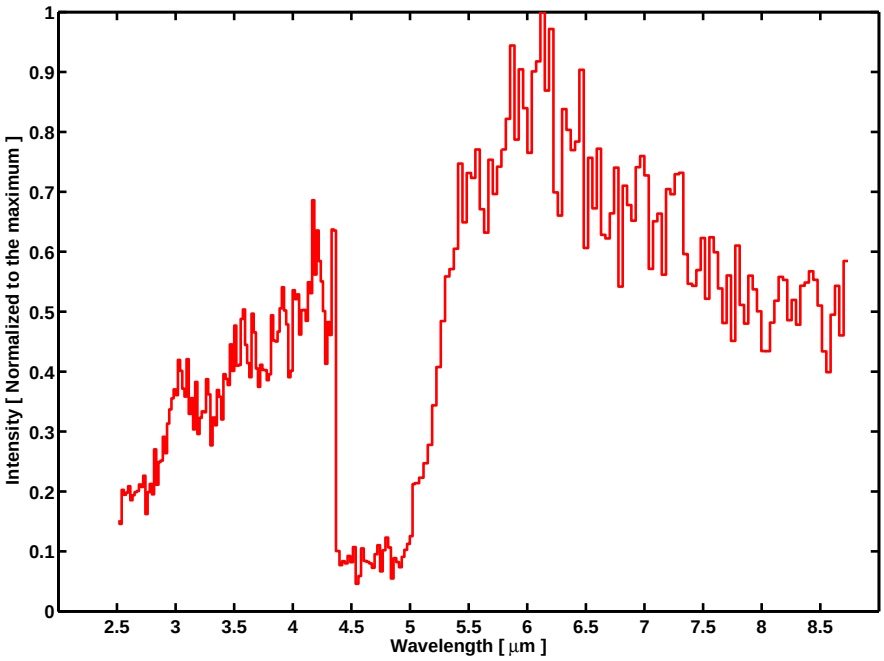

Figure 8.11: Combined spectra taken with reflectance blazed gratings of different pitch sizes of $g_1 \approx 6.5\mu m$, $g_2 \approx 4\mu m$ and $g_3 \approx 3\mu m$.

in the machine and their effect on the spectra should be considered. Despite the fact that the reproducibility of the result in a qualitative sense is proved, getting reasonable broad-band spectra requires to have the single shot spectrometer. Machine fluctuations are too large to expect an average behavior close to the instantaneous spectra. This becomes evident when the result of single-shot spectrometer are discussed.

8.2.4 Experimental investigation on the comparison of CTR and CDR

An experimental evidence of the suppression of short wavelengths for diffraction radiation is shown in Fig. 8.12. The coherent diffraction radiation spectrum is from an electron bunch having its centroid 6 mm away from the DR screen (the off-axis screen was inserted but no bunch was kicked onto it). The coherent transition radiation spectrum is recorded when an electron bunch is kicked to the off-axis screen. Both spectra are measured in the same conditions of the FLASH machine, THz beamline and the spectrometer. This shows, qualitatively,

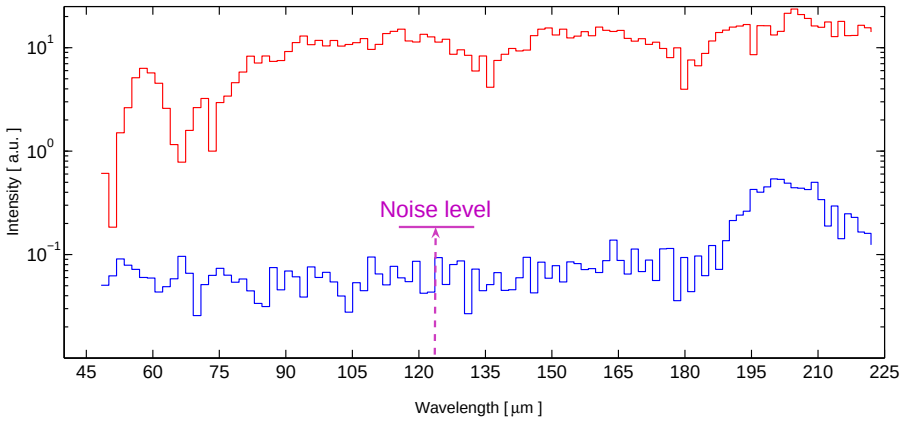

Figure 8.12: Coherent transition radiation (red) and coherent diffraction radiation (blue) are measured. Golay-cell (see section 5.2) detector was used with the RMS spectrometer in air. The electron beam centroid was 6 mm distant from the edge of the diffraction radiator screen when coherent diffraction radiation spectra was measured.

the strong suppression of generation of (see also Fig. 3.4) short wavelengths when DR screen is used. In order to study the most interesting part of the spectrum which is wavelength range well below 200 μm TR has to be used.

8.2.5 Detector response studies

Different detectors including a Golay-cell, standard Infratec $LiTaO_3$ pyroelectric detector and the specially designed $LiTaO_3$ pyroelectric detectors of different types (see section 7.2) can be mounted as detector in the RMS. Then the response function of these detectors can be studied. Figure 8.13 shows the etalon resonances

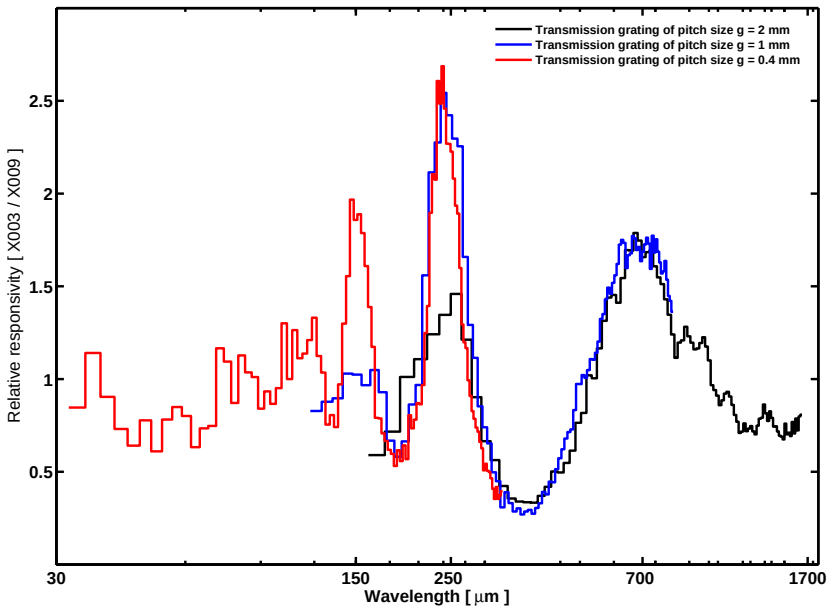

Figure 8.13: Relative response function of two pyroelectric detectors: X003 and X009.

of the standard pyroelectric detector, X003, relative to a specially designed one, X009 (for more details see section 7.2). The ratio is measured using three different transmission gratings. For larger pitch sizes the resolution decreases. For a poor resolution the resonance becomes less pronounced and partially averages out.

8.3 Sample experiments with the prototypes of the single shot spectrometer

Experiments with eight-channel single-shot spectrometer

In Fig. 8.14 and Fig. 8.15 the raw spectra as they appear in the ADC channels are shown. Each figure shows a shot recorded when the grating with pitch size of $\mathtt{g} = \mathtt{40}\ \mu\mathtt{m}$ was inserted. Figure 8.14 is a shot recorded when one bunch was

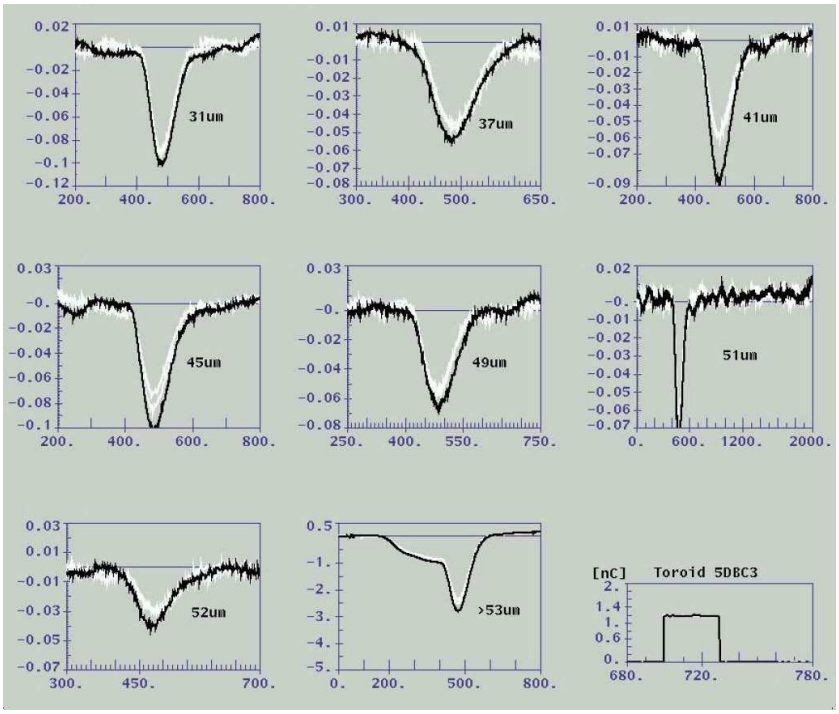

Figure 8.14: Single-shot spectrum recorded by eight-channel single-shot spectrometer. Each individual ADC channel spectrum shows the output of the integrating amplifier that corresponds to the specific channel. The horizontal axis is time and every $\approx \mathtt{13}$ units correspond to 1 $\mu\mathtt{s}$ (The toroid time scale is in $\mu\mathtt{s}$ and shows 30 $\mu\mathtt{s}$ for thirty bunches). This shot is taken when one bunch is kicked out of the train of many bunches. In the middle plot of the third row a long tail is present which is the contribution of the non-kicked bunches that pass several millimeters away from the screen and produce diffraction radiation. This radiation is horizontally polarized and can be suppressed if a polarizer is used.

kicked out of a train of many bunches. For short wavelength channels there is no contribution from non-kicked bunches, but in the last channel, where long wavelengths are integrated, the contribution is clearly visible. Figure 8.15 is a single bunch operation and there is no contribution of coherent diffraction radiation in any of the channels. The pulse width for the signal that corresponds to the kicked bunch is $\approx 4\ \mu s$ (The horizontal axis is time and every $\approx$ 13 units correspond to 1 μs) due to the relatively long integration time of the detector amplifier. The shortest bunch spacing at FLASH is 1 μs (1 MHz mode as was the case for the measurements of Figures 8.14 and 8.15), thus a pulse width of 4 μs (or longer) potentially could limit the multi-bunch operation[5]. The more interesting short wavelengths appear only when a kicked bunch on off-axis screen produces transition radiation. In this case the other bunches are far enough from the screen and do not contribute to the short wavelengths content.

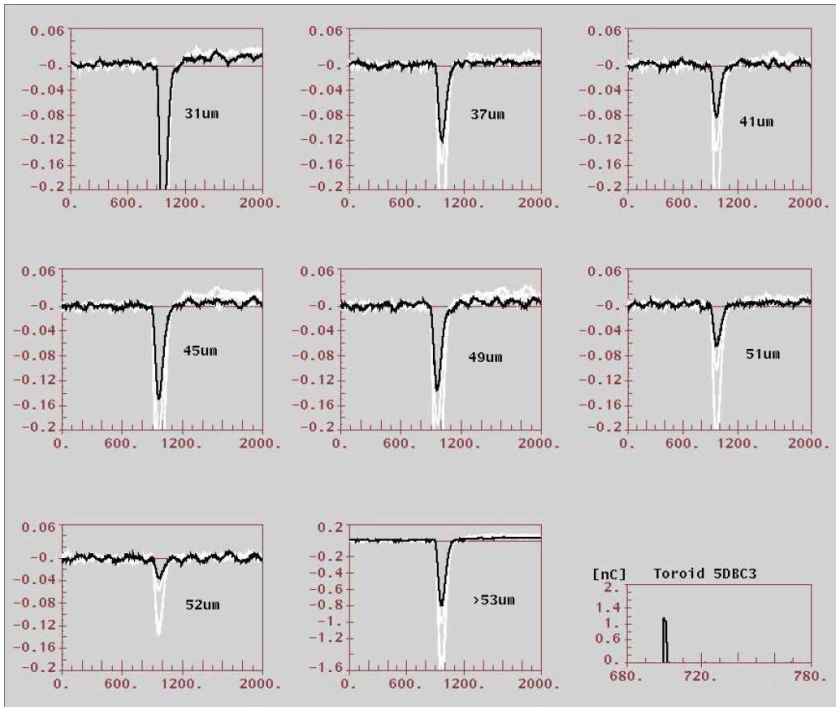

Figure 8.15: Same as Fig. 8.14 but for a single bunch operation that is kicked on off-axis screen.

[5]This applies, for instance, when coherent synchrotron radiation is used as the source with the present detector amplifier (response pulse width 4 μs) and if single bunch profile is desired.

Elementary SASE correlation studies

The result of a sample measurement made using four-stage ABCM (see section 6.2.2), is shown in Fig. 8.16. The off-crest phase of the first accelerating module has been varied over the range that is shown and for each phase the signals in different channels of the ABCM and the SASE signal (from another bunch in the train) were recorded. The signal at wavelengths longer than 90 μm, which is equivalent to the ordinary pyroelectric BCM varies monotonically, while the signals that are in the wavelength range of 20 μm, 40 μm and 75 μm exhibit a peak. In fact the channel that corresponds to a wavelength of $\approx$ 40 μm has the strongest correlation to the SASE signal because they both show a sharp peak at the same phase.

In Figures 8.17 and 8.18 two correlation runs are shown. These plots are scatter

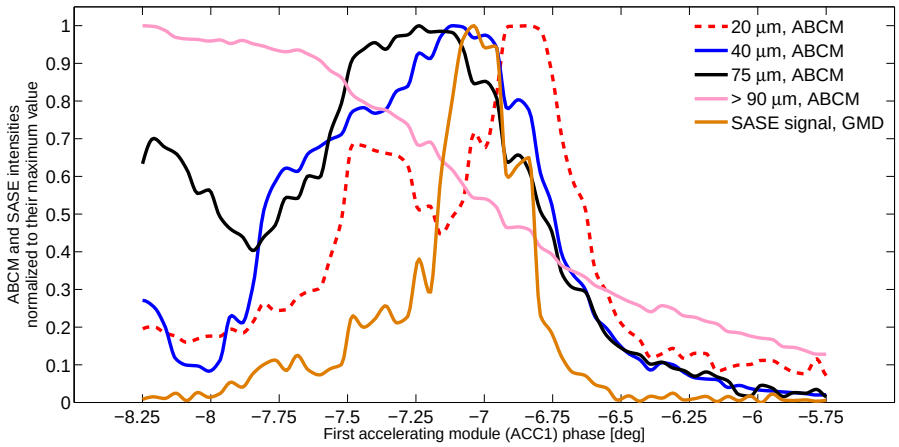

Figure 8.16: Spectrally resolved bunch compression study and correlation to SASE signal using ABCM (see section 6.2.2).

plots of many shots such that in each shot one bunch is kicked to the off-axis screen to record the spectra and another bunch is used to read its SASE signal. Wavelengths as short as 32 μm are resolved. The last plot in each figure is the zero-order long wavelengths, which is in agreement with the BCM correlation plot of Fig. 8.19. The correlation properties at short wavelengths are clearly different from those at longer wavelengths. In Fig. 8.20 another correlation plot that was made using the four-channel multi-stage device is shown. Here, a weak anti-correlation for very short wavelengths and correlation for intermediate wavelengths to the SASE signal can also be seen.

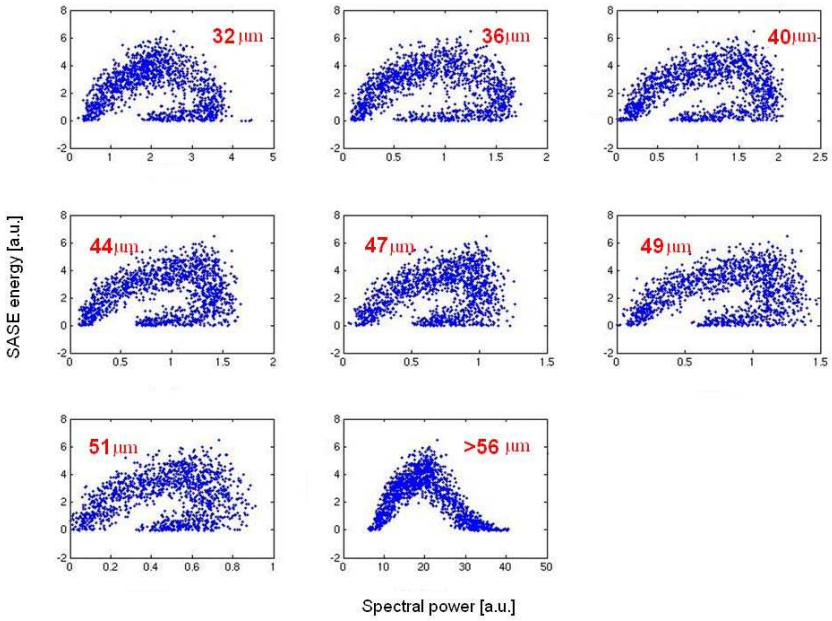

Figure 8.17: SASE correlation to the coherent transition radiation spectra recorded by eight-channel device. In each plot the vertical axis is the SASE energy and the horizontal axis is the intensity of CTR at the wavelength which is mentioned.

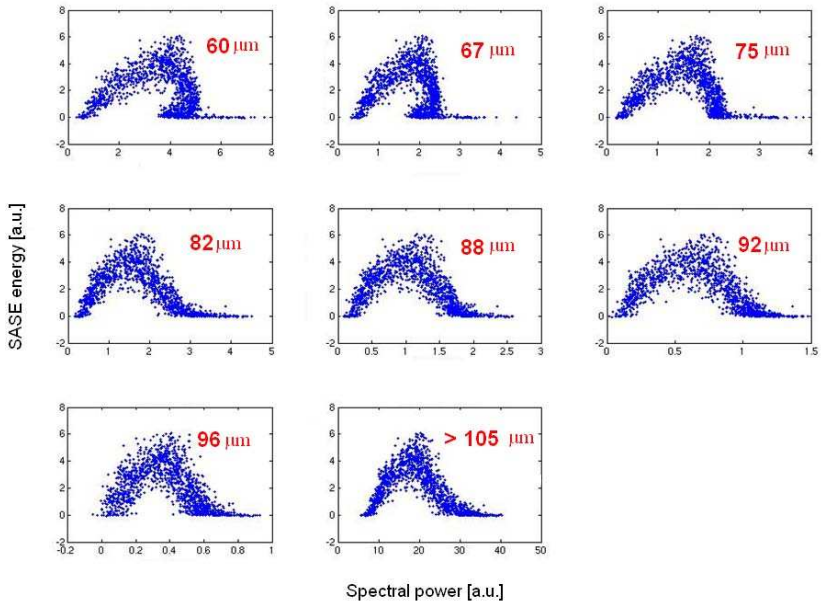

Figure 8.18: SASE correlation to the coherent transition radiation spectra, in a different range of wavelengths than that of Fig. 8.17.

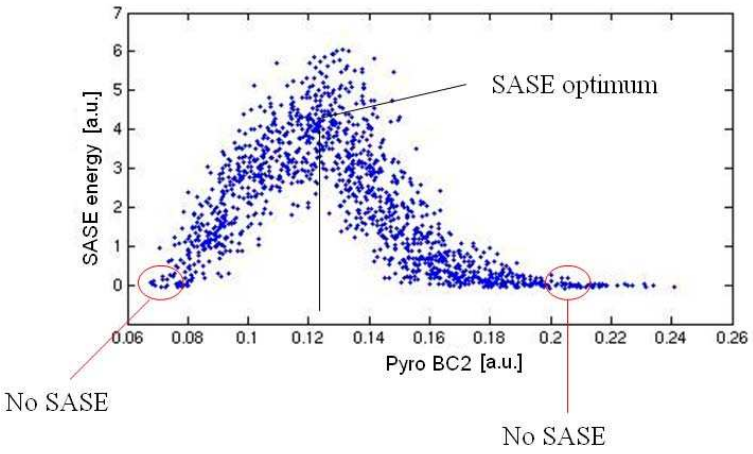

Figure 8.19: SASE correlation to the integrated diffraction radiation signal of the bunch compression monitor (first bunch compressor BC2).

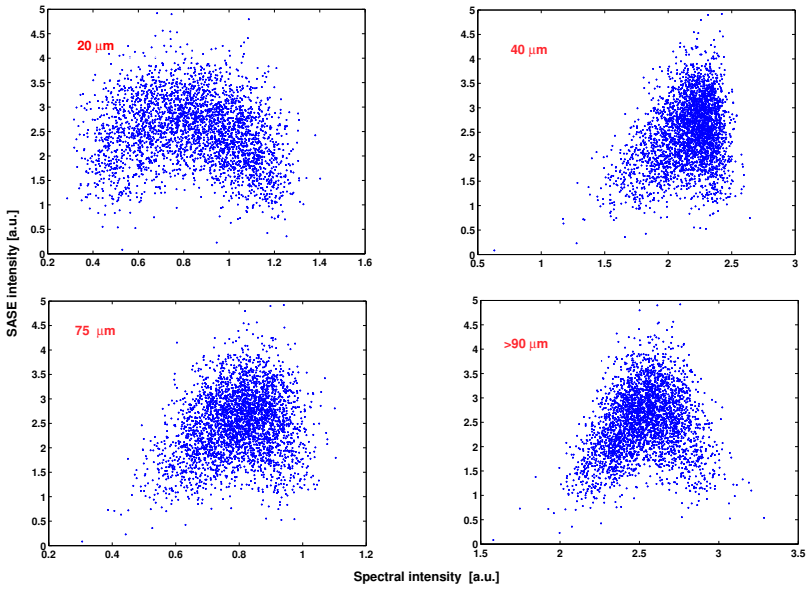

Figure 8.20: Four channel multi-stage device is used to study the correlation of intensities in different wavelengths of the coherent transition radiation to the SASE signal.

8.4 Experiments with a one-stage spectrometer

The experimental setup is composed of a one-stage spectrometer and two machine heads (see section 6.1). Operating in single shot mode, CTR spectra for different accelerator settings were recorded. Figure 8.21 is a sample of the combined results. These spectra were recorded in parallel to the FLASH machine user operation at a SASE wavelength of 13.1 nm. Each color in the figure corresponds to a different grating with a specific pitch size to cover the range which is shown. The plotted spectra are averaged over several hundreds of individual shots that were recorded single shot.

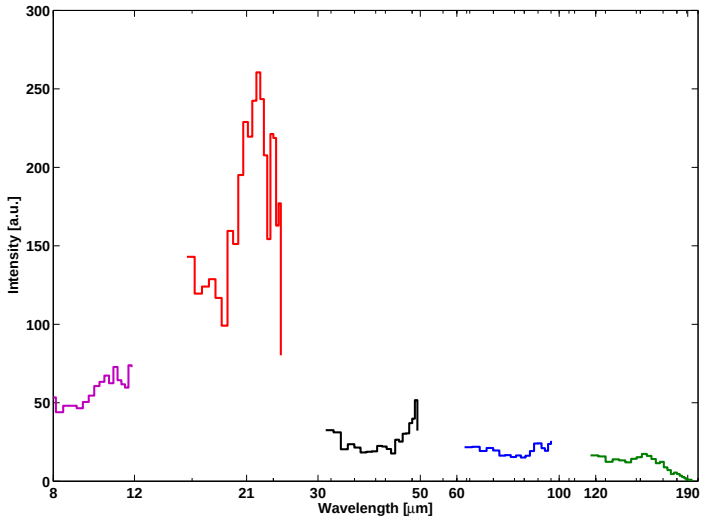

Figure 8.21: One-stage single-shot spectrometer used with reflectance blazed gratings of different pitch sizes to record CTR spectra over a relatively wide range. These spectra were recorded in parallel to the FLASH machine user operation at a SASE wavelength of 13.1 nm.

Bunch length

For a Gaussian bunch profile, which can be expressed by $\frac{1}{\sqrt{\pi}\sigma_t}\exp(-\frac{t^2}{\sigma_t^2})$, the full-width at half maximum is given by $\mathtt{FWHM}_t = 2\sqrt{\ln 2}\sigma_t$. The frequency domain form-factor is also a Gaussian given by $\frac{1}{\sqrt{2\pi}}\exp(-\frac{\sigma_t^2\omega^2}{4})$. For the short wavelengths, the single electron transition radiation spectrum can be considered constant (see Fig. 3.4). Then, the wavelength domain coherent radiation spectrum will be proportional to $\left(\exp(-\frac{\sigma_t^2\pi^2c^2}{\lambda^2})/\lambda\right)^2$. Differentiating the wavelength

domain spectral intensity with respect to the wavelength, it can be seen that $\lambda_{\mathtt{I=max}} = \frac{\pi \mathtt{c}}{\sqrt{2\sqrt{\ln 2}}}\mathtt{FWHM_t}$ or

$$\lambda_{I=max}(\mu m) = 0.8\ FWHM_t(fs) \tag{8.1}$$

In Fig. 8.21 the combined spectrum peaks at about $\approx 21\ \mu\mathtt{m}$ and accordingly corresponds to a $\approx 25\ \mathtt{fs}$ FWHM of the peak in time domain profile.

The next sample study that is made using the one-stage spectrometer is the bunch profile differences along the train when different bunches of the train are kicked to the off-axis screen to record their CTR spectra. In Fig. 8.22 the mea-

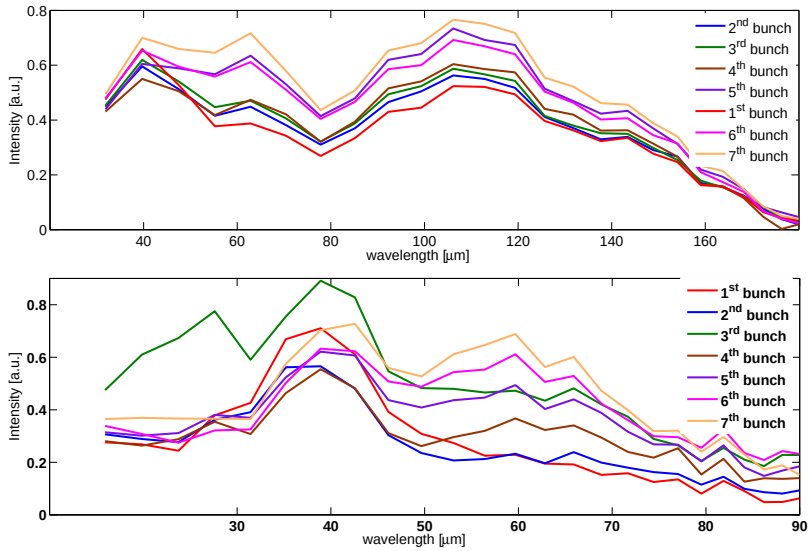

Figure 8.22: Differences in the CTR spectra of different bunches along the bunch train. Top and bottom plots are spectra (averaged over several hundreds single shots) using transmission gratings with the pitch sizes of $\mathtt{g} = 200\ \mu\mathtt{m}$ and $\mathtt{g} = 100\ \mu\mathtt{m}$, respectively.

sured spectra of seven successive bunches are shown. In the upper plot a transmission grating with a pitch size of $\mathtt{g} = 200\ \mu\mathtt{m}$ was used and for the lower plot $\mathtt{g} = 100\ \mu\mathtt{m}$. These spectra are corrected for their corresponding bunch charge and, therefore, the relative intensities are directly related to the bunch profile differences. The peak of the spectra occurs at the same wavelength and according to Eq. 8.1 this means that all bunches have the same $\mathtt{FWHM_t}$ in the time domain. The different intensities at the wavelength of the peak can translate to the different peak current of the electron bunches.

8.5 Experiments with the two-stage spectrometer

8.5.1 Spectra as a function of machine parameters

The bunch compression scheme that is implemented at FLASH uses an energy chirp that is introduced to the bunch by an accelerating module. The longitudinal profile of the electron bunches and accordingly their coherent transition radiation (CTR) spectra depend strongly on the phases of different accelerating modules. The two-stage spectrometer is used to study the variation of the CTR as a function of the phases.
The linac settings that correspond to SASE operation were chosen as the starting point and any change has been made with respect to these reference values. These would guarantee the necessary conditions on good transmission and electron beam optics as well as low losses in the undulator. In addition, starting from these conditions can help to produce useful results for machine operation. In Fig. 8.23, a snapshot of the interface of the read-out tool of the MCP-detector

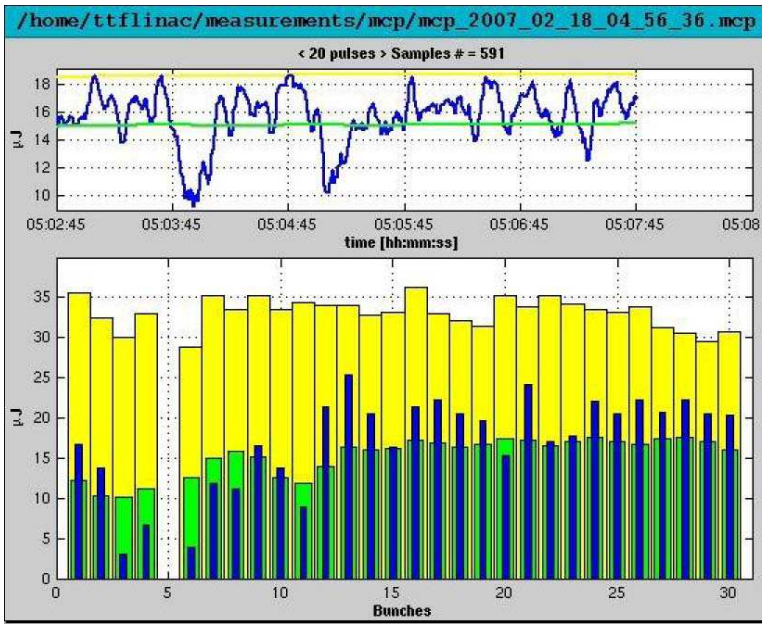

Figure 8.23: SASE level measured by the MCP detector during February 2007 measurement period (see text for details).

is shown. The MCP-detector is one of the two tools to measure the SASE intensity. The key element of this detector is a wide dynamic range Micro-Channel Plate (MCP) which detects scattered radiation from a thin gold wire crossing the

photon beam [62]. Figure 8.23 shows the SASE intensity during the accelerator study period in February 2007. It shows a relatively high SASE level that is obtainable during a machine study run. For each bunch there are three type of bars (the fifth bunch was kicked to the CTR140 screen and therefore is absent in the bar plot) in the lower part of the figure. In the following the time interval from the shot that the read-out tool is loaded to the actual shot is denoted by $\mathcal{T}_{run}$. The green bars are the average of SASE intensity over $\mathcal{T}_{run}$ for each bunch. The SASE intensities which correspond to each of the bunches in the actual shot are shown with the blue bars. The yellow bars show the maximum SASE intensities of the corresponding bunches over $\mathcal{T}_{run}$. For each shot, the average of the SASE intensities of all bunches in the train can be considered as a measure for the entire train. The result of a smoothening of the average SASE intensities of the trains over the last 20 shots ending to the actual shot is shown in the blue curve of the upper plot. The green curve is the average of the blue curve over $\mathcal{T}_{run}$. The yellow curve is the maximum value of the blue curve over $\mathcal{T}_{run}$. The fifth bunch is kicked to the CTR140 screen and does not enter the undulator (those electrons that are left after hitting on the CTR screen get absorbed by the collimator upstream of the undulator).

In Fig. 8.24 the result of a scan over the off-crest phase[6] of the first accelerating module (ACC1) at FLASH is shown. All the other settings of the accelerator including the RF settings and the electron beam optics are loaded from a SASE operation mode. The slow feedback system which regulates the compression by fine tuning the ACC1 phase was switched off. The quadratic dependence of the spectra on the bunch charge reading for each shot are removed from the spectra. With this format of the plot it is hard to see the entire changes over the scan range. A top-view can be more useful. The fact that the spectrometer is not yet calibrated in terms of the absolute intensity (the correction function includes the detector response function of Fig. 7.7 but there are more factors expected) requires more careful analysis of the data. Nevertheless any calibration factor can be removed by dividing the readings over the run for each detector by the value of the maximum intensity that is read on that detector. The drawback is that the information contained in the spectra are reduced to only showing the dependence of the relative intensity (normalized to the maximum intensity) at each wavelength on the ACC1 phase. The density plot in Fig. 8.25 shows the

[6]The on-crest phase is determined by centering the beam spot on an Optical Transition Radiation (OTR) screen downstream the module. The precision in this method is better than one degree. The importance of the on-crest phase determination is for the comparison of the measurements with the simulations. Nevertheless, when the signals of the SASE detector and the CTR spectra are recorded simultaneously, the correlated changes are conclusive, independent of the phase values.

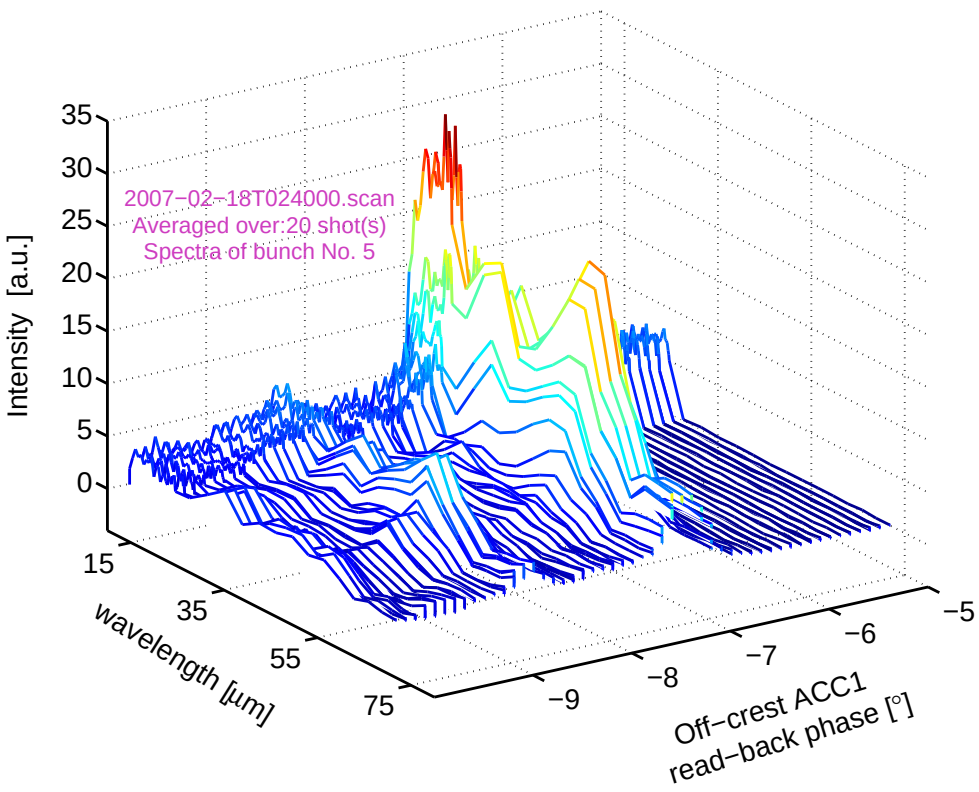

Figure 8.24: CTR spectra as a function of the off-crest phase of the first accelerating module at FLASH. All the other settings of the accelerator including the RF settings and the electron beam optics are loaded from a SASE operation mode. The slow feedback system which regulates the longitudinal compression by fine tuning the ACC1 phase is switched off. The quadratic dependence of the spectra on the bunch charge reading for each shot are removed from the plotted spectra (see text for more details).

same data as Fig. 8.24. The vertical axis is the off-crest phase. The horizontal axis of the density plot is the wavelength of the CTR spectra. The range in 15 to 25 μm is resolved by the RBG unit and the longer wavelengths are covered by the TG unit. For each of the phase steps, twenty shots are recorded and then the average values are normalized in the following way. The signals in each of the individual channels, or wavelength, are normalized to the maximum value of the signals at that channel over the entire run. In this way all possible calibration factors including the detector response, are removed. After such a normalization the possible correlations between the CTR spectra and SASE signals, independent of the signal level, can show up. In other words, without such a normalization, when the signal is much stronger at part of the spectra, the variation of the weak signals are not clearly observable. The single column in the left side of the density plot shows the normalized (to its maximum over the entire run) SASE signal. The middle plot is combined to provide information on the changes of the accelerating modules, either on purpose or due to machine fluctuations. All the gradients and phases of different modules are stable within an acceptable level and only ACC1 shows the expected changes. The two other strongly fluctuating signals are the charge of the kicked bunch and the bunch that is used to read its SASE signal. The lowest plot shows the integrated CDR signals measured using single pyroelectric detectors (BCM). The PyroBC2 measures the radiation of a diffraction radiation source at a position downstream of the first bunch compressor. PyroBC3 is the same installation at the second bunch compressor. These signals are read for the bunch that later is kicked to the CTR140 screen. These bunch compression monitor signals and the CTR spectra are all normalized to the squared kicked bunch charge. In this way the presumed quadratic bunch charge dependence of these signals are removed. The same type of the normalization is made for the SASE signal. The clear conclusion that can be drawn from such a scan is that the peak of the spectra which is recorded on the relatively short wavelengths of 15 to 70 μm, appears at phases close to the region of SASE mode operation, while at the same time none of the two classical bunch compression monitors (BCM) identify this region. The operating BCMs at FLASH are in a short distance ($\approx 1\ m$) in air after the interface with the UHV beam-pipe of the accelerator which is a crystalline-quartz window. According to the transmission of the crystalline-quartz window (see Fig. D.1) it is clear that these BCMs do not detect any intensity from short wavelengths that are shown in Fig. 8.25. The more basic problem with a BCM that measures the coherent diffraction radiation (CDR) is the fact that the generation of the short wavelengths is highly suppressed (see Fig. 8.12). A BCM which is housed in vacuum after a diamond window (see Fig. D.1) as the interface to the UHV of the accelerator can avoid

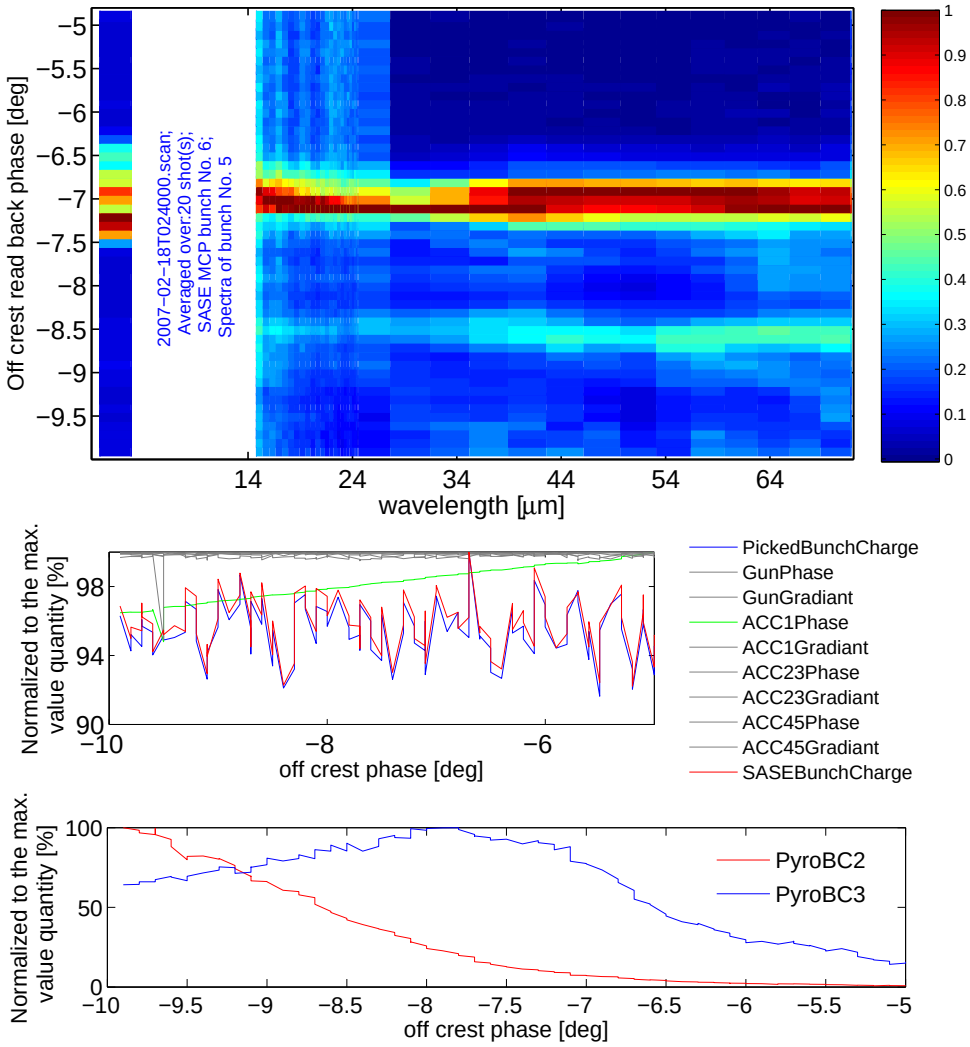

Figure 8.25: Top: First accelerating module (ACC1) phase scan. At each phase-value step in the scan range the CTR spectra of 20 shots are recorded and for each of these shots the read-back phase (which can be slightly different with the input-phase) is read and the average value over these 20 shots (which has very small standard deviation) is used for the plot. The single column in the left side of the CTR spectra density plot is the SASE energy (averaged over 20 shots) readings by the MCP-tool that is normalized to the maximum value over the run. The two other plots show the machine changes over the run. For these data the same averaging over 20 shots is carried out.

the first problem. Measuring coherent synchrotron radiation (CSR) provides a non-invasive source that contains short wavelengths. Nevertheless the results that can be obtained using an ABCM cannot be expected from a measurement based on the integrated radiation intensity (see section 8.3).
An extension of the resolved range to shorter wavelengths is shown in Fig. 8.26. As it was stated in section 6.4, in the set-up of the spectrometer it is foreseen to have different gratings on the linear movers. For each stage, the gratings of different pitch sizes can be inserted and by selecting an appropriate combination it is possible to cover different ranges. The range covered by the reflectance grating unit is from 5 to 9 μm. The region 9 to 15 μm covered by the transmission grating (with pitch size g = 100 μm) is different from the rest of the spectra. This is due to the fact that this transmission grating cannot disperse this short wavelength range from the zero-order. In other words, the intensities arrived at the corresponding detectors in the range 15 to 25 μm were not purely from the wavelengths that are labeled in the plot. In the scan shown in Fig. 8.25 that the entire wavelength range 15 to 25 μm is covered by the reflectance grating the density plot does not show a behaviour similar to what can be seen in Fig. 8.26 over wavelength range 15 to 25 μm.
In the range from 5 to 9 μm there are structures in the bunch that are not correlated to the SASE signal, and they appear to become stronger at smaller off-crest phases. There is another region (off-crest phase between -8.5 to -8 degrees) where at wavelengths longer than $\approx$ 35 μm intensities show a local maximum and no SASE signal is observable. Two samples of studies on other modules are shown in Fig. 8.27 for the gun phase and in Fig. 8.28 for the second accelerating module (ACC23). The range over which the phase of the gun can be changed is limited. For phase values far from the so called "start of the charge"[7] phase for the gun, a complex mixture of the transverse and longitudinal beam dynamics effects brings the machine to a situation with no transmission to the CTR140 screen. In general the results of these scans are difficult to interpret but the maxima of the spectral signal still are close to the high SASE regime.

[7]Dependent on the gun RF phase, the electrons at the cathode may feel a decelerating field and not able to leave the region close to the cathode. With increasing accelerating field on the cathode region electrons start to escape the region, this condition is called "start of the charge".

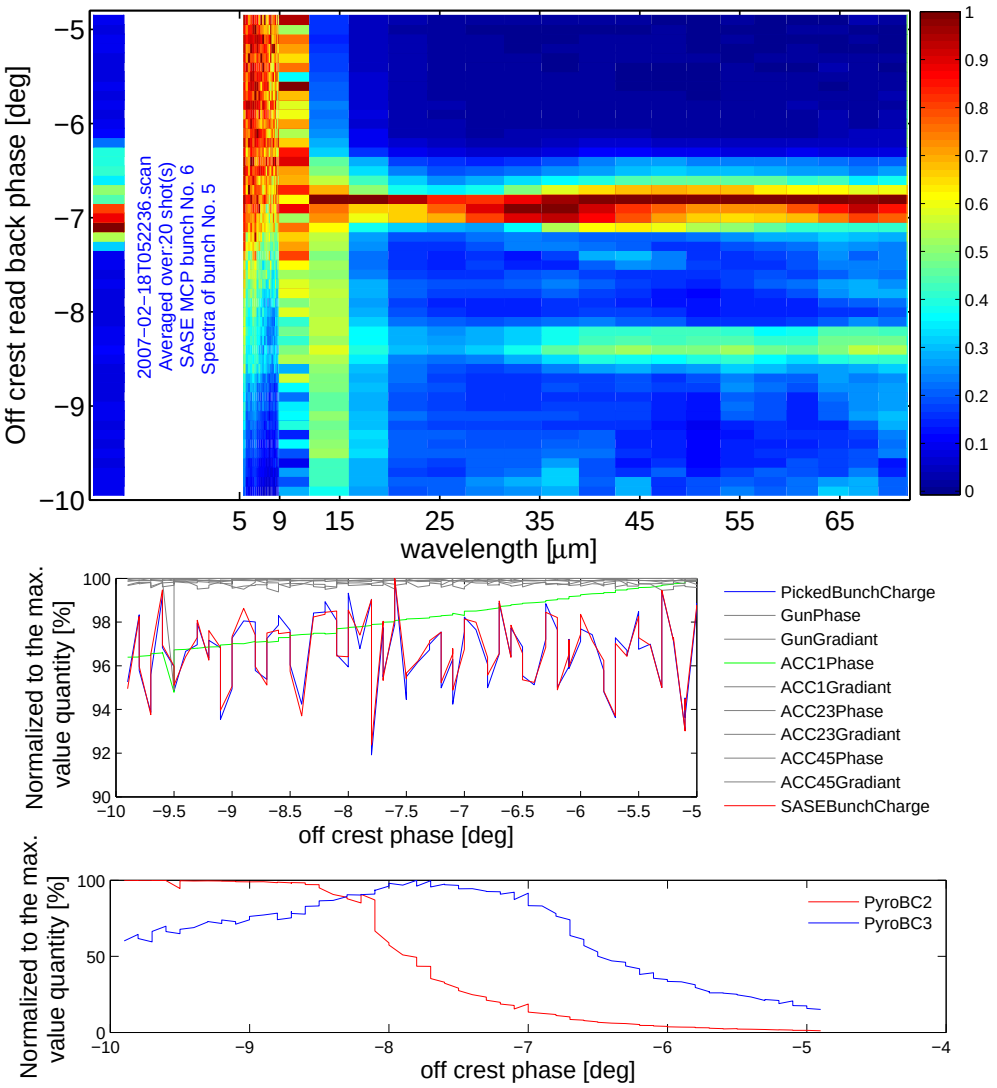

Figure 8.26: Same as Fig. 8.25 but shorter wavelengths are covered, too. The range covered by the reflectance grating unit is from 5 to 9 μm. The rest is covered by a transmission grating of the pitch size g = 100 μm. In the scan shown in Fig. 8.25 that the entire wavelength range 15 to 25 μm is covered by the reflectance grating the density plot does not show a behaviour similar to what can be seen here over wavelength range 15 to 25 μm. This is due to the fact that the used transmission grating cannot disperse short wavelength range 9 to 15 μm from the zero-order (see text for more details).

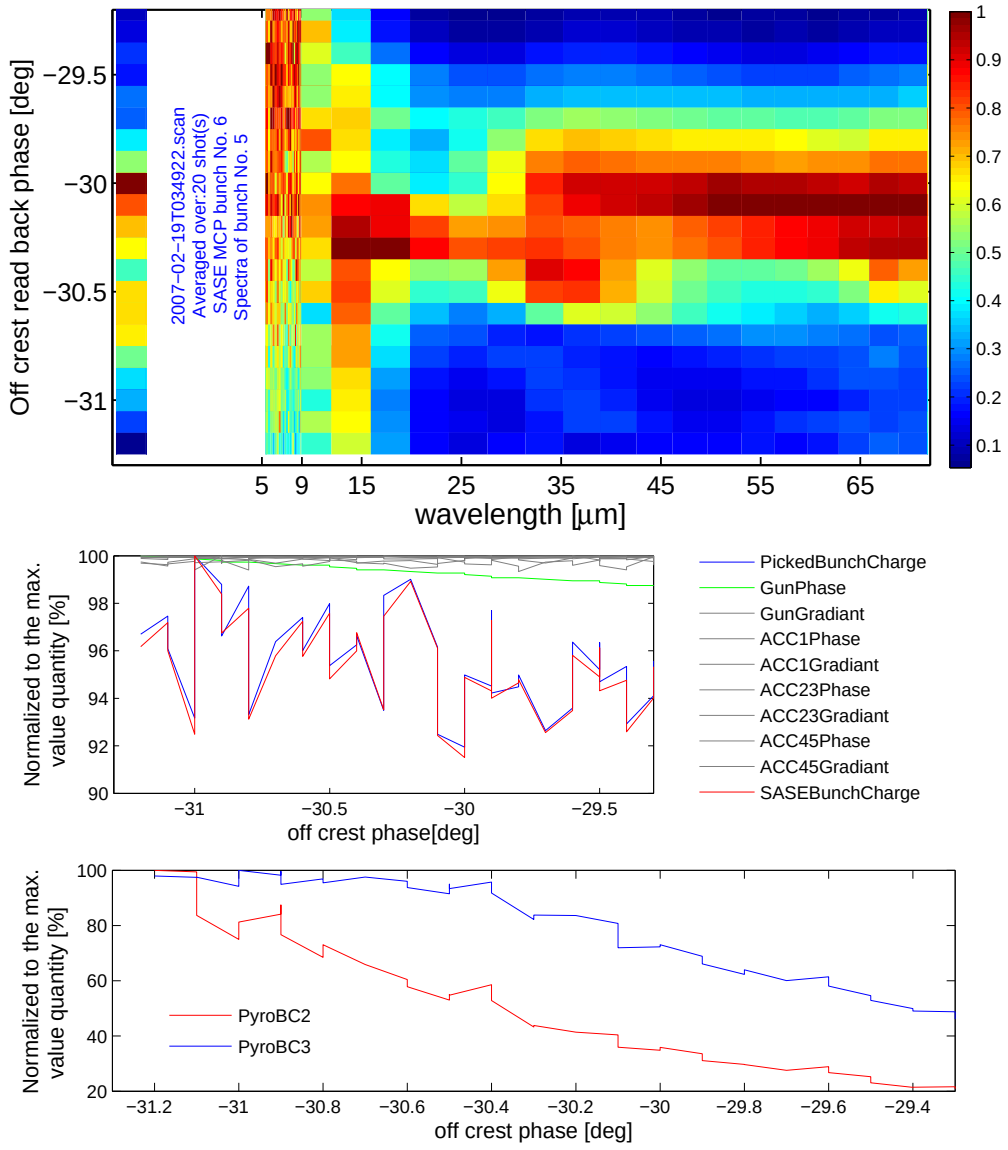

Figure 8.27: GUN phase scan. The range covered by the reflectance grating unit is from 5 to 9 μm. The rest is covered by a transmission grating of the pitch size g = 100 μm (see text for more details).

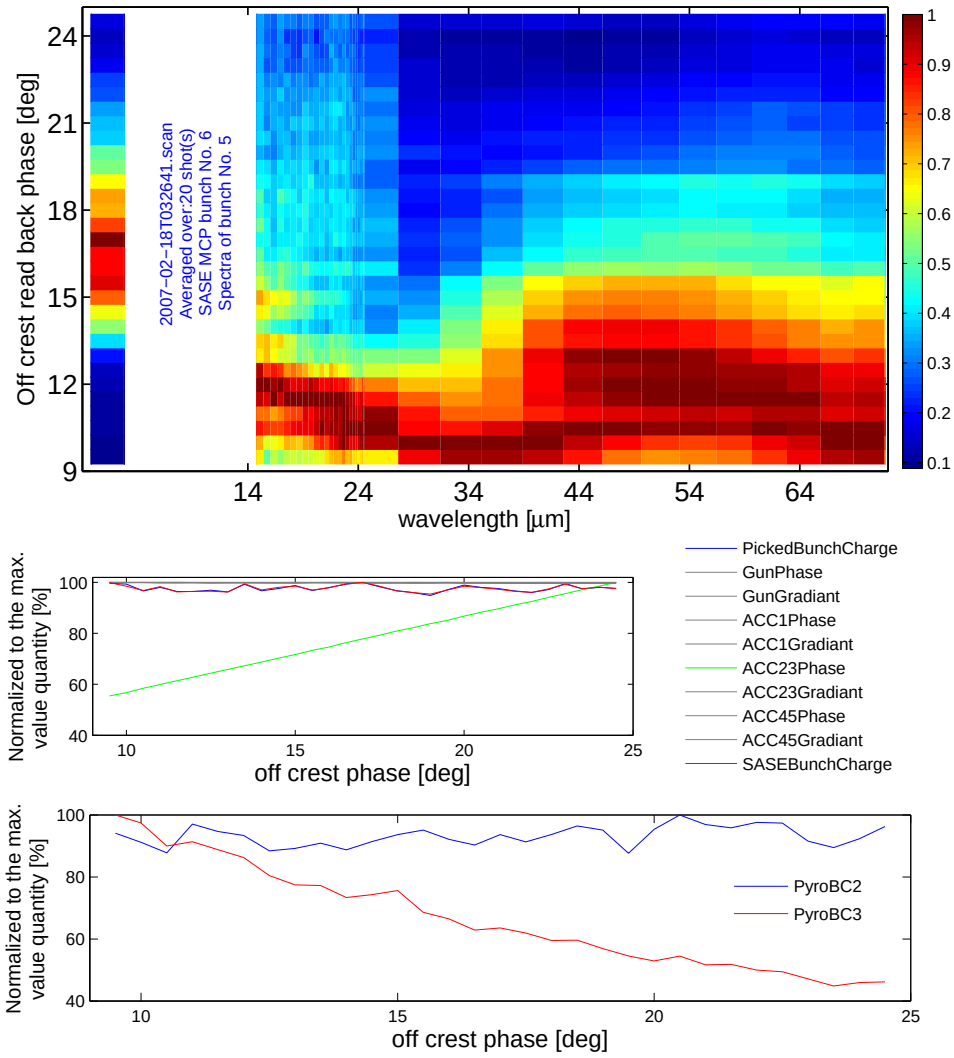

Figure 8.28: ACC23 phase scan. The range covered by the reflectance grating unit is from 15 to 25 μm. The rest is covered by a transmission grating of the pitch size g = 100 μm.

8.5.2 SASE mode spectra and SASE correlation studies

In this section measurements are presented which were carried out during stable SASE operation. This means that machine was tuned for a relatively high SASE intensity during either an accelerator study or VUV photon user period. During these measurements, none of the machine parameters changed intentionally. The only small but controlled change happens when the slow feedback system (that stabilizes the longitudinal compression) or the charge feedback act to keep their target parameters. The remaining changes, which are dominant, are unwanted drifts of phases or gradients of the accelerating modules or other perturbations like injector instabilities. SASE itself is a statistical process in the sense that starting from noise amplification has naturally its relatively large fluctuations. In Fig. 8.29 an example of a stable run is shown. The data presentation is done in the same way as it was explained for the density plots of the previous section. The only difference is that the SASE signal and the CTR spectral data are averaged with a moving window in which the data points are averaged (smoothening the data) with a step size which is mentioned in each of the plots. Instead of changing an off-crest phase, only successive shots are recorded, therefore the "off-crest phase" values are replaced by "shot number" which means an average spectrum over the last n shots that are recorded (n is the number of the shots over which the data is averaged). For stable run measurements an average spectra over the entire run makes sense. This is shown in Fig. 8.30 for the same shots as Fig. 8.29. The density plot shows a very clear correlation of the spectral changes and the SASE signal variations (with the CTR spectra one cannot study the correlation of the CTR spectra and the SASE signals of the same bunch and these correlations correspond to the changes of the entire train). In Fig. 8.29 the spectra of the bunch number five of each train are recorded while the SASE signals, in this run, are from first bunch. In order to interpret these results in a qualitative manner, three different regions could be identified. The wavelength region shorter than $\approx 35\ \mu\mathrm{m}$, the region between 35 to $45\ \mu\mathrm{m}$ and the region longer than $45\ \mu\mathrm{m}$. For relatively strong signals in the first and the third regions, SASE signal drops to the half of its maximum value. In the contrary, when these regions exhibit relatively weak signals and the signals in the second region are strong, SASE signal is at maximum. Therefore, if the spiky part of the bunch profile is uniform it could produce higher SASE signals. The wavelength region 35 to $45\ \mu\mathrm{m}$ (in this run which was to produce the 30 nm wavelength VUV SASE) are the most correlated part of the spectra to the SASE signal. Quantitative correlation function gives the same impression about the most correlated part of the spectra, Fig. 8.30.

The signals in every single channel (CTR spectra or SASE signal) during the run

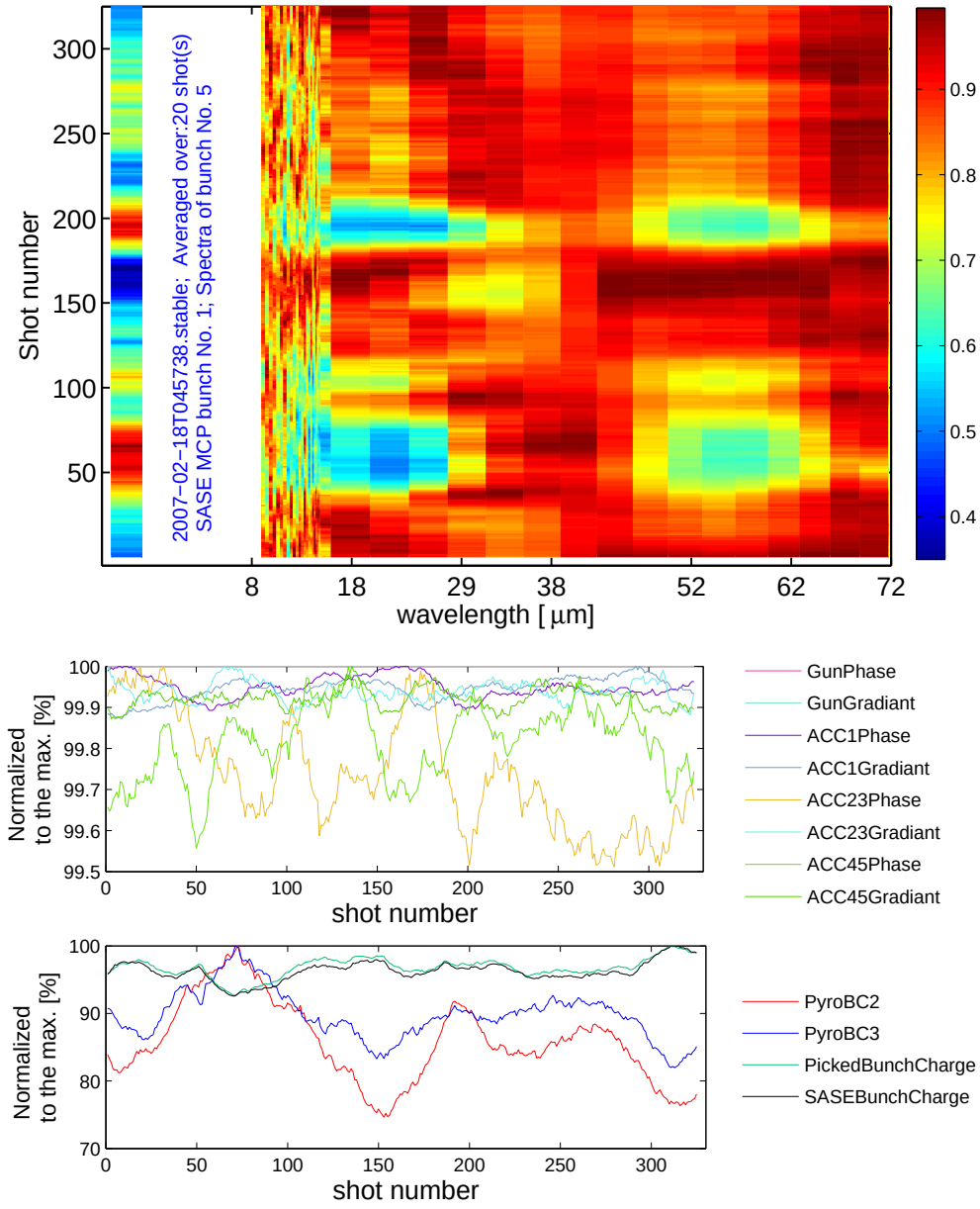

Figure 8.29: Density plot of the CTR spectra and SASE signal during stable operation of FLASH and the machine changes during the run. The SASE signal and the CTR spectral data (as well as data shown in the lower two plots) are averaged with a moving window in which the data points are averaged (smoothening the data) with a step size which is mentioned in the density plot which is in this analysis 20).

can be considered as vectors with the dimension equal to the number of shots. The angle between any of the spectral channels vectors, $\vec{S}$, and the SASE signal channel, $\vec{L}$, can be defined as[8]

$$\cos(\vec{S^c}\hat{,}\vec{L^c}) = \frac{\vec{S^c} \cdot \vec{L^c}}{\left|\vec{S^c}\right| \left|\vec{L^c}\right|}$$

where the superscript 'c' means the centered vector[9]. This gives a value between -1 and 1. Fully correlated and anti-correlated events correspond to 1 and -1, respectively.

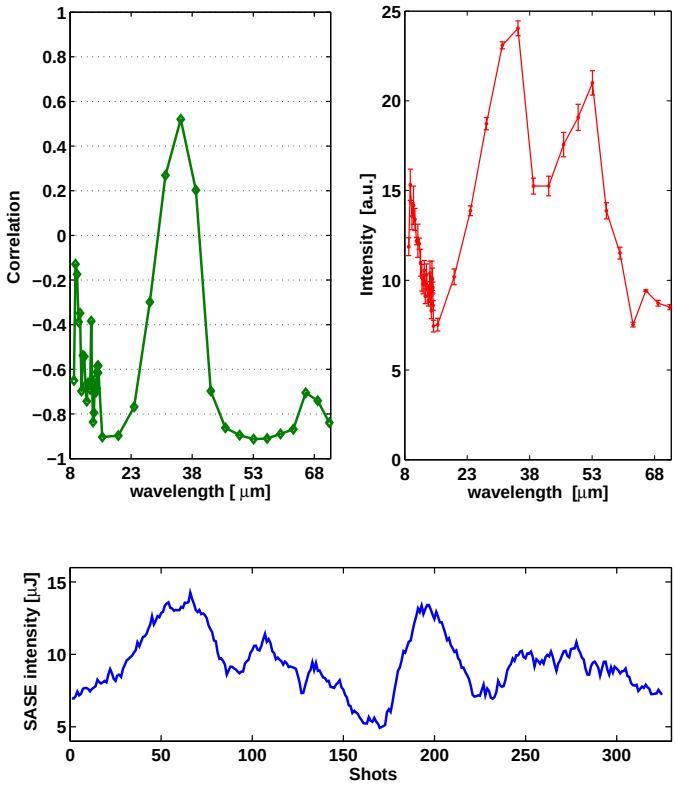

Figure 8.30: Top left: The correlation plot for Fig. 8.29. Top right: The average spectrum. Bottom: The absolute SASE energy during the run (SASE wavelength 28 nm).

[8]It can be shown that this is the same as the Pearson's product moment coefficient: $Corr(X,Y) = \frac{n\sum x_i y_i - \sum x_i \sum y_i}{\sqrt{n\sum x_i^2 - (\sum x_i)^2}\sqrt{n\sum y_i^2 - (\sum y_i)^2}}$

[9]A vector is centered if from each component of it the average value of all of its components is subtracted.

In Fig. 8.31 a second example of a stable run is shown. This time the kicked bunch for the CTR spectra and the SASE bunch are very close. The combination of the gratings has been changed as well. This makes a slight change in the coverage of the two stages of the spectrometer. The qualitative explanation is still valid but not as good as for the previous run.

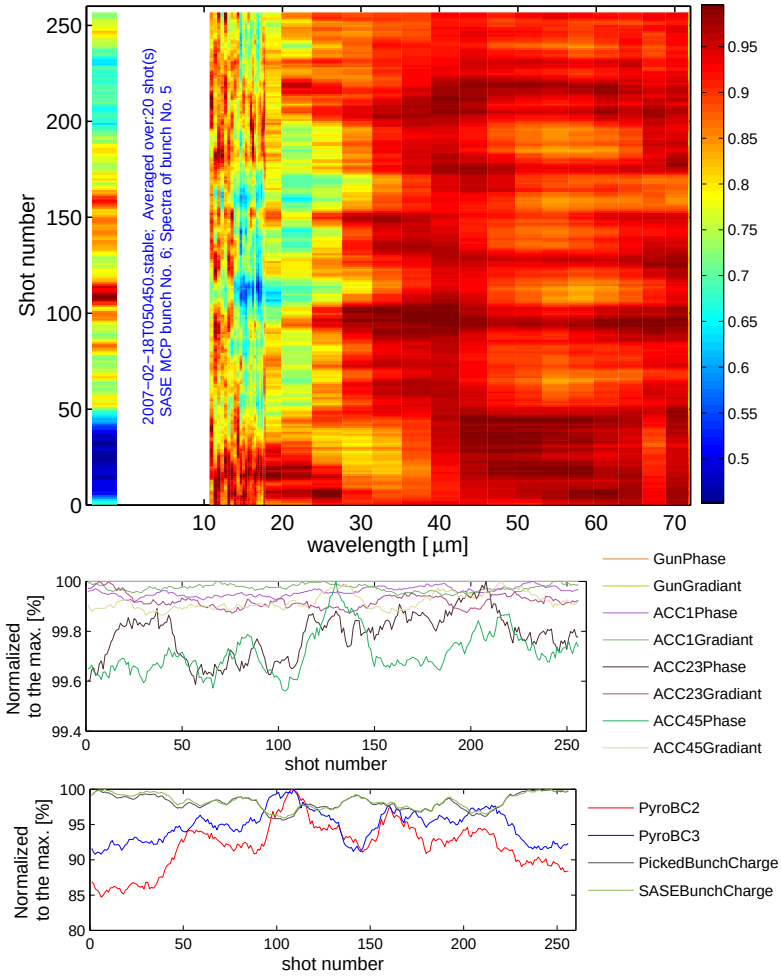

Figure 8.31: Density plot of the CTR spectra and the SASE signal during a stable run. The SASE signal and the CTR spectral data (as well as data shown in the lower two plots) are averaged with a moving window in which the data points are averaged (with a step size which is mentioned in the density plot which is in this analysis 20).

The quantitative correlation is also shown in Fig. 8.32. From the average spectra it is clear that the CTR spectra are more uniform and produce higher average SASE over the run according to the SASE signal data in lower part of the Fig. 8.32.

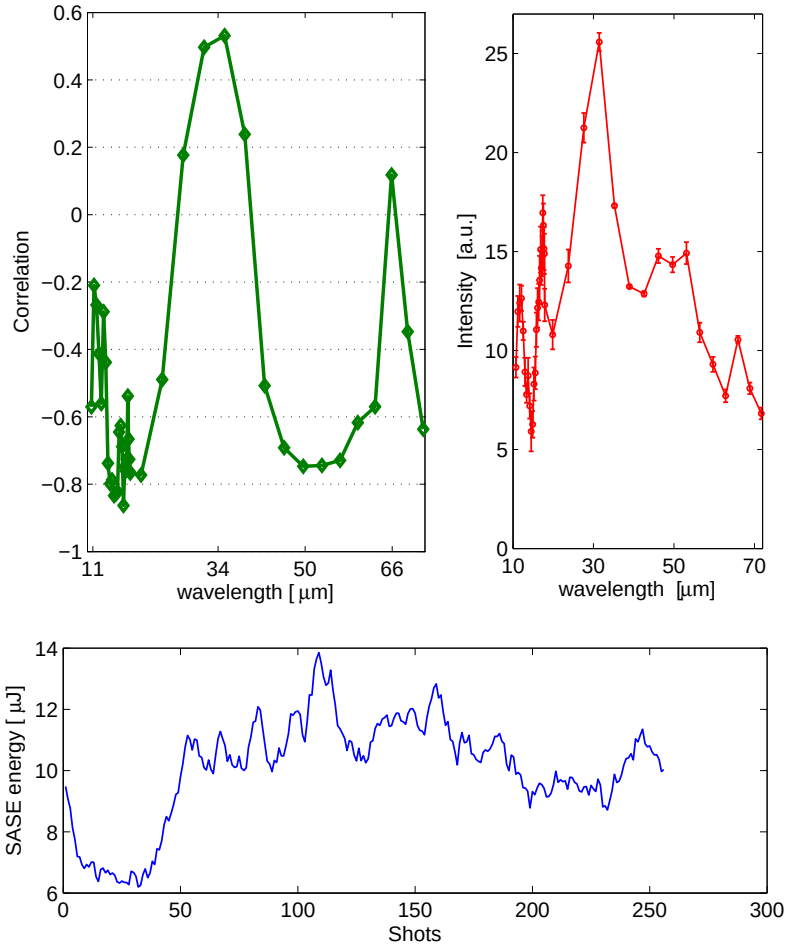

Figure 8.32: Top left: The correlation plot for Fig. 8.31. Top right: The average spectrum. Bottom: The absolute SASE energy during the run (SASE wavelength 28 nm).

Another run during the February 2007 accelerator study period is shown in Fig. 8.33. In this run a combination of the grating was chosen to cover longer wavelengths. The purpose of recording such a long wavelength range spectra was for the bunch profile determination. For the correlation studies, such a combination is not appropriate[10]. In this run after about 400 shots the longitudinal compression has increased. Accordingly, shorter wavelengths became stronger and at the same time SASE has vanished. For the shots after $\approx$ 400 in the wavelength range 26 to 41 μm, the spectral content in the wavelengths shorter than 26μm appear as the higher orders, therefore they correspond to wavelengths two or three times shorter.

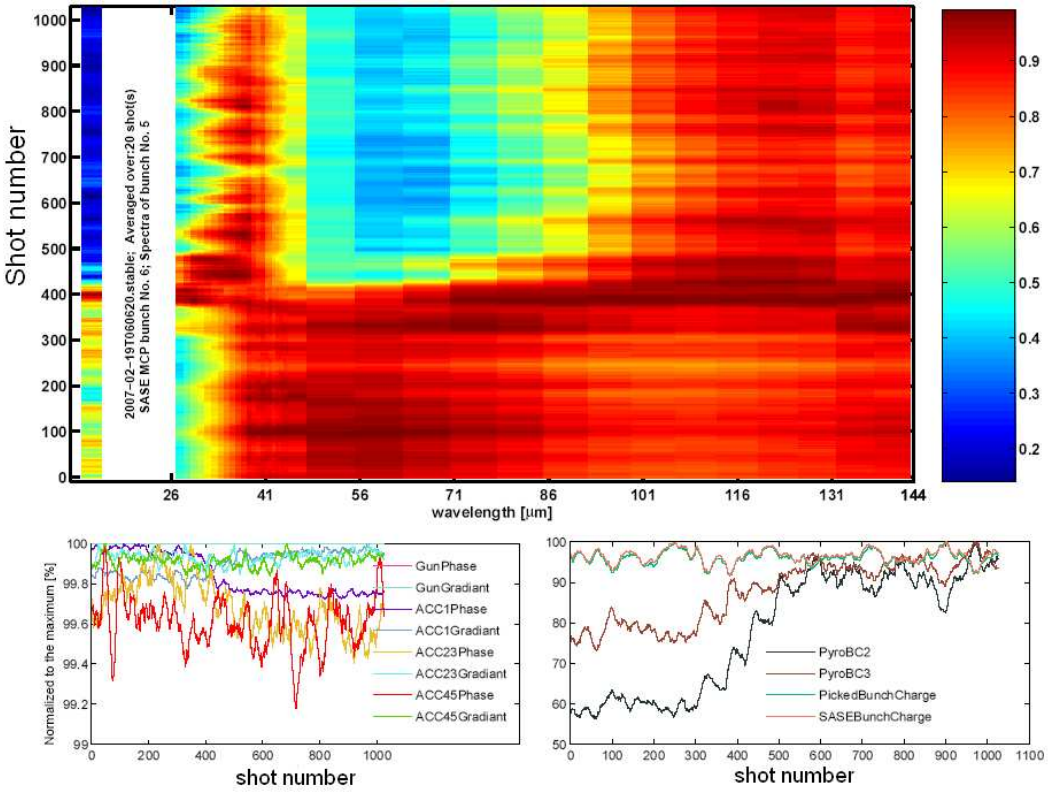

Figure 8.33: Density plot of the CTR spectra and the SASE signal for a run with unwanted sudden increase in the longitudinal compression. After about 400 shots ACC1 phase has changed by 0.2% and has not been corrected. This translated to a stronger compression that can be seen in PyroBC2 and PyroBC3 signals (for more details see text).

[10]Wavelengths shorter than 26 μm appear as the higher orders in the RBG unit. For the extraction of the spectrum, one can remove these higher orders by using a run that has data of shorter wavelengths. In this way an average spectrum can be obtained over a wide range.

Correlation to the SASE intensity using GMD

When FLASH is operated for SASE users, in parallel and parasitically, a bunch can be kicked onto the off-axis screen to record the CTR spectra. This gives the possibility to study the correlations and bunch profile when the SASE level is very high. In Fig. 8.34 the SASE pulse energy is shown which was measured with the GMD[11] and can be considered as one of the highest records achieved. As it can be seen in the picture, the 21st bunch was used to record the CTR spectra. The bar plots are made using the electron signals and the upper plots are made using the ion-signals. The meaning of the bar plot and the upper plot is the same as what was explained for the MCP-tool [63].

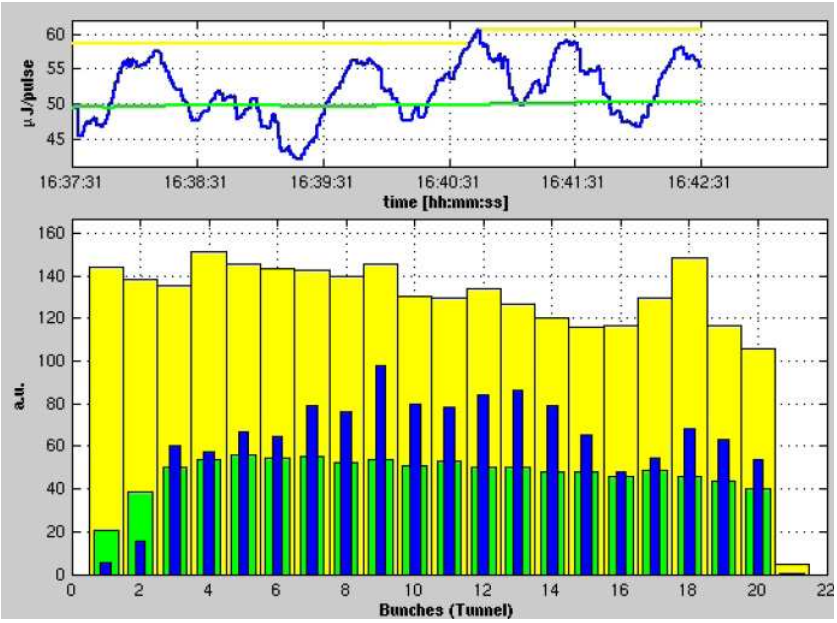

Figure 8.34: GMD-signal during a FLASH user run of a wavelength of 13.5 nm in March 2007. The 21st bunch is kicked onto the CTR140 screen to record the CTR spectra for this very high SASE intensity.

In Figures 8.35 and 8.36 the analysis of a sample run under these conditions is shown. The GMD has two detectors, Ion-detector and Electron-detector. The Electron signals, that are the faster signals, were not available during this run. The Ion-signals are slow and an averaging over a large number of shots (much larger than the values used with the MCP-detector read-out) is necessary to correlate them to the CTR spectral data. Doing such a strong data smoothening will raise an overall shift in the correlation plot, the reason why an integrated

[11] Gas Monitor Detector (see reference [64])

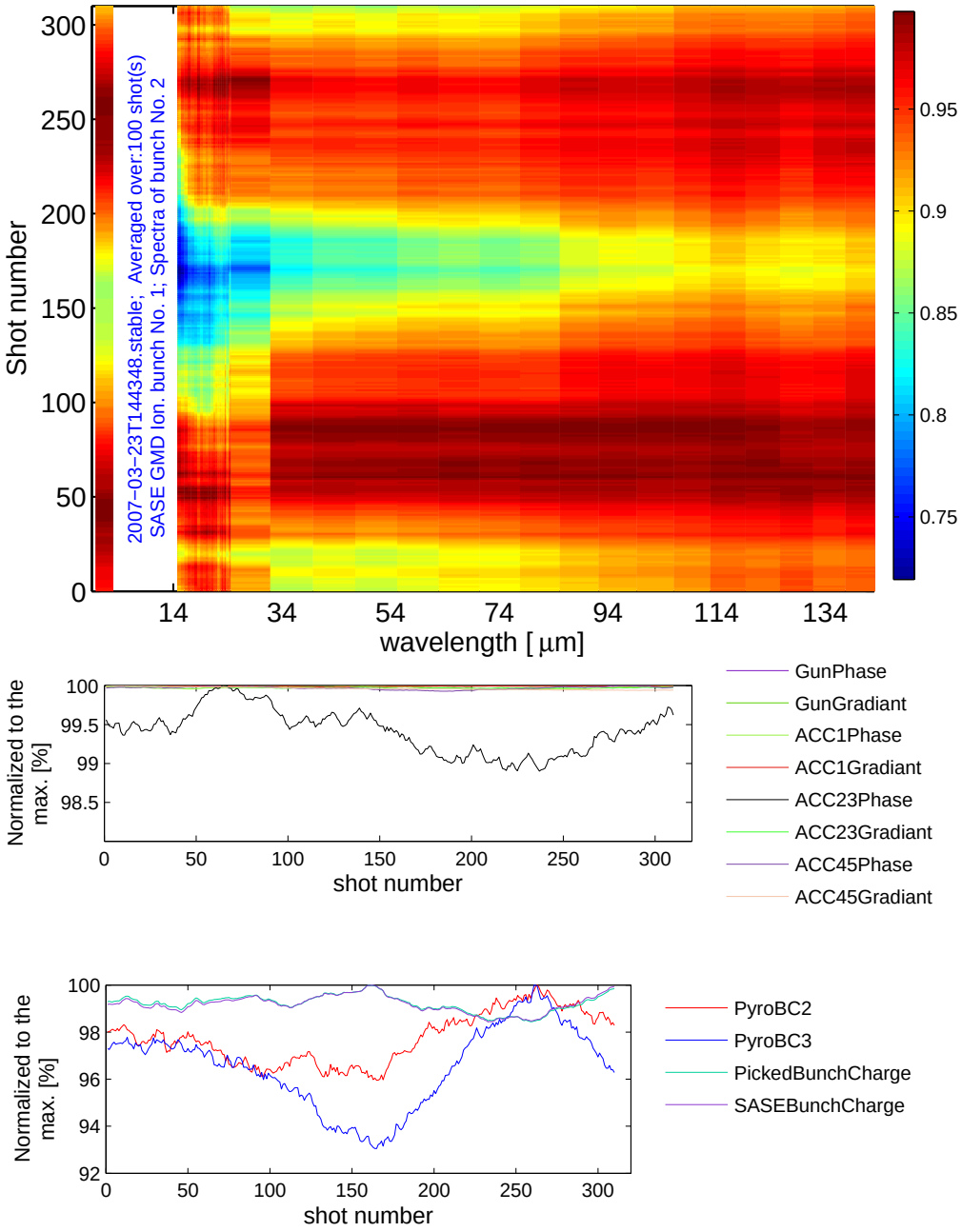

Figure 8.35: GMD-detector SASE signal and the CTR spectra. The SASE signal and the CTR spectral data (as well as data shown in the lower two plots) are averaged with a moving window in which the data points are averaged (with a step size which is mentioned in the density plot which is in this analysis 100).

signal can be used in a slow feedback compression control. The shift in the peak value of the most correlated wavelengths compared to those in Figures 8.30 and 8.32 can be related to the fact that during this run the accelerator was tuned for a SASE wavelength of 13.5 nm. Thus a different compression setting was used which could result in a different longitudinal profile.

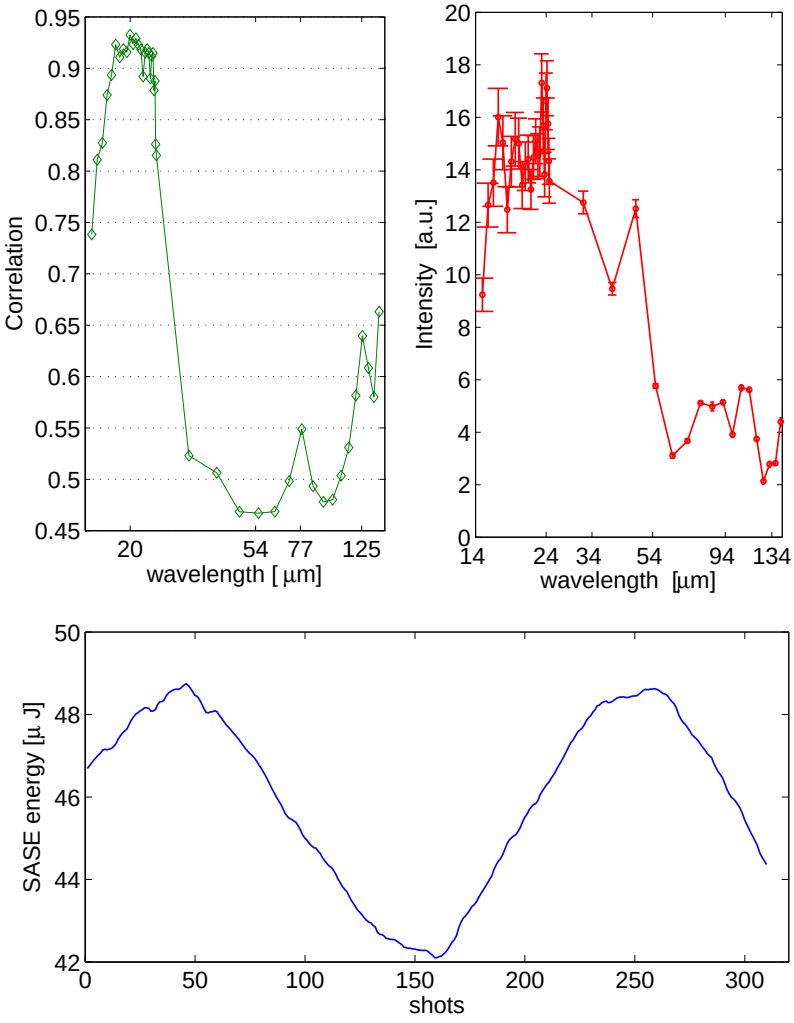

Figure 8.36: Top left: The correlation plot for Fig. 8.35. Top right: The average spectrum. Bottom: The absolute SASE energy during the run (SASE wavelength 13.5 nm).

Chapter 9

Bunch Profile Determination

The wavelength range coverage of the two-stage spectrometer is limited to about 2 octaves[1]. The measured average spectra can be combined to get the spectrum over a wider range. Such a combined spectrum represents the average CTR spectrum over a large number of shots and can be used to reconstruct the time domain profile.

9.1 The extraction of an ultra broad-band spectrum

Any bunch-profile measurement based on reconstruction of the time domain profile from a measured spectrum can give a more precise result as the measured spectral range becomes wider. The two-stage spectrometer can be used in several successive measurements that cover different spectral ranges and the measured average spectra can be combined. The range covered by the first stage of the spectrometer depends on the pitch size of the selected grating. Different gratings can be inserted to cover the entire wavelength range shorter than $\approx 40\ \mu\mathrm{m}$, the range that corresponds to the spike in the time-domain bunch-profile. The first stage of the spectrometer can resolve this range with high resolution. In the second stage of the spectrometer, dependent on the range that is covered by the first stage, a transmission grating can be chosen to disperse longer wavelengths. It is assumed that the intensities that are measured at the shortest wavelength range

[1] As a next development it is planned to construct compact stages which make it possible to setup four stages of the spectrometer in a vacuum chamber that is only one meter in diameter (see Fig. 6.13).

(with a grating of the pitch size $g_1 = g_{min}$) are free from higher order contributions. Starting from such a spectrum of the shortest measured wavelengths and using the efficiency calculations for the higher orders of the grating (see Fig. 4.3) that is used in the next range (covered by the first stage but in another measurement with a grating of the pitch size $g_2 > g_1$), it is possible to calculate the contribution of the higher orders that are not filtered. In Fig. 9.1 the result of such a calculation is shown[2].

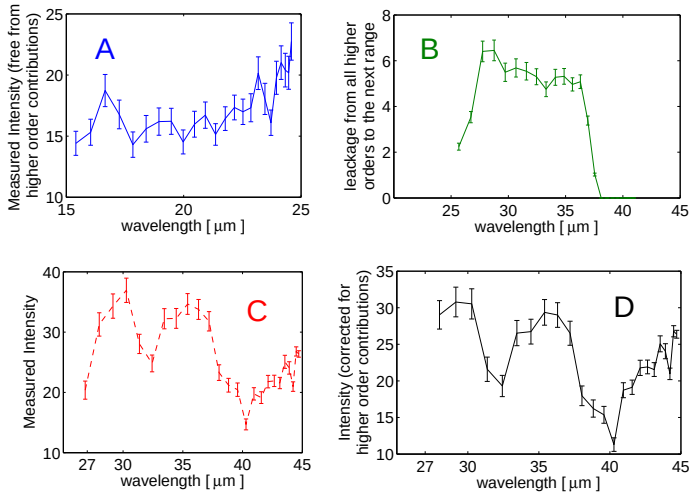

Figure 9.1: Correction of higher order contributions from a measured spectrum. A: A spectrum which is free from higher order contributions, measured with a grating with a pitch size of $g_1 = 20\ \mu m$. B: Contributions from the spectrum in 'A' if it illuminates a grating with a larger pitch size of $g_2 = 35\ \mu m$. C: The measured CTR spectrum using a grating with a pitch size of $g_2 = 35\ \mu m$ before correction for contributions from shorter wavelengths. D: Spectrum 'C' corrected by spectrum 'B'.

The spectrum that is shown in Fig. 9.1.A has been measured with a grating of pitch size $g_1 = 20\ \mu m$. Without loss of generality it can be assumed that this spectrum is free from higher order contributions. When exchanging the grating with one of pitch size $g_2 = 35\ \mu m$, the short wavelength spectrum of 'A' will show up as higher orders mixed with a first order spectrum. Using the theoretical expectations for the higher order efficiencies, the contribution from short wave-

[2]When unfolding these contributions from the measured signal in the next range the relative detector response has to be taken into account.

lengths like in 'A' when illuminating a grating with larger pitch size of $g_2 = 35\ \mu m$ can be calculated as 'B' in Fig. 9.1. In 'C' a measured spectrum is shown in which the incoming CTR illuminated a grating with a pitch size of $g_2 = 35\ \mu m$ without any preceding filter grating. Therefore a contribution like in 'B' can be subtracted from 'C' to obtain the spectrum that is shown in 'D'.
The range that is unfolded from the higher order contributions can be used in a similar way on the next longer wavelengths range. This process can be repeated until the entire spectrum becomes free from higher orders. Then the absolute detector response can be used to get the spectrum in absolute units of energy per bandwidth. The obtained spectrum can be corrected for the transfer function of the beamline plus diamond window and transmission of the polarizer. The result of application of this process to the March 2007 measurements is shown in Fig. 9.2. The error bars are calculated in terms of the standard deviation of the signals over the run and no further possible systematic errors like uncertainties on the detector response or other sources are considered.

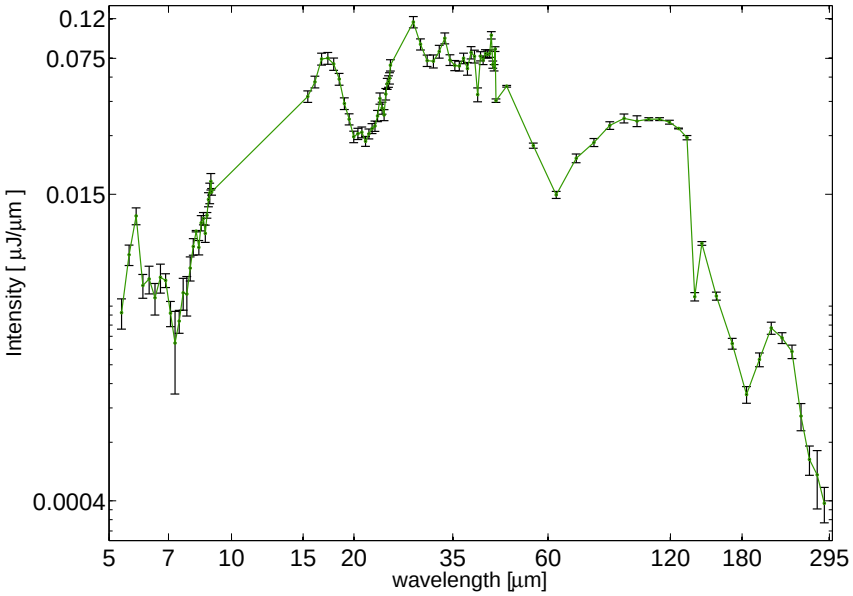

Figure 9.2: Combined spectrum of March 2007 measurement.

The TR single electron intensity emitted into the frequency band $d\omega$, as is described in chapter 3, shows a flat spectrum over the range of frequencies larger than $\approx 1\ THz$. Therefore, factorizing the $\frac{1}{\lambda^2}$ dependence, a wavelength domain spectrum like in Fig. 9.2 is proportional to the form factor squared (see Eq. 3.3).

9.2 The time profile reconstruction method

The form factor that is defined by Eq. 3.1 is a complex value function. From a measured coherent radiation spectrum only the magnitude of the form factor can be extracted directly. In order to reverse the Fourier transformation and obtain the time domain profile, phases are needed. An ordinary method is to use a Kramers-Kronig relation for phase reconstruction. In this method extrapolations on both shorter and longer wavelengths limits of the measured spectrum can be used to obtain a spectrum that extends over all wavelengths. Then this extended spectrum can be used to get a minimal phase that gives a most likely time profile [25]. In the following a more intuitive method based on the extraction of the bunch profile by making a fit to the measured spectrum is described. Gaussian profiles of different standard deviations ($\sigma_{\mathtt{i}}$) with different weights ($\mathtt{A_i}$) that peak at different times ($\mathtt{t_i}$) can be considered as the building blocks of the fit

$$g_i(t) = \frac{A_i}{\sqrt{2\pi}\sigma_i} \exp\left(-\frac{(t-t_i)^2}{2\sigma_i^2}\right) \tag{9.1}$$

A superposition of such profiles can be written as

$$T(t) = \sum_i g_i(t) \tag{9.2}$$

where $g_i(t)$ is given by Eq. 9.1. The frequency domain conversion of T(t) can be written as

$$\Omega(\omega) = \sum_i G_i(\omega)$$

where

$$G_i(\omega) = A_i \exp(-\frac{\omega^2\sigma_i^2}{2}) \exp(-i\omega t_i)$$

$\Omega(\omega)$ is proportional to the form factor[3]. The wavelength domain intensity spectrum can be written as (for wavelengths shorter than $\approx \mathtt{300}\ \mu\mathtt{m}$ where the single electron spectrum is roughly a constant multiplied by $\frac{1}{\lambda^2}$)

$$U(\lambda) \propto \frac{2\pi c}{\lambda^2} \left|\Omega(\frac{2\pi c}{\lambda})\right|^2 \tag{9.3}$$

where c is the speed of light. With $\sigma_{\mathtt{i}}$ and $\mathtt{t_i}$ in femtoseconds and λ in micrometers, $\mathtt{c} = \mathtt{0.2996}\ \frac{\mu\mathtt{m}}{\mathtt{fs}}$. For the fit method the "fminsearch" command of MATLAB

[3]With Eq. 9.2 normalized to the total bunch charge $\Omega(\omega)$ would give the form factor.

is used which is based on the Nelder-Mead [65] simplex algorithm[4] and it finds a local minimum of a scalar function of several variables, starting with an initial estimate. The rate of the convergence and the fit itself (which is the local minimum closest to the initial) is highly dependent on the initial starting profile. The developed code for the bunch profile determination works in the following way. A measured spectrum can be loaded and then as a starting point a reasonable initial can be introduced. The initial profile is based on the superposition of up to eight Gaussian profiles like Eq. 9.1. The variation of the initial as a function of the parameters ($\mathtt{A_i s}$, $\sigma_\mathtt{i s}$ and $\mathtt{t_i s}$) can be seen in comparison with the measured spectrum in a combined plot (like Fig. 9.3). When the initial is enough close to the spectrum, the fit routine can be started to find a possible fit. With appropriate values for the fit parameters a wavelength-domain spectrum can be found that is proportional to a measured spectrum (see Eq. 3.3).

It is possible to start with a well defined time domain profile, for instance a

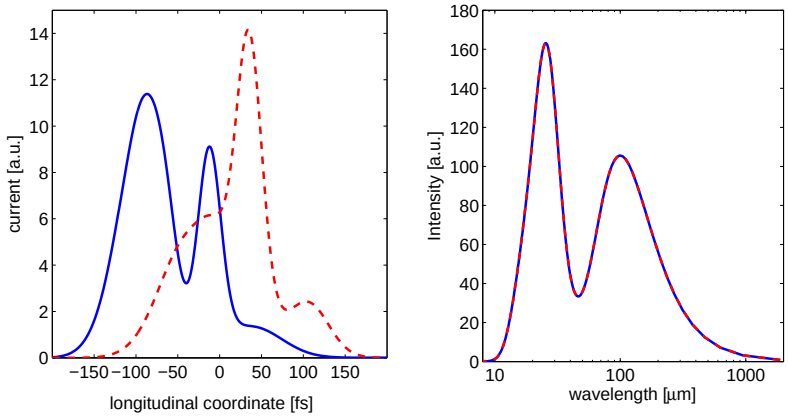

Figure 9.3: An example of two time domain profiles that fit to the same spectrum. The values of Gaussian components like Eq. 9.1 that result in these fits are given in table 9.1.

superposition of eight Gaussian profiles as is described in Eq. 9.1, and calculate the form factor. Then this wavelength domain form factor can be used in a reconstruction process. The fact that the Gaussian profiles are not orthogonal functions makes it possible to have different expansions in terms of this set of

[4]This simplex search method is a direct search method that does not use numerical or analytical gradients. At each step of the search, a new point in or near the current simplex is generated. The function value at the new point is compared with the function values at the vertices of the simplex and, usually, one of the vertices is replaced by the new point, giving a new simplex. This step is repeated until the diameter of the simplex is less than the specified tolerance [66].

functions for an arbitrary time profile. In other words, it can be seen that a time domain fit like Eq. 9.2 to a measured form factor is not unique but this does not necessarily mean that the time domain profile that fits to a measured spectrum is degenerate. An example is shown in Fig. 9.3 with the values as are listed in table 9.1. For a wavelength spectrum and its time domain profile like the dashed-red curves in Fig. 9.3 there is another fit like the solid-blue curves. Within the precision that can be achieved experimentally, the two spectra are identical and therefore the two time profiles are indistinguishable. There is no physical argument to identify a fit that is more likely than the other.

Table 9.1: The values of the parameters used for the fits of Fig. 9.3

	i	1	2	3	4	5	6	7	8
fit1	σ_i (fs)	20	15	20	25	30	32	35	30
	t_i (fs)	0	35	50	105	-30	-40	-50	-60
	A_i	150	450	75	150	150	150	75	37.5
fit2	σ_i (fs)	16.36	14.9	33.9	46.23	30	26.4	22.3	13.6
	t_i (fs)	67.75	90.4	-46.3	18.2	-39.2	121	101	12.2
	A_i	239	98	75	80	12.9	130.5	326	278.4

The fact that for a measured spectrum there are always errors in the intensity level increases the number of possible fits. The results of two fits to the spectrum of Fig. 9.2 are shown by the blue and red curves in Fig. 9.4. The corresponding time domain profiles are shown with the same color in the lower plot. In table 9.2 the parameters that are used for the two fits of Fig. 9.4 are given.

Table 9.2: The values of the parameters used for the fits of Fig. 9.4

	i	1	2	3	4	5	6	7	8
fit1 (blue)	σ_i (fs)	83.25	6.73	16.86	80	17.08	6.28	15.63	25.38
	t_i (fs)	-74.6	321.7	200.3	0	225.3	282.8	113.2	2.8
	A_i	9.25	0.78	2.3	0.323	10.65	1.98	2.235	0.379
fit2 (red)	σ_i (fs)	5.65	17	10.1	21.7	20.4	16	26	5.52
	t_i (fs)	105	203	81	209	110	268.7	130.6	93.4
	A_i	1.67	2.01	1.48	1.58	4.07	1.25	4.53	2.71

In Figures 9.5 and 9.6 the same time-domain profile reconstruction method is applied to the measurements of Figures 8.29 and 8.31, respectively. The numerical

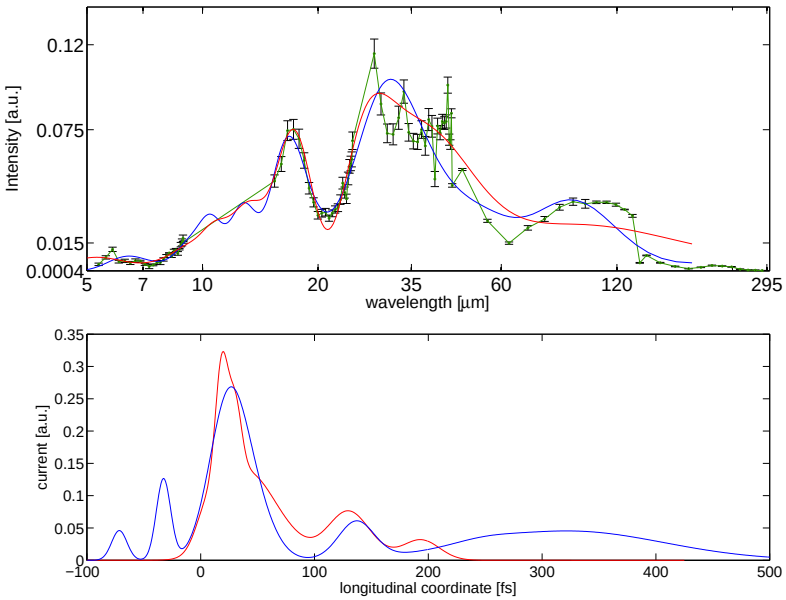

Figure 9.4: Combined spectrum of March 2007 measurement with two possible time domain profiles that their wavelength spectra fit to the measured spectrum.

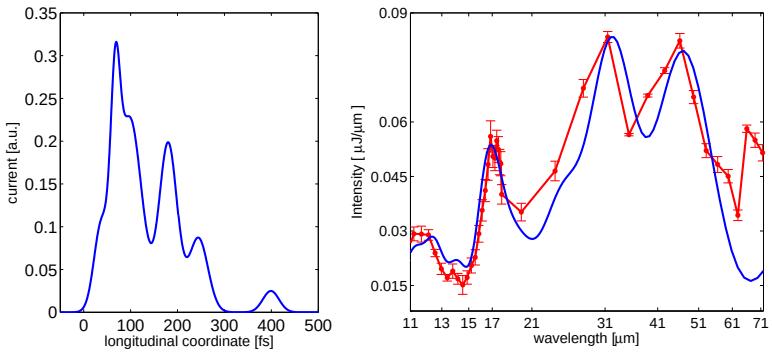

Figure 9.5: Average spectrum and a corresponding time domain profile for measurement of Fig. 8.29. This spectrum is not a combination of spectra of successive measurements and therefore covers a limited spectral range in comparison to Fig. 9.4. The possible contribution from wavelengths shorter than 11 μm are not corrected here. Thus showing several fits does not give any further insight into the time domain profile.

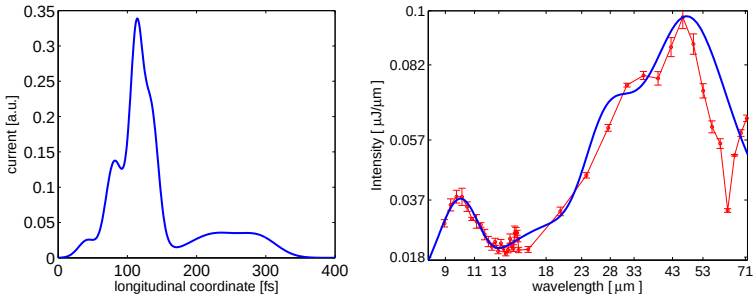

Figure 9.6: Average spectrum and a corresponding time domain profile for measurement of Fig. 8.31. This spectrum is not a combination of spectra of successive measurements and therefore covers a limited spectral range in comparison to Fig. 9.4. The possible contribution from wavelengths shorter than 8 μm are not corrected here. Thus showing several fits does not give any further insight into the time domain profile.

Table 9.3: The values of the parameters used for the fits of Figures 9.5 and 9.6.

	i	1	2	3	4	5	6	7	8
	σ_i (fs)	9.8	33.1	20.2	19.06	15.6	17.2	24.6	–
fit	t_i (fs)	-112.5	-80.1	64.6	0.55	-143	219.4	-81.9	–
Fig. 9.5	A_i	4.6	3.52	4.4	9.34	3.6	1.08	11.4	–
	σ_i (fs)	13.04	38.8	9.85	10.8	11.1	26.07	20.2	8.5
fit	t_i (fs)	-12.29	-197.07	-105	-54.4	-48.2	-261.9	-85.9	-83.1
Fig. 9.6	A_i	0.82	3.33	3.4	0.51	2.67	1.55	5.8	4.46

values of the fit parameters are given in table 9.3. The average SASE intensities produced during these runs are shown in Figures 8.30 and 8.32, respectively. They show an average SASE intensity of about $\approx 10\ \mu J$ for 28 nm wavelength which is much less than $\approx 45\ \mu J$ average SASE signal, in 13.5 nm wavelength, of Fig. 8.36 that corresponds to the spectrum and bunch profile of Fig. 9.4. It is unlikely to be able to explain the difference in the SASE intensity level in these measurements in terms of the reconstructed longitudinal profiles of Figures 9.4, 9.5 and 9.6. The possible reason is the tunings of the machine that usually is performed downstream of CTR140 screen. As it was mentioned before, the measurements that resulted in the spectrum of Fig. 9.4 are made parasitically in parallel to a user operation with a very high SASE level while the other two measurements (Figures 9.5 and 9.6) are made during a machine study period with an intermediate SASE level and much less efforts made to achieve high level SASE intensity.

In order to conclude this section a few remarks can be made. According to the arguments of this section, any bunch profile reconstruction from a measured spectrum, taking into account the presence of systematic errors, cannot result in a unique (or a most likely) result. Nevertheless a measured spectrum can be used to tune the accelerator. Intensities in different spectral ranges can be used in a feedback loop to keep/tune, for instance, RF parameters of the accelerating modules to achieve an optimal longitudinal compression. Further study has to be made to use the information about the longitudinal bunch profile which are encoded in the coherent radiation of the electron bunches.

Chapter 10

Summary and Outlook

Summary

For an FEL based on the SASE principle, electron bunches with a high peak current in the kA range over at least one coherence length (which is related to the FEL wavelength) is required. Due to the space charge repulsive forces the realization of such a high peak current is not possible before electrons are accelerated to ultra-relativistic energies. When electrons are ultra-relativistic a magnetic-chicane bunch compressor can be used to convert a correlated energy chirp, introduced by the sinusoidal accelerating field, into a longitudinal compression. Such a compressed electron bunch has a spike with high peak current and a long tail. Diagnostics of the spike in the electron bunch profile is very crucial for the operation and stabilization of the accelerator that drives the high-gain SASE-FEL. One of the important parameters that has to be monitored is the longitudinal bunch profile. Operation of accelerators like the linac of FLASH shows that the shot to shot changes in the longitudinal bunch profile is not necessarily small, requiring a single-shot longitudinal diagnostics. One way for the longitudinal bunch profile diagnostics is to measure the coherent radiation that an electron bunch emits when it is subjected to a radiation process such as transition radiation.

It has been shown that a transition radiation source can provide information on short structures in the bunch profile that correspond to the coherence length and shorter.

Following theoretical investigations on different approaches to build up a spectrometer, a grating spectrometer has been found to be very advantageous in many respects. The result of the theoretical investigations that resulted in an optimized grooves geometry for a reflectance-grating spectrometer setup is demonstrated.

Experimental proof-of-principle measurements on the theoretical calculations for the grating setup are presented. The optimization of the setup was carried out to achieve very high dispersion efficiency of the gratings over a wide range in each stage and at the same time sustain a very high efficiency of the zero-order for the longer wavelengths. A layout to stage several units to enlarge the wavelength range coverage of the spectrometer has been designed.
It has been demonstrated that room temperature detectors can be used in the detection unit of the spectrometer even though the coherent radiation is dispersed into its components and the sorted intensities are much less than the integrated intensity that usually can be measured by the detection system of the classical bunch compression monitors.
A scanning mode grating spectrometer has been designed and tested. This spectrometer has been used in further developments towards the realization of the broad-band single-shot spectrometer.
Prototypes of the single-shot spectrometer were designed and mounted and a variety of experiments including the first studies on the correlation of the spectral changes in the emitted coherent radiation of the electron bunches and the SASE intensity has been carried out.
Finally a rather compact two-stage single-shot spectrometer based on an integrated collecting optics and detectors has been designed, mounted and used in several series of measurements that are demonstrated in this thesis.
The correlation studies show different wavelength ranges of the Coherent Transition Radiation (CTR) spectra that correlate or anti-correlate to the SASE intensity. Dependent on the parameters that are used to tune the longitudinal compression of the electron bunches (to tune for a desired SASE-FEL wavelength), the CTR wavelength range that correlates or anti-correlates to the SASE intensity was found to be different. For example, for a set of parameters that provide 20 μJ single-pulse SASE intensity at a wavelength of 28 nm the range from 25 to 40 μm in the CTR spectra correlates to the SASE intensity while the shorter wavelengths of 15 to 20 μm show a strong anti-correlation. In another run where the accelerator was tuned for 13.5 nm SASE wavelength, the strongest correlations showed up in the 15 to 25 μm wavelength range.
The limited space of the vacuum tank at the CTR140 beamline plus the relatively big size of the first design of the integrated collecting and detection systems did not allow to mount more than two stages of the single-shot spectrometer, thus the wavelength coverage in the single-shot mode was limited to about two octaves. A wider spectrum was derived only in an average sense by combining the average spectra that were measured in series by inserting gratings with different pitch sizes. The effect of the higher orders which were present in the first stage of the

two-stage spectrometer were always removed from the measured spectra (the lack of space did not allow to follow the proposed layout to start with the first grating to resolve the shortest wavelengths which were present in the coherent radiation spectra and still catch the range of interest towards longer wavelengths).
For the bunch profile determination from a measured broad-band spectrum a fit method has been developed and used. It has been shown that the time domain fit to an experimental data is not unique. In the presence of un-avoidable systematic errors the number of possible fits to a measured spectrum increases. Although the presence of the short structures can be studied, a bunch profile reconstruction is not feasible due to the missing phase information. It has been generally shown that this is an intrinsic problem with a wavelength-domain measurement that measures only the intensities, and not the phases, therefore cannot result even in a most-likely bunch profile. An example is given which shows that no reconstruction method can overcome this intrinsic problem. The attempt to reconstruct the bunch time profile is probably not the most appropriate way of extracting the useful information contained in the spectra.

Outlook

There are several areas that are not covered by this thesis and could improve the device. Detector calibration has to be continued, in particular, for the short wavelengths below 35 μm. Transmission gratings are not studied in terms of an experimental evaluation of different order efficiencies. An experiment similar to those which have been done for the reflectance grating has to be performed. After having good experimental knowledge on these calibrations the entire spectrometer has to be calibrated to obtain a measured transfer function of the entire device. In a later step systematic errors have to be studied as well.
The ongoing efforts to setup a multi-stage device composed of more compact detection units could provide a wider wavelength range coverage in a single-shot mode. It is planned to have two gratings on each of the four grating holders in each stage to keep the possibility to cover different parts of the spectra (about four octaves with each combination of the gratings).
It is obvious that the spectrally resolved single-shot measurement of the coherent radiation could help to tune the longitudinal compression of the electron bunches. Advanced bunch compression monitors can be used in different parts of an accelerator where the electron bunches undergo longitudinal profile changes. For feedback purposes a dedicated study can help finding how to use the information encoded in the measured online spectra to tune different parameters of the accelerator.

Installation of the described single-shot spectrometer in different parts of an accelerator such as FLASH (for instance at the dipoles of the magnetic chicanes, where the coherent synchrotron radiation is emitted anyhow) could help to carry on correlation studies in a more dedicated way with much larger rate of data acquisition. In particular at FLASH, a CTR-screen coupled to a short THz beamline inside the tunnel, after all undulators, could provide a source of CTR containing information about all fine structures including microbunching. Such an installation provides a source that is theoretically well predictable over a wide range of far-infrared down to the visible wavelengths.

Appendix A

Vector Diffraction Theory for Gratings

A.1 Perfectly conducting grating

The physical problem of diffraction grating has been described in section 4.1. In the following the notation of section 4.1 and Fig. 4.1 is used. For a perfectly conducting $\mathtt{R}_-$, the electromagnetic field vanishes in this region[1]. The diffracted fields are defined in region $\mathtt{R}_+$ by $\vec{E}^d = \vec{E} - \vec{E}^i$ and $\vec{H}^d = \vec{H} - \vec{H}^i$.

Maxwell equations in free space are given by

$$\begin{aligned} \nabla \times \vec{E}^d &= i\omega\mu_0 \vec{H}^d & \nabla \times \vec{H}^d &= -i\omega\epsilon_0 \vec{E}^d \\ \nabla \cdot \vec{E}^d &= 0 & \nabla \cdot \vec{H}^d &= 0 \end{aligned}$$

Introducing the components of the diffracted fields on the three axes, the following equations can be derived:

$$\begin{aligned} \partial_y E_z^d &= i\omega\mu_0 H_x^d & \partial_y H_z^d &= -i\omega\epsilon_0 E_x^d \\ \partial_x E_z^d &= -i\omega\mu_0 H_y^d & \partial_x H_z^d &= i\omega\epsilon_0 E_y^d \\ \partial_x E_y^d - \partial_y E_x^d &= i\omega\mu_0 H_z^d & \partial_x H_y^d - \partial_y H_x^d &= -i\omega\epsilon_0 E_z^d \end{aligned} \tag{A.1}$$

and for the boundary conditions for the fields on the grating surface:

$$\widehat{\mathcal{N}} \times (\vec{E}^d + \vec{E}^i) = \vec{0} \qquad \widehat{\mathcal{N}} \cdot (\vec{H}^d + \vec{H}^i) = 0$$

[1] There are experimental evidences [67] that the model of perfectly conducting gratings fails in the visible and near infrared despite the reflectivity of aluminum, silver or gold exceed 90 percent.

Here $\widehat{\mathcal{N}}$ is the unit vector in the direction normal to the grating surface and is pointing to the region $\mathtt{R}_+$. It suffices to write the first equation as:

$$E_z^d = -E_z^i \qquad\qquad \mathcal{N}_x E_y^d - \mathcal{N}_y E_x^d = -(\mathcal{N}_x E_y^i - \mathcal{N}_y E_x^i)$$

Regrouping Eq. A.1 for TE and TM modes, will result in two sets of differential equation systems. For TE mode

$$\partial_y E_z^d = i\omega\mu_0 H_x^d \qquad \partial_x E_z^d = -i\omega\mu_0 H_y^d \qquad \partial_x H_y^d - \partial_y H_x^d = -i\omega\epsilon_0 E_z^d$$

with boundary condition $E_z^d = -E_z^i$. For TM mode:

$$\partial_y H_z^d = -i\omega\mu_0 E_x^d \qquad \partial_x H_z^d = i\omega\mu_0 E_y^d \qquad \partial_x E_y^d - \partial_y E_x^d = i\omega\mu_0 H_z^d$$

with boundary condition[2] $\frac{\mathtt{d}}{\mathtt{d}\mathcal{N}}\mathtt{H_z^d} = -\frac{\mathtt{d}}{\mathtt{d}\mathcal{N}}\mathtt{H_z^i}$.
These two sets of equations can be written as Helmholtz differential equation for the magnitude of the fields, F, as:

$$\nabla^2 F^+ + k^2 F^+ = 0 \tag{A.2}$$

with boundary conditions on the surface of the grating:

$$\begin{cases} F^+ = -F^i = -\exp[ikx\sin\theta - ikf(x)\cos\theta] & TE\ mode \\ \frac{d}{d\mathcal{N}}F^+ = -\frac{d}{d\mathcal{N}}F^i = i(k\mathcal{N}_y\cos\theta - k\mathcal{N}_x\sin\theta)\exp[ikx\sin\theta - ikf(x)\cos\theta] & TM^3\ mode \end{cases} \tag{A.3}$$

and $\mathtt{F}^+$ satisfies a radiation condition[4] when $\mathtt{y} \to \infty$.

A.1.1 The Rayleigh expansion above the grooves

It can be shown that $\mathtt{F}^+(\mathtt{x},\mathtt{y})$ is a periodic function with the period of groove spacing, g, or in other words the period of the function f(x) (see [34]). $\mathtt{F}^+(\mathtt{x},\mathtt{y})$ can be expanded in Fourier series as:

[2] $\frac{\mathtt{d}}{\mathtt{d}\mathcal{N}}$ is the directional derivative in the direction of $\widehat{\mathcal{N}}$ or $\frac{\mathtt{d}}{\mathtt{d}\mathcal{N}} = \widehat{\mathcal{N}}\cdot\nabla$

[3] TM mode (S-polarization) is when the electric field is perpendicular to the grooves and TE mode (P-polarization) is when the electric field is parallel to the grooves.

[4] The integrated power over a large enough surface that surrounds the entire volume under consideration is finite.

$$F^+(x,y) = \sum t_n(y) \exp(i\alpha_n x) \tag{A.4}$$

with $\alpha_n = k \sin\theta + nK$ where $K = \frac{2\pi}{g}$.
Substituting Eq. A.4 into Eq. A.2 results in a differential equation for t_n

$$\frac{d^2 t_n}{dy^2} + (k^2 - \alpha_n^2) t_n = 0 \qquad above\ \ the\ \ grooves \tag{A.5}$$

With the definition:

$$\beta_n = \begin{cases} (k^2 - \alpha_n^2)^{1/2} & if\ k^2 > \alpha_n^2 \\ i(\alpha_n^2 - k^2)^{1/2} & otherwise \end{cases}$$

the general solution can be written in the form:

$$t_n = A_n \exp(-i\beta_n y) + B_n \exp(+i\beta_n y) \quad above\ \ the\ \ grooves \tag{A.6}$$

The first term with coefficient A_n becomes infinite when $y \to \infty$ if $k^2 < \alpha_n^2$, or it represent incoming plane wave propagating toward the grating surface if $k^2 > \alpha_n^2$. Thus

$$F^+(x,y) = \sum B_n \exp[i(\alpha_n x + \beta_n y)] \qquad above\ \ the\ \ grooves \tag{A.7}$$

Introducing θ_n as the angle of wave-vector $k_n = (\alpha_n, \beta_n)$ (Fig. 4.1) one can derive:

$$\sin\theta_n = \frac{\alpha_n}{(\alpha_n^2 + \beta_n^2)^{1/2}} = \frac{\alpha_n}{k}$$

or after substitution from $\alpha_n = ksin\theta + nK$ the grating equation[5] results:

$$\sin\theta_n = \sin\theta + n\frac{\lambda}{g} \tag{A.8}$$

[5]The sign convention for direction of angles could be considered differently and then this may result in a minus sign difference with Eq. 4.3.

A.1.2 Efficiencies of different orders

It can be seen that $\mathcal{E}_n$ (defined in section 4.2.2) is related to the B_n by [34]:

$$\mathcal{E}_n = B_n \bar{B}_n \cos\theta_n / \cos\theta \tag{A.9}$$

where $\bar{B}_n$ is the complex conjugate of B_n. The efficiencies obey the energy balance criterion $\sum \mathcal{E}_n = 1$ and B_n is given by the integral equations (for detailed derivation see [34]):

for TM case

$$B_n = \frac{1}{2ig\beta_n} \int_0^g \exp[-i(\alpha_n x + \beta_n f(x))]\phi(x)dx \tag{A.10}$$

where $\phi(x) = (1 + f'^2(x))^{1/2} \frac{d}{d\mathcal{N}}(F^+ + F^i)$, and for TE case

$$B_n = \frac{1}{2g} \int_0^g (1 - \frac{\alpha_n}{\beta_n} f'(x)) \exp[-i(\alpha_n x + \beta_n f(x))\Psi(x)dx] \tag{A.11}$$

where $\Psi(x) = F^+(x, f(x)) + F^i(x, f(x))$ and $\mathtt{F}^+$ is given by Eq. A.7.
These are the integral equations to be solved for complete solution of the grating problem. Fortunately there are several different methods to calculate B_n coefficients described for instance in [34].
There are many techniques developed more recently to calculate efficiencies for instance in [61] which is a method based on a theorem of analyticity of the electromagnetic field with respect to variations of the interface for perfectly conducting gratings[6].

A.1.3 A numerical method for efficiency calculation for perfectly conducting grating material

In this part a numerical method to solve Eq. A.11 or in other words, efficiency calculation for P polarization, is described. Similar method can be used to solve Eq. A.10 of the S polarization. Define an internal product on $C^{(1)}([0, g])$ as

$$\langle k(x)|l(x)\rangle = \frac{1}{2g} \int_0^g k(x)l(x)dx$$

Following definitions are used in the forthcoming algorithm

[6] Therefore applicable to infrared range.

$$h_n(x) = 1 - \frac{\alpha_n}{\beta_n} f'(x) \qquad \phi_n(x) = \exp(i\alpha_n x + i\beta_n f(x))$$

Then Eq. A.11 can be written as

$$B_n = \langle h_n(x)\phi_n^*(x)|F^i(x, f(x))\rangle + \langle h_n(x)\phi_n^*(x)| \sum_{m=-\infty}^{+\infty} B_m\phi_m(x)\rangle$$

Sorting this equation in terms of the unknown coefficients $\mathtt{B_m}$ it can be written as

$$\sum_{m=-\infty}^{+\infty} (\langle h_n(x)\phi_n^*(x)|\phi_m(x)\rangle - \delta_{m,n})B_m = -\langle h_n(x)\phi_n^*(x)|F^i(x, f(x))\rangle \qquad \text{(A.12)}$$

As it has been stated in section A.1.2 the $\mathtt{B_m}$ coefficients are directly related to the efficiencies of different orders and depend on the ratio $\lambda/\mathtt{g}$. There will be a limited number of orders that carry energy, therefore the summation can be truncated to a finite range -N to N. The lower limit for the number of coefficients can be found by checking the convergence of the coefficients $\mathtt{B_m}$ when N varies. The system of equations given by truncated form of Eq. A.12 can be written as,

$$\sum_{m=-N}^{N} (\langle h_n(x)\phi_n^*(x)|\phi_m(x)\rangle - \delta_{m,n})B_m = -\langle h_n(x)\phi_n^*(x)|F^i(x, f(x))\rangle$$

$$n = 1, 2, ..., 2N + 1$$

These are 2N+1 linear equations of 2N+1 unknown coefficients $\mathtt{B_m}$ that can be solved. Generally when the ratio $\lambda/\mathtt{g}$ decreases, N increases and the $\mathtt{B_m}$ coefficients do not converge quickly.

A.2 Normal conducting metallic gratings

In this part it is assumed that the region $\mathtt{R\_}$ is a dielectric or metal of complex refraction index ν. As a result, for the complete solution of the grating problem the electromagnetic field in the region $\mathtt{R\_}$ has to be taken into consideration.

Similar to the approach of section A.1 it can be seen that the magnitude of the field, $\mathtt{F}^{\pm}$ (for both polarizations), satisfies the differential equation Eq. 4.1 with boundary conditions Eq. 4.2 (see [34]).
Defining the field generated at a point P of the region $\mathtt{R}_{+}$ by a single elementary current placed at $\mathtt{M} \in \rho$ (Green function method), the diffracted field $\mathtt{F}^{\pm}(\mathtt{P})$ can be deduced by integrating on ρ the effects of all currents. Using the notation of [34] the integral equation for $\mathtt{F}^{\pm}(\mathtt{P})$ can be written as

$$F^{\pm}(x,y) = \sum_n D_n^{\pm} \exp(i\alpha_n x \pm i\beta_n y)$$

where $\mathtt{D}_{\mathtt{n}}^{\pm} = \int_0^{\mathtt{g}} \mathtt{T}_{\mathtt{n}}^{\pm}(\mathtt{x})\tau(\mathtt{x})\mathtt{dx}$ and the expressions for $\mathtt{T}_{\mathtt{n}}^{\pm}$ and τ for the two polarizations are given by

$$T_n^{\pm}(x) = \begin{cases} \frac{1}{2ig\beta_n} \exp\left(-i\alpha_n x \mp i\beta_n f(x)\right) & TE\ mode \\ \frac{1}{2g}\left(\pm 1 - \frac{\alpha_n}{\beta_n} f'(x)\right) \exp\left(-i\alpha_n x \mp i\beta_n f(x)\right) & TM\ mode \end{cases}$$

$$\tau(x) = \begin{cases} \left(1 + f'^2(x)\right)^{1/2} \left[\frac{dF^+}{d\mathcal{N}(x)} - \frac{dF^-}{d\mathcal{N}(x)}\right] & TE\ mode \\ F^+(x) - F^-(x) & TM\ mode \end{cases}$$

The coefficients $\mathtt{B}_{\mathtt{n}}$ used in section A.1.2 for the efficiency calculation take a complicated form and will not be given here (see [34]).

Appendix B

THz Filter Calibration Measurements at BESSY

THz filters[1] and their precise transmission curves play an important role in the wavelength calibration of the grating spectrometers. For this reason, several measurements were carried out at BESSY. An interferometer (Bruker IFS66v) with KBr beam splitter and the glowbar source and Bolometer as the detector was provided[2]. Air pressure during measurements was about 3.5 mbar.

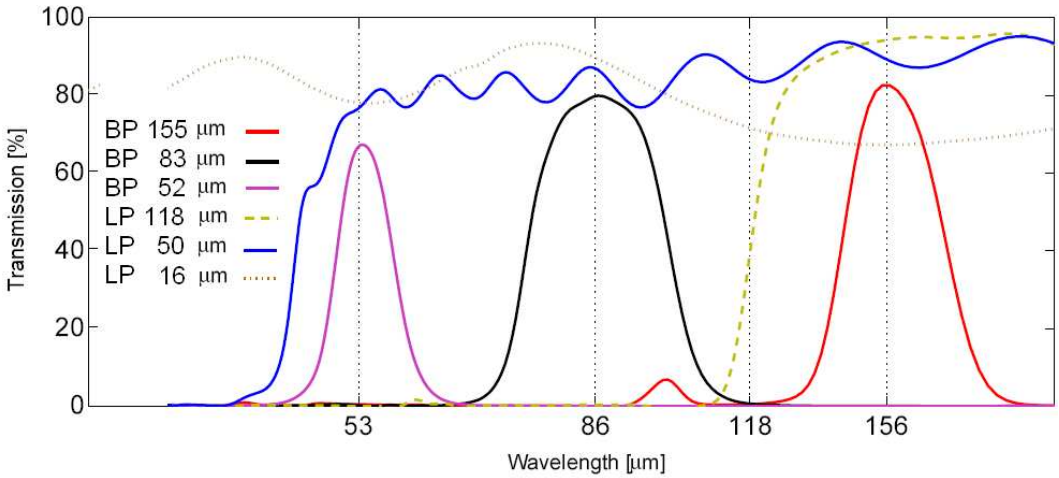

Figure B.1: Transmission curves of several THz filters

[1]The producer of the THz filters, QMC [68], provides the measured transmission curves for a restricted wavelength range.

[2]These measurements as well as the DTGS pyroelectric calibration measurements were supported by U. Schade (BESSY).

Appendix C

Infrared Polarizer

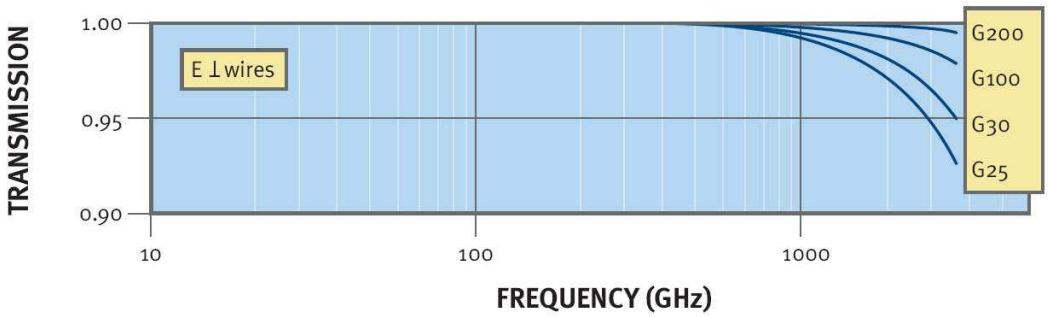

Figure C.1: Transmitted polarization for G30 and G25 MICROTEK THz polarizers (Courtesy of MICROTEK).

In Figures C.1 and C.2 the transmission of polarizers G30 and G25 (MICROTEK) over millimeter and sub-millimeter wavelength range in both polarizations are given. The electric field is perpendicular to the wires of the polarizers for the radiation that gets through the polarizers.

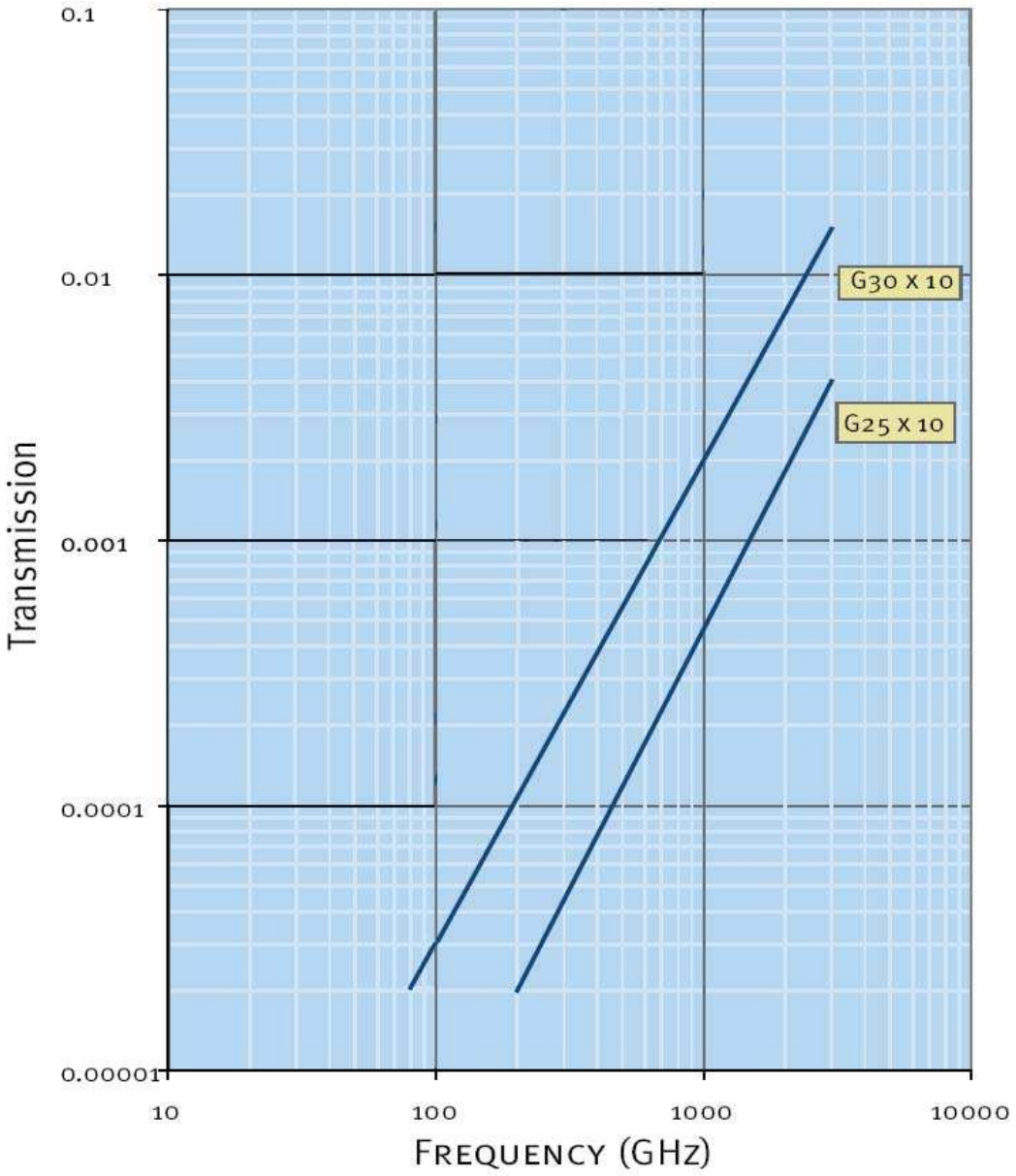

Figure C.2: Blocked polarization for G30 and G25 MICROTEK THz polarizers (Courtesy of MICROTEK)

Appendix D

Transmission of Several Materials in the THz Range

For those materials that are used in different measurements of this thesis the transmission over the wavelength range 3 to 300 μm is given in Fig. D.1 [69].

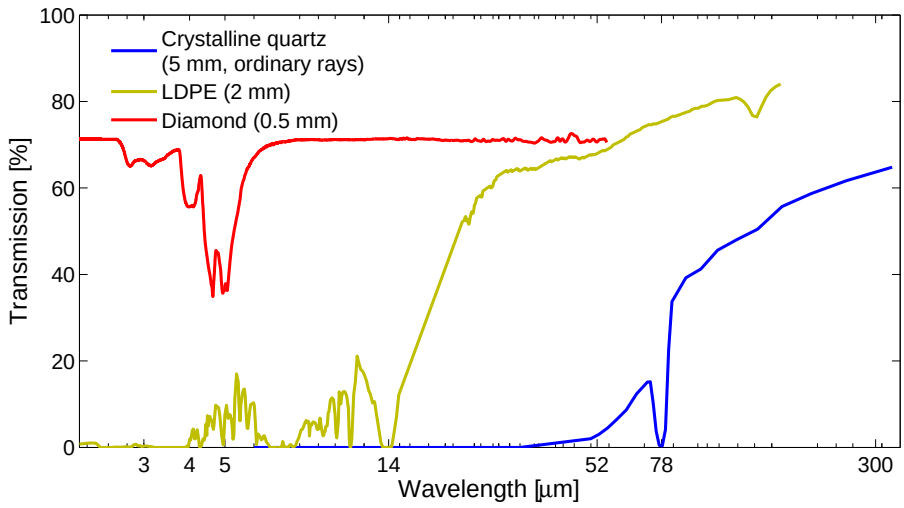

Figure D.1: Transmission of diamond, LDPE and crystalline-quartz window with the thickness that is mentioned in the plot [69].

Water absorption lines are shown for one meter of humid air in Fig. D.2. The absorption of radiation over the infrared range by humid air shows the importance of making the entire setup in vacuum.

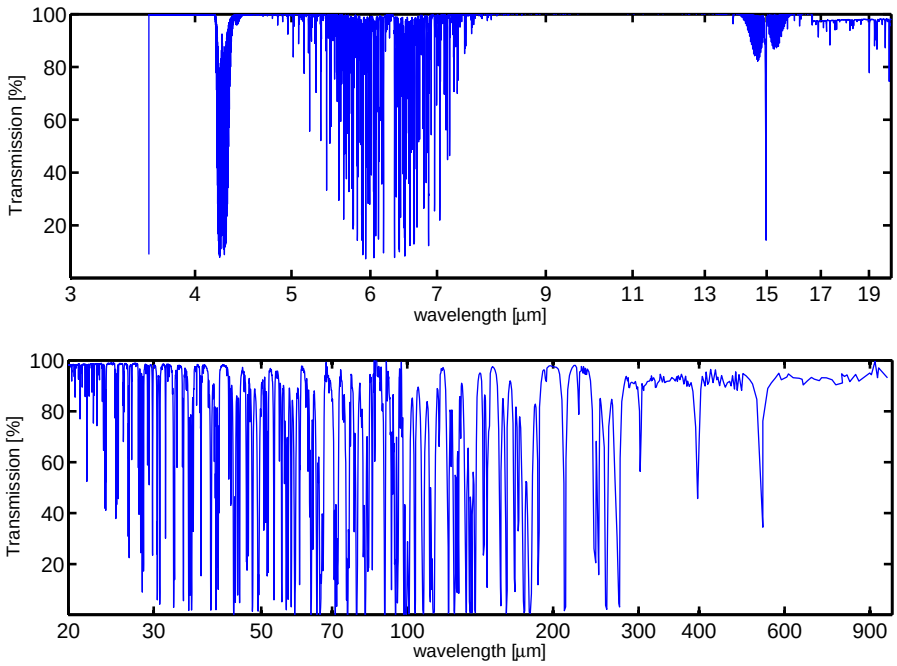

Figure D.2: Transmission of one meter humid air [70]

Appendix E

Geometrical Design of Collecting Cones

In Eq. 6.1 a way to trace rays reflected from a surface is given. The sketch in Fig. E.1 illustrates the situation. Each ray incident upon the surface of the cone may enter to the throat dependent on the vertical distance between the first point that it hits the cone and the throat. The red ray hits at a point above the acceptance and therefore does not enter the throat. The solid blue ray shows the starting point of the acceptance for rays that hit parallel to the cone axis. If a ray, like the dashed blue, enters to the acceptance region with angles smaller than the cone angle, it will get through (dashed blue and green). The limit of the acceptance region can be determined by considering rays that enter to the throat after multiple reflections like the solid green ray.

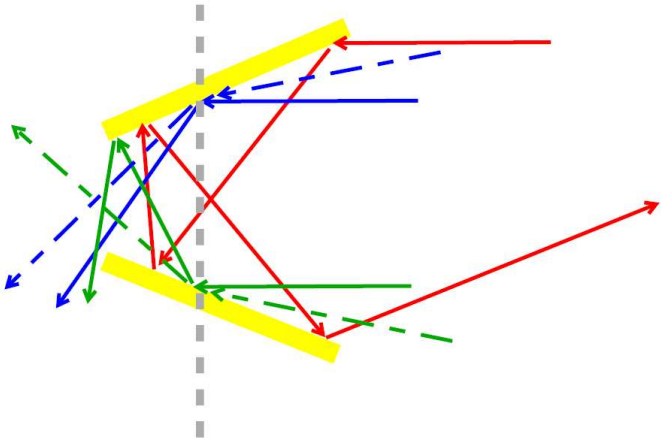

Figure E.1: A pure geometrical computation on the collecting properties of a cone.

With cone angle of about 18°, the ratio of the area where the acceptance begins (indicated by the broken line in Fig. E.1) to the throat area is ≈ 4. This is determined by considering all rays that may enter after multiple reflections. This ratio is the basis of the design for the cones that are used in the collecting optics. This optimizes the inlet radius of the cones. For larger values there is no higher collection efficiency.

Appendix F

Auxiliary Measurements

One important aspect of setting up any experiment that measures the spectral intensities of the coherent transition radiation of the electron bunches at CTR140 is the optimization of the kicker strength. The optimum strength varies depending on the electron energy and the actual electron orbit.

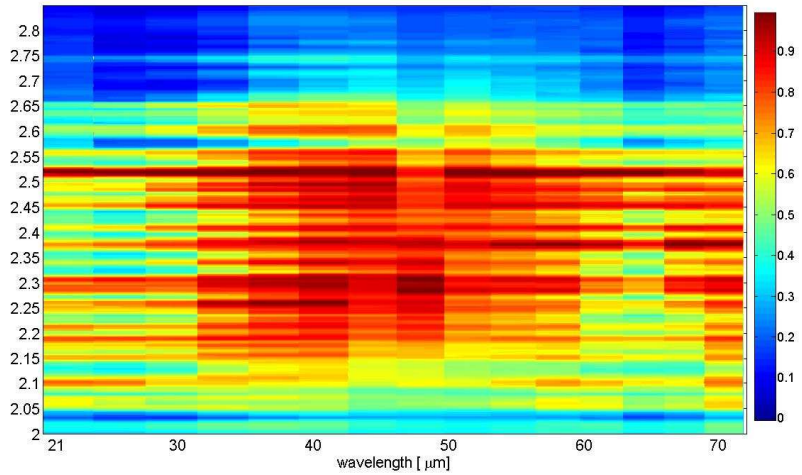

Figure F.1: Kicker strength optimization for the machine study period Feb. 2007. The H.V. setting equal to 2.5 kV has been selected to center the kicked bunch on the off-axis screen.

The strength is optimum when the electron beam hits the central part of the off-axis screen. In Fig. F.1 a systematic study on this issue in a stable run is shown. As it is clear from the density plot, the optimum kicker strength is for a high voltage of ≈ 2.5 kV. This run corresponds to the February 2007 measurements that are presented in section 8.5.
The dependence of the CTR spectra on the target screen position is studied in Fig. F.2. This shows a sample comparison made in short wavelengths (using the RMS device thus it is not single shot) to see the differences when the off-axis screen or a full screen [1] is used. These measured spectra show that these modes of operation are identical.

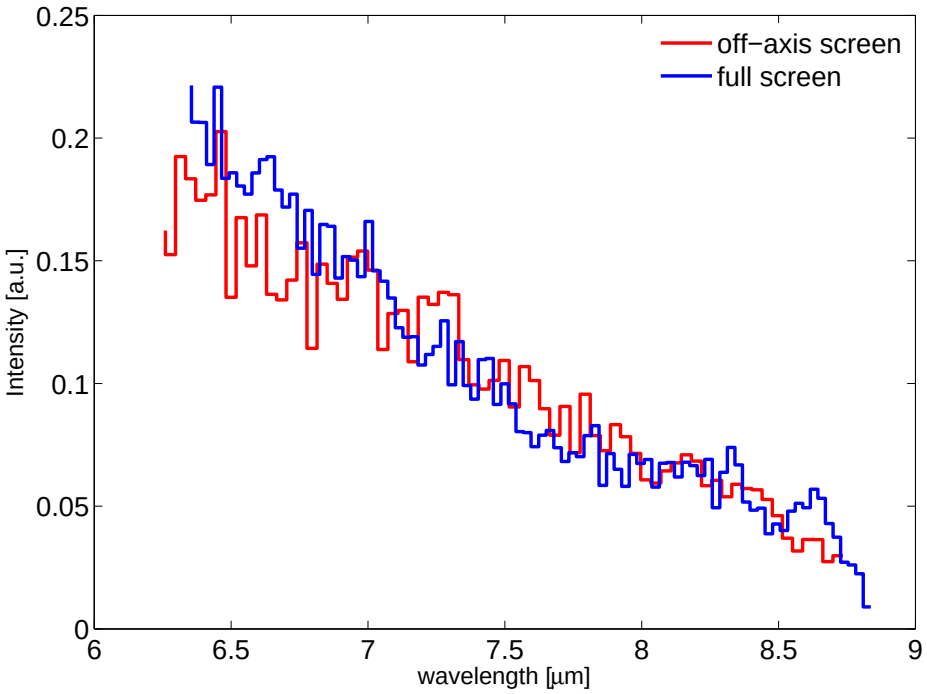

Figure F.2: The sample spectra measured for the comparison of the two types of radiation screens.

The CTR spectrum over the shortest wavelengths, which have ever been measured at FLASH, is shown in Fig. F.3. With the same conditions of the machine and shortly after measuring the short wavelengths spectrum, the wavelength range that corresponds to the spiky part of the spectrum is covered and

[1] A full screen blocks the users mode operation of the machine. Therefore, it is foreseen to kick a bunch out of the train to the off-axis screen.

shown in the same plot.

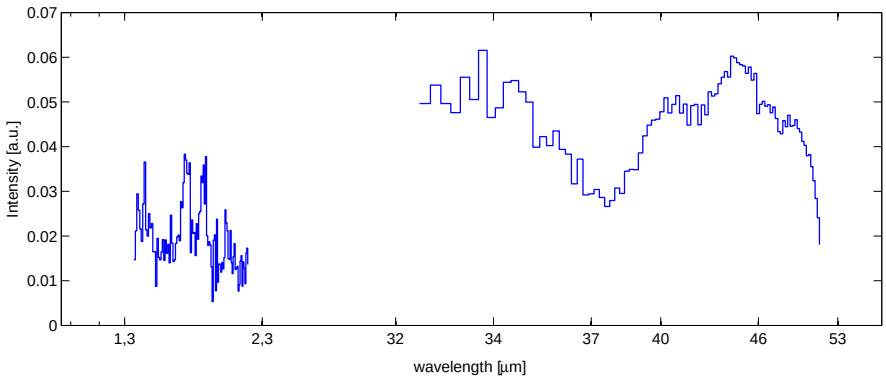

Figure F.3: The comparison of the intensity of the CTR in the shortest measured wavelengths together with the one over the range that is known to correspond to the peak of the CTR wavelength spectrum.

In chapter 3 it was mentioned that the charge density distribution of the bunch is a three dimensional one and there are conditions under which one can use the line charge approximation. The influence of the transverse size on the measured spectrum is discussed in [25]. An experimental study on this issue using the two stage single shot spectrometer has been carried out at FLASH. A setting of the machine is installed to make high intensities over the short wavelengths. The optics of the machine kept as the optics for the SASE mode operation. The measured average spectrum is shown in Fig. F.4 in blue color. In the next step, adjusting the settings of several quadrupoles[2], the transverse size of the electron beam has been blown up by a factor of ≈ 3.5 at the closest OTR-screen (4 m downstream CTR140 screen). The averaged measured spectrum is shown in red. The ratio of these two measured spectra is shown in green and theoretical calculation of the ratio is also shown in dashed-black. For the theoretical calculation Eq. 16 in reference [25] for the wavelength domain form-factor of a 3D-Gaussian profile is used. In the theoretical calculation the influence of the blown-up beam size on the transmission is taken into account. This shows a qualitative agreement which can be considered as the basis for further investigations.

[2]Thanks to Nina Golubeva and Vladimir Balandin for their electron beam optics calculations.

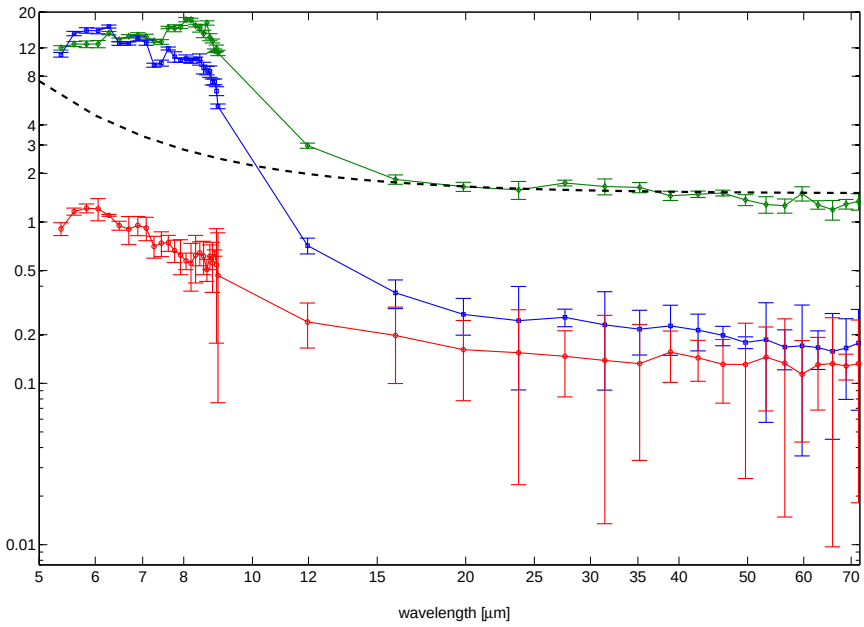

Figure F.4: Transverse beam-size effect on the CTR spectrum. An RF phase of the first accelerating module was set to maximize the short wavelengths with a SASE operation electron-optics. The blue curve shows the recorded CTR spectrum in such conditions. Then the electron-optics was changed in the region nearby an OTR screen (the closest screen down-stream the CTR140 screen) to blow up the transverse beam size by a factor of ≈ 3.5. The red spectrum is measured in this condition of blown up electron-beam transverse size. The ratio of this two curves is shown in green curve. A theoretical calculation of the ratio is carried out as it is described in reference [25] which is shown in black (dashed) curve.

Bibliography

[1] J. D. Jackson, Classical Electrodynamics, Second Edition, John Wiley and Sons, New York, 1975.

[2] J. Roßbach, LINAC based free-electron laser, TESLA-FEL Report 2004-08.

[3] Martin Dohlus, Peter Schmüser, Jörg Roßbach, Introduction to Ultraviolet and X-Ray Free-Electron Lasers, To be published.

[4] A. M. Kondratenko and E. L. Saldin, Generation of coherent radiation by relativistic electron beam in an undulator, Part. Accelerators, 10,207 (1980)

[5] V. Ayvazian et al., Generation of GW Radiation Pulses from a VUV Free-Electron Laser Operating in the Femtosecond Regime, Phys. Rev. Lett. 88(2002)104802.

[6] V. Ayvazian et al., A New Powerful Source For Coherent VUV Radiation: Demonstration of Exponential Growth and Saturation at the TTF Free Electron Laser, Eur. Phys. J. D20(2002)149.

[7] V. Ayvazian et al., First operation of a free-electron laser generating GW power radiation at 32 nm wavelength, Eur. Phys. J. D 37, 297-303 (2006).

[8] W. Ackermann et al., Operation of a free electron laser from the extreme ultraviolet to the water window, Nature Photonics 1, 336 - 342 (2007).

[9] Jochen R. Schneider et al., FLASH, The Free-Electron Laser in Hamburg, Deutsches Electronen-Synchrotron DESY, http://flash.desy.de/sites/site_vuvfel/content/e395/e2188/FLASH-Broschrefrs_web.pdf

[10] Frank Stulle, A Bunch Compressor for Small Emittances and High Peak Currents at the VUV Free-Electron Laser, DESY-THESIS-2004-041.

[11] M. Dohlus, T. Limberg, P. Emma, Bunch Compression for Linac-based FELs, ICFA Beam Dynamics Newsletter No. 38.

[12] O. H. Altenmueller and R. R. Larson and G. A. Loew, Investigations of Traveling-Wave Separators for the Stanford Two-Mile Linear Accelerator, Rev. Sci. Instrum. 35,(438),1964.

[13] Bernhard Schmidt, OVERVIEW ON DIAGNOSTICS FOR X- AND XUV-FEL, Proceedings FEL 2006, THCAU01.

[14] A. Bolzmann, Investigation of the Longitudinal Charge Distribution of Electron Bunches at the VUV-FEL Using the Transverse Deflecting Cavity LOLA, DESY-THESIS-2005-046.

[15] H. Schlarb, Private communication

[16] M. Nagel, Private communication

[17] M. Hüning et al., Observation of Femtosecond Bunch Length Using a Transverse Deflecting Structure , Proceedings FEL 2005.

[18] B. Steffen, Electro-optic methods for longitudinal bunch diagnostics at FLASH , DESY-THESIS-2007-020.

[19] S.P. Jamison et al., Femtosecond bunch length measurements, Proceedings EPAC 2006, TUYPA01.

[20] I. Willke et al., Single-shot electron-beam bunch length measurements, Phys. Rev. Lett. 88, (2002), 124801.

[21] A.L. Cavalieri et al., Clocking Femtosecond X Rays ,Phys. Rev. Lett. 94, (2005), 114801.

[22] G. Berden et al., Electro-optic techniques with improved time resolution for realtime, nondestructive single-shot measurements of femtosecond electron bunch profiles , Phys. Rev. Lett. 93, (2004), 114802.

[23] B. Steffen et al., Single Shot Longitudinal Bunch Profile Measurements at FLASH using Electro-Optic Techniques, Proceedings EPAC 2006, TUPCH026.

[24] E. L. Saldin, E. A. Schneidmiller, and M. V. Yurkov, A novel diagnostics of ultrashort electron bunches based on detection of coherent radiation from bunched electron beam in an undulator, Proceedings FEL 2004 375-378.

[25] O. Grimm and P. Schmüser, Principles of Longitudinal Beam Diagnostics with Coherent Radiation, TESLA Report 2006-03.

[26] H. Delsim-Hashemi et al., Bunch Compression Monitor , Proceedings EPAC 2006.

[27] L. Fröhlich, Bunch Length Measurements Using a Martin-Puplett Interferometer at the VUV-FEL, DESY-THESIS 2005-011.

[28] Sara Casalbuoni, Bernhard Schmidt, Peter Schmüser, Far-Infrared Transition and Diffraction Radiation, Part I: Production, Diffraction Effects and Optical Propagation, TESLA Report 2005-15.

[29] V. L. Ginzburg and I. M. Frank, Radiation of a uniformly moving electron due to its transition from one medium into another, Journ. Phys. USSR, 9, 353, 1945.

[30] A derivation of the Ginzburg-Frank equation can be found in: L. D. Landau, E. M. Lifshitz, Electrodynamics of Continuous Media, Pergamon, New York, 1960.

[31] G. A. Geloni, E. L. Saldin, E. A. Schneidmiller, M. V. Yurkov, A Method for Ultrashort Electron Pulse Shape-Measurement Using Coherent Synchrotron Radiation, http://arxiv.org/abs/physics/0303113v1.

[32] A.F.G. van der Meer, Private communication.

[33] J. Pavageau and J. Bousquet, Opt. Acta 17, 469(1970).

[34] D. Maystre, Opt. Commun. 6, 50(1972).

[35] E. G. Loewen et al., Grating efficiency theory as it applies to blazed and holographic gratings, Appl. Opt. 16, 2711-2721(1977).

[36] A. Wirgin, Scattering from sinusoidal gratings: an evaluation of the Kirchhoff approximation J. Opt. Soc. Am. 73, 1028-1041(1983).

[37] R. Petit (editor), Electromagnetic Theory of Gratings , Springer-Verlag, 1980

[38] GSolver, Grating Solver, available from www.gsolver.com

[39] M. Altareli et al., XFEL Technical Design Report, http://xfel.desy.de/

[40] Sara Casalbuoni, Bernhard Schmidt, Peter Schmüser, Coherent Transition and Diffraction Radiation, Part II: The THz Beam-line at the VUV-FEL , TESLA-FEL Report 2006-04.

[41] James D. Brownridge and Sol Raboy, Pyroelectric response in $LiNbO_3$ and $LiTaO_3$ to temperature changes, arXiv: physics/0107046V1, 19 July 2001.

[42] J. Cooper, Minimum Detectable Power of a Pyroelectric Thermal Receiver , THE REVIEW OF SCIENTIFIC INSTRUMENTS, VOLUME 33, NUMBER 1, JANUARY, 1962.

[43] E. H. Putley, The Pyroelectric Detector, Semiconductors and Semimetals R. K. Willardson and A.C. Beer (eds.) Academic Institute of Physics, New York, NY. Vol. 5, 1970, pp. 259-285.

[44] S. Lavi and M. Simhony, Pyroelectric response to single infrared laser pulses in triglycine sulphate and strontium-barium niobate, J. Appl. Phys., Vol. 44, No. 11, November 1973.

[45] A. Shaulov and M. Simhony, Peak Voltage of the Pyroelectric Response to Short Infrared Laser Pulses, Appi. Phys. Lett. Vol. 20, No. 1, 1 January 1972.

[46] Wen-Sen Zu et al., Pyroelectric detection of submicrosecond laser pulses between 230 and 530 μm, Appl. Opt. 28,3647-3651(1989).

[47] B. Schmidt, Private communication.

[48] B. Schmidt et al., Comments on Pyroelectric Response - Influence of Material Parameters and Geometry, http://tesla.desy.de/fla/crd/IR_related_info.html

[49] B. Schmidt et al., The reflection, transmission, and absorbtion coefficients for a multi-layer arrangement of dielectric materials for vertical incidence of electromagnetic waves, http://tesla.desy.de/fla/crd/IR_related_info.html.

[50] O. Grimm et al., Detector Response and Beam Line Transmission Measurements with Far-Infrared Radiation, Proceedings FEL 2005.

[51] M. J. E. Golay, A Pneumatic Infra-Red Detector, Review of Scientific Instruments, Vol. 18, No. 5 (p. 357), May 1947.

[52] M. J. E. Golay, Theoretical Considerations in Heat and Infra-Red Detection, with Particular Reference to the Pneumatic Detector, Review of Scientific Instruments, Vol. 18, No. 5 (p. 347), May 1947.

[53] M. J. E. Golay, The theoretical and Practical Sensitivity of the Pneumatic Infra-Red Detector, Review of Scientific Instruments, Vol. 20, p. 816, 1949.

[54] E. Chiadroni, Bunch Length Characterization at the TTF VUV-FEL, TESLA-FEL 2006-09.

[55] M. Gensch et al., New infrared undulator beamline at FLASH, Infrared Phys. Techn. (2008).

[56] http://tesla.desy.de/doocs/

[57] H. Delsim-Hashemi et al., Single-Shot Longitudinal Diagnostics with THz Radiation at the Free-Electron Laser FLASH , Proceedings FEL 2006.

[58] http://www.rijnhuizen.nl/research/guthz/felix

[59] http://cremat.com

[60] B. Schmidt, THz Transport: Uebergangs und Diffraktionsstrahlung Erzeugung und Transport durch optische Elemente, www.desy.de/schmidtb/THzTransport.

[61] Oscar P. Bruno and Fernando Reitlich Numerical solution of diffraction problems: a method of variation of boundaries J. Opt. Soc. Am. A 10, 2307-2316 (1993).

[62] A. Bytchkov et al., Development of MCP-based photon diagnostics at the TESLA Test Facility at DESY, Nucl. Instr. and Meth. A 528(2004), p. 254.

[63] Vitali Kocharyan, Private communication.

[64] Ch. Gerth et al., Measurement of gigawatt radiation pulses from a vacuum and extreme ultraviolet free-electron laser, Applied Physics Letters, Vol. 83, No. 14.

[65] Jeffery C. Lagarias, James A. Reeds, Margaret H. Wright, and Paul E. Wright, Convergence Properties of the Nelder-Mead Simplex Method in Low Dimensions, SIAM Journal of Optimization, Vol. 9 Number 1, pp. 112-147, 1998.

[66] MATLAB Version 7.0.0.19920(R14).

[67] Madden, R.P. and J. Strong, Concepts of Classical Optics, Freeman & Co, San Francisco, 1958.

[68] http://www.terahertz.co.uk/

[69] Downloaded from: "http://tesla.desy.de/fla/crd/IR_related_info.html" on August 2007.

[70] Britta Redlich, Private communication.

Acknowledgements

I would like to express my gratitude to all those who helped me to complete this thesis. I am deeply indebted to my supervisor Prof. Dr. Jörg Roßbach whose help, stimulating suggestions and unflinching encouragement helped me in all aspects of my work.
My words cannot express my thanks to PD. Dr. Bernhard Schmidt, who helped me in many parts of my research. His knowledge and experience within the fields of infrared detectors and generation and transport of THz transition radiation provided an excellent backbone for me.
Thanks to Dr. Oliver Grimm for his excellent support in different areas, especially during all shifts of measurements at FLASH and other labs.
Thanks to Dr. A.F.G. van der Meer, who exceptionally inspired and enriched many useful ideas and together with Dr. Britta Redlich provided the possibility for the very crucial measurements that have been carried out at FELIX.
Thanks to all members of the FLASH team for their patience and help during my measurements. Especially I acknowledge the support by Dr. Siegfried Schreiber, Dr. Bart Faatz and Dr. Katja Honkavaara. Thanks to all members of the FLA group at DESY for their help and for providing interesting discussions about different topics. Especially I acknowledge excellent talents of Bernd Beyer in mechanical design and construction, Matthias Hoffmann in electronics and Dr. Bernd Steffen in lab techniques.
Thanks to Lars Fröhlich and Dr. Bolko Beutner for their useful discussions on different aspects, specially their help in math-softs and LaTeX. I am very much indebted to Dr. Christopher Gerth for his valuable advice in science discussions and furthermore using his precious time to correct this thesis in terms of English.
Especially I would like to give my special thank to my wife, Nasrin, whose patient love enabled me to complete this work.